A Dissertation

entitled

Experimental Characterization of an Innovative

Thermo-Brachytherapy Seed for Prostate Cancer Treatment

by

Somayeh Taghizadehghahremanloo

Submitted to the Graduate Faculty as partial fulfillment of the requirements for the

Doctor of Philosophy Degree in Physics

Dr. David Pearson, Committee Chair

Dr. Ambalanath Shan, Committee Member

Dr. Aniruddha Ray, Committee Member

Dr. Mersiha Hadziahmetovic, Committee Member

Dr. Nikolas Jacob Podraza, Committee Member

Dr. Daniel Hammel, Acting Vice Provost for Graduate Affairs
Office of Graduate Affairs

The University of Toledo
May 2024

An Abstract of

Experimental Characterization of an Innovative Thermo-Brachytherapy Seed for Prostate Cancer Treatment

by

Somayeh Taghizadehghahremanloo

Submitted to the Graduate Faculty as partial fulfillment of the requirements for the Doctor of Philosophy Degree in Physics

The University of Toledo
May 2024

Adjuvant administration of hyperthermia with radiation therapy in the treatment of cancer has been extensively studied in the past five decades. Concurrent use of the two modalities was found to lead to both complementary and synergetic enhancements in tumor management but presents a practical challenge. Their simultaneous administration using the same implantable seed source has recently been established theoretically through magnetically mediated heat induction and the utilization of ferromagnetic materials. Careful consideration, however, showed that regular ferromagnetic alloys lack the power to overcome blood perfusion at clinically measured rates.

We characterized the newly developed thermo-brachytherapy (TB) seed that combines a sealed radioactive source with a ferrimagnetic ceramic (ferrite) core, serving as a self-regulating hyperthermia source when placed in an alternating electromagnetic field. A TB seed structure is based on the Low Dose Rate (LDR) brachytherapy seed, with the ability to simultaneously deliver heat to the target. To increase the heat production and uniformity of temperature distribution, we used hyperthermia-only (HT-only) seeds in the empty spaces within already-inserted implantation needles.

The heat generation is due to eddy currents circulating in the seeds' thin metal shell; it depends drastically on the permeability of the core. We identified a soft ferrite material ($MnZnFe_2O_4$) as the best candidate for the core, owing to its high

permeability, the hyperthermia range Curie temperature, adjustable through specific material composition, and a sharp Curie transition. By measuring the magnetic properties of ferrite samples with different compositions, the final core prototype with the optimal parameters was identified. For this purpose, the permeability as a function of temperature was calculated based on measured circuit parameters and material B-H curves. The thickness of the shell enclosing the ferrite core was optimized separately for TB and HT-only seeds, having slightly different dimensions. Heat generation was calculated using the power versus temperature approximation. Finally, the temperature distribution for a realistic prostate LDR brachytherapy plan was modeled with COMSOL Multiphysics for a set of blood perfusion rates found in the literature.

The small size of investigated ferrite core samples resulted in demagnetization significantly decreasing the relative permeability from its intrinsic value of ~ 5000 to about 11 in the range of magnetic field amplitude and frequency values used in the clinical setting. The power generated by the seed dropped sharply as the shell thickness deviated from the optimal value. The optimized TB and HT-only seeds generated approximately 45 mW and 260 mW power, respectively, providing hyperthermia sources sufficient for $> 90\%$ volume coverage even for the highest blood perfusion rates. Due to the rapid Curie transition leading to heat self-regulation, no invasive thermometry is required. The toxicity of the normal tissue surrounding the prostate is minimal due to the rapid temperature fall off within a few millimeters distance from a seed.

The TB and HT-only seed prototypes presented here were shown to provide sufficient power for concurrent administration of radiation and hyperthermia. In addition to being used as a source for both radiation and heat at the onset of cancer therapy, these implanted seeds would be available for thermal re-treatment of the tumor in case of recurrence, possibly as a sensitizer to systemic therapies or as a modulator of the immune response, without another invasive procedure. Experimentally determined parameters of the ferrite material cores provided in this study open an opportunity for moving the project to preclinical animal evaluations.

Acknowledgments

I express my sincere gratitude to my adviser, Dr. David Pearson, for his invaluable insights throughout the course of my Ph.D. journey. With special appreciation extended to Dr. Ambalanath Shan for his support, insightful comments, and expertise, which made my research possible. I am also grateful to Dr. Aniruddha Ray, Dr. Nikolas Podraza, and Dr. Mersiha Hadziahmetovic for their valuable advice and guidance that significantly contributed to my academic growth. Additionally, this work would not have been possible without the help and support of Dr. Diana Shvydka, Dr. Gregory Warrell, Dr. Nicholas Sperling, Dr. Richard Irving, and Dr. Ishmael Parsai.

I owe so much to my fellow graduate students and medical physics residents, especially James Seekamp whose invaluable assistance significantly enriched my understanding of clinical medical physics.

I would like to thank my family, especially my parents, and my brothers for their continuous encouragement of my dedication to and passion for science.

Finally, I want to express my deepest thanks to my beloved husband, Emad. The past few years, though marked by lots of challenges and sacrifices, have been sustained by his unwavering love and support. Without him, none of this would have been achievable.

Contents

List of Tables

List of Figures

List of Abbreviations

CAPRA .... Cancer of the prostate risk assessment
CEM .... Cumulative equivalent minutes
CT .... Computed tomography

DC .... Dendritic cell
DNA .... Deoxyribonucleic acid
DSB .... Double-strand break

EBRT .... External beam radiation therapy

HDR .... high dose rate
HIFU .... High-intensity focused ultrasound
HSP .... Heat shock protein
HT .... Hyperthermia

IRT .... Internal radiation therapy
ISA .... Interseed scatter and attenuation

LDR .... Low dose rate

MDR .... Medium dose rate
MRI .... Magnetic resonance imaging

NK .... Natural killer
NP .... Nanoparticle

PET .... Positron emission tomography
PI .... Parasitic inductance
PSA .... Prostate specific antigen
PSMA .... Prostate-specific membrane antigen
PTV .... Planning target volume

RBC .... Red blood cells

RL .... Resistor-inductor
RNA .... Ribonucleic acid
RT .... Radiation therapy

SAR .... Specific absorption rate
SSB .... Single-strand break

TER .... Thermal enhancement ratio
TB .... Thermo-brachytherapy

WBH .... Whole-body hyperthermia

List of Symbols

Φ .... Magnetic field flux

α .... Single-strand break coefficient
α_L .... Linear thermal expansion coefficient
α_V .... Volume thermal expansion coefficient
β .... Double-strand break coefficient
γ .... Aspect ratio
δ .... Skin depth
ϵ_c .... Core electric permittivity
θ .... Angle
κ_L .... Non-uniformity correction coefficient
κ_m .... Mutual inductance correction coefficient
κ_s .... Self inductance correction coefficient
μ .... Permeability
μ_0 .... Vacuum permeability
μ' .... Real component of relative permeability
μ'' .... Imaginary component of relative permeability
ρ .... Mass density
ρ_b .... Blood mass density
σ .... Conductivity
σ_{SB} .... Stefan-Boltzmann constant
σ_s .... Shell conductivity
ϕ_A .... Phase angle at node A
ϕ_B .... Phase angle at node B
ω .... Angular frequency
ω_h .... Energy density

$\delta\phi$ .... Phase shift
Δl .... Change in length
ΔT .... Change in temperature
ΔV .... Change in volume
ε .... Emissivity

A_c .... Area of the coil
$\vec{A}$ .... Magnetic vector potential
B .... Magnetic flux density
C_p .... Specific heat capacity at constant pressure
C_b .... Blood heat capacity
D .... Exposure dose
E .... Electric field
F .... Force
H .... Magnetic field
H_0 .... External magnetic field
H_d .... Demagnetization field
I .... Current
J .... Current density
L .... Total inductance
$L_{c_{\text{air}}}$ .... Inductance of a core-less coil
L_i .... Internal inductance
L_{par} .... Parasitic inductance
M .... Magnetization
N .... Number of turns
N_d .... Demagnetization coefficient
P .... Power
Q .... Heat
R .... Resistance
R_o .... Oscilloscope resistance
R_L .... Inductor resistance
S .... Survival rate
T .... Temperature
V .... Volume
V_A .... Electric potential at node A
V_B .... Electric potential at node B
V_{par} .... Parasitic voltage
V_R .... Voltage across resistor
V_c .... Voltage across the coil
V_{r_w} .... Voltage due to wire resistance
Y .... Young's modulus
$\mathbf{Z}_{\text{tot}}$ .... Total impedance
$\mathbf{Z}_L$ .... Inductor impedance

a .... Semi-major axis
b .... Semi-minor axis
c_o .... Ocsilloscope capacitance

d_w .... Wire diameter
d_c .... Coil diameter
f .... Frequency
j .... $\sqrt{-1}$
k .... Thermal conductivity
ℓ_c .... Coil length
ℓ_f .... ferrite core length
p .... Pitch
r_c .... Coil radius
r_s .... Shell radius
r_w .... Wire resistance
t .... Time
t_s .... Shell thickness

Chapter 1

Introduction

1.1 Prostate Cancer

A tumor is an abnormal mass in the body that grows because of cells reproducing too quickly or failing to die when they should. Tumors are classified as benign or malignant based on a variety of characteristics. Benign tumors grow slowly and have distinct edges, not invading surrounding tissue or other parts of the body. On the other hand, malignant tumors have irregular borders, invade surrounding tissues, and can migrate to distant locations in the body to create new tumors (a process called metastasis). Difficulties in treating cancer are due to its particular abilities for immune escape, metastasis, and resistance to cancer therapies.

Cancers are named for the region where they first appear and the type of cell they are comprised of, even if they move to other regions of the body. In general, there are four clinical terms used for certain types of cancer. Carcinoma is a type of cancer that develops in the skin or tissues surrounding other organs. Sarcoma is a type of cancer that affects connective tissues such as bones, muscles, cartilage, and blood vessels. Leukemia is a cancer of bone marrow, which creates blood cells. Lymphoma and myeloma are cancers of the immune system.

Among the different types of cancer, prostate cancer is becoming an increasingly important public health problem in the United States. According to the American Cancer Society's 2022 Facts and Figures, prostate cancer is the first in incidence and second in the cancer-related cause of death in men, with 268,490 new diagnoses and 34,500 deaths from this disease projected for 2022 [1]. One in eight men will be diagnosed with prostate cancer at some point in their life, and one in forty-one dies from this disease. Therefore, knowledge about prostate cancer is essential. The average age of diagnosis is 66 years. The majority of prostate cancer occurrences (89%) are diagnosed while the disease is limited in the prostate and adjacent organs, a stage known as local or regional stage. Most patients with local or regional prostate cancer have a 5-year survival rate of about 100%. For people diagnosed with prostate cancer that has spread to other parts of the body, the 5-year survival rate is 30%.

1.2 Risk Assessment

To categorize the risk of prostate cancer, clinicians use risk assessment systems. Risk assessment systems provide a simple tool for disease risk categorization in clinical decision-making and future research. Risk assessment may be carried out in various ways, including the D'Amico classification, a variety of nomograms, and the UCSF-cancer of the prostate risk assessment (CAPRA) score. The category developed by D'Amico is one of the most widely used and is a good starting point for risk assessment. This system uses prostate specific antigen (PSA) level (blood test), Gleason grade (microscopic appearance of the cancer cells), and T stage (size of the tumor on the rectal exam and/or ultrasound) to group men as low, intermediate, or high-risk. PSA less than or equal to 10, Gleason score less than or equal to 6, and clinical stage T1-2a are classified as low-risk. Intermediate risk is PSA between 10 and 20, Gleason scores 7, or clinical stage T2b. PSA more than 20, Gleason score equal or larger than 8, or clinical stage T2c-3a is considered high-risk.

Medical nomograms use biological and clinical variables, such as tumor grade and patient age, to graphically depict a statistical prognostic model that generates a probability of a clinical event, such as cancer recurrence or death. UCSF-CARPA score is a pre-treatment score based on patient age, PSA, biopsy Gleason score, clinical T stage, and percentage of positive biopsy cores. The CAPRA score predicts cancer recurrence risk with an accuracy comparable to other pre-treatment risk prediction instruments. Yet it is simple to calculate, requiring no paper tables or computer software [2]. Prostate cancer risk assessment is thus critical in identifying a group of men at high risk of cancer mortality who require aggressive, sometimes multimodal, therapy and those at low risk and may be spared the potential impact of treatment on quality of life.

1.3 Prostate Cancer Treatment Modalities

Based on the staging of prostate cancer, we have different therapeutic methods. When selecting a treatment for an individual patient, the physician should consider the extent of disease, patient age, and competing co-morbidities. Surgery is an option to remove the tumor and some surrounding lymph if the patient is in good health. Different types of surgery are radical (open) prostatectomy, robotic or laparoscopic prostatectomy, and bilateral orchiectomy.

Radiation therapy (RT) is another option when prostate cancer is in its early stages or is limited to the prostate. One can also use RT to eliminate any cancer cells left behind after surgery. There are two types of RT, external beam radiation therapy (EBRT) and internal radiation therapy (IRT). EBRT is the most common radiation treatment technique generating radiation outside the patient, usually by a linear accelerator. EBRT is a method for delivering a beam or several beams of high-energy x-rays to a patient's tumor. In the IRT method, radioactive material sealed in needles, seeds, wires, or catheters is placed directly into or near a tumor, and it is also denoted as brachytherapy.

For advanced cancer, hormonal therapy is one of the standard options. Hormone therapy is a cancer treatment that involves removing hormones or inhibiting their activity and preventing cancer cells from proliferating. Chemo will be a substitute option if cancer is spread outside the prostate gland and hormone therapy is not working. Chemotherapy is a cancer treatment that employs drugs to prevent the development of cancer cells, either by killing the cells or by prohibiting them from dividing.

Immunotherapy uses the body's immune system to attack cancer cells. It is a promising treatment for prostate cancer, including advanced or recurrent forms of the disease [3]. Bisphosphonate therapy can ease pain and prevent fractures if the disease reaches the patient's bones. There are more option to treat men with low-risk early-stage prostate cancer who cannot have surgery or radiation therapy is cryotherapy. Cryotherapy (also known as cryosurgery) involves freezing and killing prostate cancer cells at extremely low temperatures.

1.4 Brachytherapy

Brachytherapy is an established treatment for prostate cancer. In this thesis our work is more focused on the brachytherapy technique and some alterations to this method for enhancement, therefore this technique will be discussed in more details in the following.

Brachytherapy is a short-distance treatment of cancer with a radioactive isotope placed on, in, or near the lesions or tumor to be treated [4]. Based on the doses rate delivery, brachytherapy techniques are classified as either high-dose-rate (HDR), medium-dose-rate (MDR), and low-dose-rate. HDR devices use dose rates of over

12 Gy/h at 1 cm from the source. MDR brachytherapy is a treatment that delivers doses at a rate 2-12 Gy/h. Lower values, in the range of 0.4-2 Gy/h, are used by LDR devices. The most common radioisotopes used in brachytherapy are iridium-192, Iodine-125, cesium-137, palladium-103, and cobalt-60. Sources for brachytherapy are available in several forms (seeds, pellets, tubes, wires, or needles), with different average photon energy and half-life. There are two main types of brachytherapy implants: intracavitary, in which the sources are placed in body cavities close to the tumor, and interstitial, in which the sources are implanted within the tumor. However, other less popular techniques are also available, like surface, intraluminal, intraoperative, and intravascular implants.

The main advantages of brachytherapy include improved toxicity profiles with greater doses applied to the prostate gland. In terms of prostate cancer, HDR brachytherapy involves inserting a temporary radioactive source into the prostate using transperineal catheters. A radiation source, often iridium, is supplied from a chamber via a series of catheters that are temporarily placed inside the prostate using ultrasound guidance.

In LDR brachytherapy, the small radioactive seeds I-125, Cs-137 or Pd-103 are permanently implanted into the prostate gland using a transperineal method. Long needles are inserted, and radioactive seeds are delivered into the prostate gland through the needles, followed by a computed tomography scan to determine their position. They remain in place but gradually become inactive as the radioactivity decays over time. From a radiobiological standpoint, the degree of dose escalation provided by LDR brachytherapy may be more effective in killing tumor cells than other radiation techniques [5]. The physical prescription doses commonly used with LDR brachytherapy are approximately 1.5-2 times higher than those with EBRT, and their biologically effective dose can be up to 3 times greater, and surrounding nearby normal tissues will be contaminated with less toxicity [6].

Compared to most anti-tumor treatments, irradiation is a non-invasive and spatially targeted method since it can penetrate the body and is precisely confined to the depth of interest. On the other hand, some tumor cells can be radioresistant, exhibiting resistance to radiation-induced oxidative stress and DNA damage-induced cell death. In addition, intrinsic DNA repair could prevent the conversion of sublethal and potentially lethal to lethal damages, thereby reducing tumor cell kill. Further presence of hypoxic tumor cells confers radioresistance to tumor cells. At the same time, tumor cells in the "S" phase cycle are intrinsically radioresistant. Although a higher radiation dose is more likely to cause tumor cell death, at the same time, it can harm nearby normal tissue and result in other adverse effects. As a result, many radiosensitization techniques have been established to enhance treatment effectiveness and outcome due to the failure of radiotherapy on advanced disease [7, 8].

1.5 Hyperthermia

The term hyperthermia originates from the Greek word hyper ("raise") and therme (heat). The first record of hyperthermia for cancer treatment was noted in ancient Rome by Cornelius Celsus Aulus, a Roman encyclopedic doctor (25 BC - 50 AD), who recognized that the first stages of cancer are highly thermosensitive. Hippocrates was convinced that tumors incurable by HT were indeed lethal. The first paper on HT was published in 1886 [9]. It was mentioned that the sarcoma on the face of a 43-year-old woman was cured when the fever was caused by erysipelas. A decade later, Westermark [10] used circulating high-temperature water to treat an inoperable cancer of the uterine cervix with positive results with the outcome of the long-term remission. Several other clinical trials with HT were developed in the 1980s.

HT was neglected for a long time due to difficulties in reproducing uniform heat distribution and appropriate temperature, specifically for deep-seated tumors.

Moreover, lack of technology to monitor the temperature of tumor and surrounding tissue and absence of widely applicable quality assurance hampered more clinical use of HT [11, 12].

Some recent studies have shown the effectiveness of hyperthermia in enhancing tumor treatment [13–15]. The biological response of the tumor to heat depends on the intrinsic characteristics of the tumor cell itself and the surrounding environment [16], the temperature and duration of exposure [17, 18]. Specifically, it is known that the tumor cells are hypoxic and contain much less vascular distribution, in which heat can accumulate ("heat-trap") much easier compared to healthy tissues ("heat-sink") at temperatures around 40-44 °C [19, 20]. In modern definition, HT is defined as increasing the tumor temperature in the range 39-45 °C, and thermoablation is the temperatures above that. Heating cells to 39-42 °C reduces their survival rate, while heating to more than 42.5 °C for more than an hour dramatically amplify this effect. The pH microenvironment in tumors is heterogeneous [21]. For poor nutrition and low pH regions of the tumor cell environment are also beneficial to HT while detrimental to radiation therapy due to low oxygenation. To study the benefits of HT in more detail here we outline the major topics on the cellular and molecular targets of HT.

1.5.1 Response of Tumor Blood Flow to Hyperthermia

As tumor size increases, tumor angiogenesis lags behind due to the rapid growth of the cell population. This process is chaotic, resulting in a highly heterogeneous vascular distribution in the tumor [20, 22, 23]. The areas with a lack of vascular distribution and low blood flow are usually nutrient-deprived, low in oxygen, and highly acidic. However, in some cases, especially for small tumors, their blood flow can be higher than normal tissue [14].

Blood flow can be increased by dilation of blood vessels, reperfusion of non-flowing blood vessels, or formation of new vasculature [24]. In a normal tissue blood flow can increase by a factor of 10-15 times compared to a factor of 2 for tumors [25, 26]. The amount of blood flow in the tumor changes the microenvironment of the tumor cells, which along with vascular distribution plays an important role when treated with HT.

The rise in the temperature in the tissue depends highly on the inflow of heat from the external source and outflow of heat by blood circulation. The effect of HT on blood flow can be advantageous in two separate treatment paths.

Several studies have shown raising the tumor temperature in the range 39-42 °C, also referred to as mild HT, increases the blood flow to its maximum value and consequently increases the oxygenation [27–29]. The enhanced oxygenation lasts for about 24 to 48 hours after HT [30]. The areas of the tumor suffering from hypoxia, low pH, lack of nutrients, and previously resistant to radiation are now more vulnerable to radiation. Therefore, using mild HT is a great choice to be applied simultaneously or in sequence with RT to enhance the outcome.

Increasing the tumor temperature to more than 42 °C in the process of HT will result in tumor vasculature damage due to high permeability [29, 31]. Consequently, fluid and protein accumulate in the tumor microenvironment and contribute to elevated interstitial fluid pressure, further reducing vascular perfusion. Moreover, temperatures higher than 43 °C can increase tumors' acidity, which may result in the rigidity of red blood cells (RBC) and reduces its velocity [32]. Elevated temperatures above 37 °C result in a notable increase in lysosomal enzyme activity, with a particularly significant rise observed within the range of 42–44 °C. This effect is pronounced in low pH environments [33]. HT can also be used as a single modality to perform cell kill in these conditions. Vascular disrupting agents, which disrupt the established tumor vasculature and reduce blood flow, are sometimes used to enhance the effect of HT [34].

Being able to image the vascular microenvironments can be very beneficial in predicting the outcome of HT. Some non-invasive methods for this purpose are magnetic resonance imaging (MRI) and positron emission tomography (PET), which are well-established clinical procedures and are used routinely in hospitals [35].

1.5.2 Sensitization of Hypoxic Tumor Cells by HT

Hypoxia is the state in which the cells do not receive sufficient amounts of oxygen. As discussed in the Section 1.5.1, the vascular distribution is heterogeneous due to the rapid and chaotic multiplication of tumor cells, resulting in areas outside the oxygen diffusion regions (100–200 μm from the capillaries) suffering from hypoxia. Hypoxia has two different types. Diffusion-limited or chronic hypoxia arises due to restricted oxygen diffusion within actively metabolizing tissue, and the underlying biological conditions will persist until cell death. Perfusion-limited or acute hypoxia occurs when tumor blood vessels temporarily close, leading to intermittent periods of oxygen deprivation as the blood vessels reopen to restore normoxia. Studies have shown that acute hypoxic cells are more sensitive to HT than chronic hypoxic cells [36].

HT mitigates hypoxic tumor cell environment by increasing blood flow. In the presence of oxygen, the damages derived by free radicals become permanent, which implies the hypoxic cells will be more resistant to RT (about 2 to 3 times) [37]. Given the negative impact of hypoxia on RT, identifying patients with hypoxic tumors and developing approaches to sensitize hypoxic tumor areas to RT is of significant interest.

1.5.3 Hyperthermia-Induced Cell Death

Cell death can be categorized into two extreme cases of necrosis and apoptosis. Apoptosis is an ordered and programmed cell death that is non-immunogenic or anti-inflammatory. Apoptosis is present in all cells, but it is lacking in tumors and plays an essential role in maintaining tissue homeostasis by removing harmful cells [38,39].

HT induces cell death through apoptosis by increased tumor membranes permeability, elevating production of oxygen free radicals, inhibition of DNA repair, and alteration of the cellular cytoskeleton. Apoptosis mainly occurs in mild HT by increasing the blood flow and oxygenation [18].

On the other hand, necrosis is the death of cells in an organ due to disease, injury, or failure of the blood supply. Temperatures higher than 43 °C will cause cell necrosis by damaging the blood vessels and hampering the blood flow [40, 41].

HT has been demonstrated to induce protein denaturation, which affects and alters the internal organization of cells, including cytoskeleton and cell membrane, which are important targets for the induction of heat-induced cell death. The cytoskeleton maintains the cell structure and participates in various activities, including cell movement and cell division. HT alters and disrupts the cytoskeleton, affects the fluidity and stability of cellular membranes, and impedes the function of transport proteins [18].

1.5.4 Heat Shock Proteins

Heat shock proteins (HSPs) are a group of chaperon proteins that protect the cells and regulate cellular homeostasis. They prevent the aggregation of toxic substances by refolding or binding the misfolded protein in a soluble form until it can be refolded or degraded [42]. HSPs are the main natural opposing force against HT. Despite causing apoptotic cell death, HT also results in rapid production of HSPs that induce transient thermotolerance. Hypoxia and infection can cause cell stress and release HSPs. HSPs are divided based on their molecular mass and different biological functions into small HSPs (molecular mass less than 40 kDa) and the HSP60, HSP70, HSP90, HSP100 protein families [43]. The temperatures above 43 °C inhibit HSP synthesis and result in exponential cell death.

Despite their undesirable side effect against mild HT, HSPs have some beneficial aspects for cancer treatment. Studies have shown that the HSPs also induce immunity against tumor cells [44–49]. Among HSPs, HSP70 plays a crucial role because it can be released from the cell to the extracellular environment and connect to the immune surface receptors. This process can stimulate the immune system in different ways [50].

1.5.5 Hyperthermia-Induced Changes in Cellular Immune Response

HT influences the immune response to cancer in various steps through different mechanisms. Heat can either directly activate the immune cells or by releasing heat shock proteins, modulating the expression of surface markers, increasing the release of exosomes containing tumor antigens, or by enhancing tumor perfusion, which allows immune cells to migrate to the tumor [51].

An immune response can be divided into two main phases. An initial non-specific phase (innate immunity) mediated by monocytes, immature dendritic cells (DCs), natural killer (NK) cells, and a later specific phase (adaptive immunity) mediated by cellular (T lymphocytes) and humoral (B lymphocytes) immune reactions.

1.5.5.1 Innate Immune System

HT can increase innate immune response by increasing the proliferation, maturation, and antigen presentation of the DCs. Furthermore, there is evidence that HT can also activate the NK cells by enhanced cytotoxicity and recruitment to the site [52]. NKs are the most effective cells involved in tumor cell growth and recurrence inhibition. In addition, it facilitates immune cell trafficking by increasing the permeability of the tumor vasculature and perfusion. HSPs engage in the immune response by attaching to immune surface receptors. Subsequently, the cell releases pro-inflammatory molecules, stimulating DCs and macrophages because they act as a damage-associated molecular pattern. Therefore, HT can reduce the immune-suppressed state of the tumors and increase immunotherapy effectiveness [51].

1.5.5.2 Adaptive Immune System

One of the mechanisms by which HT stimulates the adaptive immune system is through activating HSPs. HSPs carry the chaperoned tumor proteins to antigen-present cells. These cells, in turn, evoke a tumor-specific T-cell response which presumably can attack all tumor cells. Some studies also suggest the activation of B-cells after treatment with HT [51].

Tumor cells under heat stress also release more exosomes. Exosomes are the means of communication between the tumor and the immune system and contain protein, RNA, and DNA of the cell that secrete them. They are part of the mechanisms cancer cells use to create an immunosuppressive microenvironment enabling the disease to progress. Recent studies have shown exosomes can also stimulate both innate and adaptive immune systems. Exosomes containing genetic materials from cancer cells can deliver antigens to DCs, and activate T-cell responses against cancer [53].

One of the challenges is to uniformly heat the tumor area in the HT temperature range. However, from an immunotherapy perspective, the heterogeneity can be beneficial. The temperatures above 42 °C can result in direct cell kill through necrosis, and the mild temperature will be stimulating the immune response. Various studies have shown that enhanced immunogenicity induced by HT has yielded significantly improved radiosensitization [52,54]. Enhanced HT-induced immune response has also shown positive effects combined with chemotherapy and immunotherapy.

1.5.6 Hyperthermic Cell Death in Different Phases of the Cell Cycle

M-phase is the most sensitive to heat between the phases of the cell cycle. Heat in M-phase can damage the cellular mitotic apparatus leading to inefficient cell division [55, 56]. S-phase is also very sensible to HT treatment. In this phase, HT directly inhibits multiple processes related to the replication and result in chromosomal damage [57, 58]. G2-phase is somewhat sensitive to hyperthermia but is most sensitive to ionizing radiation. HT enhances radiation-induced cell cycle arrest in G2 and M phases which causes tumor cell apoptosis. G1-phase cells are relatively heat resistant and do not show any damage [56]. HT modulates cell cycle checkpoints which can increase the tumor cell radiosensitivity.

1.5.7 Treatment Methods of Hyperthermia

HT application is divided into three main categories of local, regional, and whole-body. Employing any of these methods depends on the body part being treated, the stage of cancer, and the energy distribution technique [59].

1.5.7.1 Local HT

Local HT applicators are used for small (up to 5-6 cm) superficial tumors or on intraluminal or endocavitary tumors near available body cavities such as the rectum, prostate, cervix or, esophagus [60, 61]. The applicators are placed on the surface of the superficial tumor with contacting layer called a bolus. Water boluses are usually used to keep the surface temperature at about 37 °C to avoid side effects. Microwaves, radio waves, or ultrasound are the most frequent applicators for local HT [62].

1.5.7.2 Regional HT

Regional HT is mainly used to treat deep-seated tumors that are inoperable. Tumors such as cervical and bladder cancers are of these types. Additionally, regional HT is used to treat larger parts of the body compared to Local HT, such as the pelvis, abdomen, or thighs [63]. The main methods used in regional HT are heating the tumors with peripheral applicators (intrinsic), heating organs with thermal perfusion (thermal), and constant hyperthermic peritoneal perfusion. In regional perfusion HT, blood is removed, heated, and inserted back into the body, usually with chemotherapy agents. This combination is referred to as hyperthermic intraperitoneal chemotherapy. In some other methods of regional hyperthermia, dipole antennas are placed around the patient's body, and the heat is produced through microwave or radio waves. The target tissue can be heated up to 41-42 °C.

1.5.7.3 Whole Body HT

Whole-body HT (WBH) is achieved by radiation or extracorporeal technologies to increase the body temperature to 41 °C. Common methods of WBH are hot water immersion and ultraviolet radiation. In radiant WBH, the body is heated through heating blankets, inductive loops, thermal chambers, or hot wax. In the extracorporeal methods, WBH is achieved by extracting the blood and heating it by passing through hot air or water bath and then reinserting it to the main vein. Through the WBH, depending on the method that is being used, patients can ask for anesthesia. The whole process takes about four hours. Two hours to reach the target temperature, one hour for maintaining the target temperature and treatment, and one hour for the cool down process. Patients treated with WBH usually show side effects such as diarrhea, nausea, and vomiting. However, all of them are temporary side effects [64].

1.5.8 Modalities of Hyperthermia

The effectiveness of the HT depends on the modality being used, stage of the cancer and the biological response of the patient. Some of more widely used HT modalities are ultrasound, microwave, radiofrequency, and magnetic hyperthermia which will be briefly discussed here.

1.5.8.1 Ultrasound

Ultrasound is a high-frequency mechanical wave. It provides heat through mechanical friction when it is focused and applied to a specific area. Ultrasound has adequate tissue penetration at a wavelength that allows beam shaping and focusing. The penetration depth can be adjusted to between 1 cm to 20 cm, appropriate for superficial and deep-seated tumors [65]. Ultrasound devices have evolved in four generations [66]. The fourth and most advanced generation of ultrasound devices can generate high-intensity focused ultrasound (HIFU), which can precisely and rapidly heat a target with various shapes and sizes to an ablative temperature while sparing the surroundings. The temperature distribution can be monitored with MRI in real-time [67, 68].

The modes at which HIFU destructs the cells in the tumor are mainly thermal and mechanical. HIFU imposes thermal cell destruction, by increasing the temperature above cell toleration limit, and mechanical cell destruction by oscillating and collapsing the gas-filled cavities, increasing the cell membrane permeability, and radiosensitizing the tumor cells noninvasively [69]. The main disadvantage of the ultrasound techniques is high absorption by bone and high reflection from air-filled areas such as the respiratory tract and gastrointestinal tract.

1.5.8.2 Hyperthermia through Electromagnetic Waves

Electromagnetic Hyperthermia includes a group of modalities that either depend on electric or magnetic fields or electromagnetic radiation which we will discuss in current section.

Microwave

Microwave is electromagnetic radiation with a frequency range between 0.3 GHz to 300 GHz. The microwave radiation can be focused on the tumor tissue by using an array of antennas adjacent to the patient body. The number of antennas depends on the depth and size of the tumor. Microwaves are non-ionizing radiation that transfer their energy by interacting with dipole molecules in the target tissue. Among dipole molecules, water absorbs most of the power. The water molecules oscillate with the same frequency as the alternating radiation fields. Simultaneously, they lose some of their energy in the form of heat due to friction with adjacent molecules. Tumor cells tend to heat faster because of their high water content [70, 71].

Electromagnetic waves attenuate faster in the tissue when the frequency is higher; therefore, microwaves work better for superficial tumors. For deep-seated tumors, the frequency should be decreased. These low-frequency microwaves might not have enough energy to deposit in the tissue; therefore, more antennas should be added. This process requires high precision to avoid heating any healthy tissue [72].

Radiofrequency

The range of radio waves frequency is 3 kHz to 300 MHz. Radio wave heating is applied by two different modalities, denoted as capacitive heating and inductive heating. Capacitive heating is performed by placing two electrodes above and below the patient. The electric field oscillates with a frequency of a few million times per second, and the water molecules rotate with the same frequency and generate friction-like heating. This modality can be used to heat both superficial and deep-seated tumors. However, it also deposits a significant amount of energy in the subcutaneous fatty tissue due to its high resistivity. The power delivered to the tissue depends on the electrodes' size and orientation, and blood perfusion plays a vital role in diffusing the heat [73, 74].

Inductive modality uses a magnetic field to deliver energy to the tumor tissue. The patient is placed inside a coil (with no contact with the applicator), and a secondary coaxial magnetic system is used to improve the power. Moving the applicator along the coaxial axis delivers uniform energy to the patient body. The alternating magnetic field generates heat by generating Eddy current. This modality can provide limited power to the target tissue [75, 76]. The human body's variable and inhomogeneous thermoregulation presents a challenge to distributing power uniformly. To optimize the power distribution the temperature should be closely monitored.

Magnetic Hyperthermia

Magnetic HT uses magnetic fields and ferromagnetic materials to generate heat. The mechanisms through which heat can be produced are Eddy currents, Hysteresis losses, and relaxation losses. The ferromagnetic materials are placed in the treatment area either as nanoparticles (NPs) or as ferromagnetic seeds to deliver the heat to a targeted area.

Ferromagnetic materials consist of small domains, each possessing a net magnetic moment. When subjected to an external alternating magnetic field, these magnetic moments align with the applied field. The magnetization responds nonlinearly when the field direction is reversed, as explained by the hysteresis loop. Key parameters on the hysteresis loop include saturation magnetization, representing the magnetization at a high field limit when all regions align with the magnetic field; remanent magnetization, indicating the remaining magnetization in the absence of a field; coercivity, denoting the field required for complete demagnetization. The area under the loop represents the amount of heat generated in a cycle of the alternating field through eddy current and hysteresis losses. [77, 78].

In the case of ferromagnetic NPs, thermal effects have the potential to override the influence of magnetization, causing the orientation of the net magnetization to randomly flip from its equilibrium state. This phenomenon can occur either due to the Brownian motion and physical rotation of the particles in a fluid or because of changes in the orientation of individual spins within the NP. Another process that contributes to heat generation is Neel relaxation. When a particle is subjected to a rapidly alternating field, its magnetic moment oscillates at the same frequency. However, the rapid alignment faces opposition from the crystalline structure of the particle, resulting in the generation of heat. [79, 80].

The contribution of each of these heat production mechanisms to the total heat depends highly on the type of particle. In the case of Ferromagnetic seeds, which will be discussed shortly, the relaxation losses do not play a role at all, and the hysteresis losses depend on the composition of the seed. For NPs, however, all of the above can be significant in determining total heat generation.

It is worth noting that in an alternating magnetic field, eddy currents are also generated in the body tissue; however, the amount is eight orders of magnitude smaller than in metals. [81].

Ferromagnetic Seeds

Burton et al. [82] was the first group to suggest using self-regulating implants for interstitial HT. The implants are usually in the shape of a needle and made of ferromagnetic materials.

Ferromagnetic materials have a permanent magnetic moment in the absence of a magnetic field and, when placed in the magnetic field, show strong magnetism in the direction of the field. Ferromagnetic materials lose their magnetic properties sharply at a critical temperature denoted by Curie temperature [83]. The value of the Curie temperature depends on the substance of the ferromagnetic material. The loss of magnetic properties regulates the temperature by losing their magnetic properties and become paramagnetic. Therefore ferromagnetic core simultaneously amplifies the magnetic field and self-regulates the temperature.

The encouraging properties of ferromagnetic materials make them a great candidate for permanent implants for multiple heating sessions. The inherent self-regulation of ferromagnetic materials mitigates concerns related to tissue overheating, eliminating the need for invasive temperature monitoring loops and feedback mechanisms. Unlike methods such as microwaves and ultrasound, inductive heating circumvents the issue of bone penetration.

The implants need to be biocompatible, i.e. it has to be composed of biocompatible elements such as C, O, N, Na, Mg, Si, K, Ca, Ti, and Fe [84]. The computations have shown the heat production rate of 200 $\mathrm{mW\,cm^{-1}}$ is adequate for most clinical applications [85].

1.5.8.3 Nanoparticles

NPs are particles with a diameter ranging from 1 to 100 nm. Recent advancement in the field of NPs, enables precise adjustments to the surface of these particles, enhancing their interaction and efficacy in interfacing with biological systems. In the NP technique, the NPs may either be infused in the target tissue, and an external source is used for heating, or they are administered intravenously, in which the NPs can accumulate preferentially in tumors via enhanced permeability and retention [86].

Among NPs, gold and superparamagnetic ferrite oxides are most widely used, each with its own advantages. Gold can respond to a wide range of heat sources such as radiofrequency and ultrasound, and iron oxides show strong magnetic properties when placed in a magnetic field [87–90].

Although the use of NPs can be very beneficial in the case of deep-seated tumors and can provide uniform heat to the target if appropriately administered, increased toxicity might occur depending on the size of the particles and their composition [86]. In addition, an alternating magnetic field is usually applied to the entire body, which results in heat generation in other parts of the body due to NPs not being concentrated in the tumor.

1.5.9 Cumulative Equivalent Minutes at 43 °C

In most studies, HT is applied at different temperatures in various durations making comparison of thermal doses and results very difficult. Unlike RT in which the specific prescription does, dose per fraction, and overall treatment time to various tumors are mandatory, HT did not have such a mandate. Sapareto and Dewey [91] proposed the concept of thermal isoeffect dose to convert one-time temperature combination to a standard level, by converting time-temperature data to the equivalent minutes for 43 °C, known as cumulative equivalent minutes at 43 °C (CEM43 °C). As it will be discussed shortly, it appears that this parameter directly correlates with the treatment outcome [92]. Furthermore, CEM43 °C is now recommended as the standard for reporting thermal dose. It can also be calculated by using the below formula:

$$\text{CEM43°}C = \int_0^t R^{43-T(t)}\mathrm{d}t[\text{min}] \tag{1.1}$$

Here T is the applied temperature of the target tissue and R is the factor to compensate for a 1 °C temperature change. The value of R is experimentally determined it is set to 0.5 for T>43 °C, and 0.25 for $T \leq 43$ °C.

Several points can be deduced by looking at cell death versus the duration of the HT treatment for various temperatures. Firstly, for the temperatures below 42.5 °C, the cell kill clearly reaches a plateau. This means mild HT can only effectively induce a cell kill for a short time, and after that, the cell kill rate will not increase significantly due to thermotolerance. Therefore, there needs to be 48-72 hours time interval between the application of HT to avoid the effects of thermotolerance. It should be noted that the thermotolerance only affects the cell kill and not the radioresistivity, and therefore it does not reduce the effect of combined HT and RT. Secondly, the two separate cell kill processes by HT, as 42.5 °C marks the border of two very different cell kill rates. Above 42.5 °C the cell kill exponentially increases (necrosis), and below 42.5 °C cell kill reaches a plateau very soon (apoptosis diminished by thermotolerance). Also, the shoulder in the survival curve indicates accumulation of sub-lethal heat damage, and changes into a straight line represent a constant rate of cell death [56, 93, 94].

1.5.10 Safety Limits

Probably the single most important point in any type of treatment is the patient's safety. Different techniques have different quantities for safety evaluation. In the case of electromagnetic HT, one needs to study whether there is any non-specific heating or other damaging effects that might occur on the body when it is placed in an alternating magnetic field known as specific absorption rate (SAR). SAR is defined as the amount of absorbed electromagnetic energy by an object per unit mass (units of $\mathrm{W\,kg^{-1}}$), is widely accepted for electromagnetic field effects characterization [95–97] and it is defined as

$$\mathrm{SAR} = \frac{\sigma E^2}{\rho} \tag{1.2}$$

where E is the electric field ($\mathrm{V\,m^{-1}}$), σ is the conductivity ($\mathrm{S\,m^{-1}}$), and ρ is the mass density of the tissue ($\mathrm{kg/m^3}$). SAR is a useful value for quantifying the interactions of RF/microwave fields with living systems. SAR implicitly depends on frequency, size, and configuration of the anatomical region. National/international safety regulations set the upper limit on SAR such that the increase in tissue temperature does not cause harmful physiological effects. For diagnostic MRI, the maximum used frequency, and magnetic field are $\sim$ 128 MHz, and 3 T, respectively. No physiological consequences for values of SAR $\sim 4\ \mathrm{W\,kg^{-1}}$ during MRI procedures have been found. We will limit electromagnetic field parameters that satisfy the safety criterion [98].

The rate of power generation per unit volume due to eddy current in tissue can be found from

$$P = \sigma \left(\pi \mu_0 H f\right)^2 r^2 \tag{1.3}$$

where r is the radius of human body. Atkinson [99] studied the eddy current effects based on the frequency (f) and the strength of the magnetic field (H). His results, often referred to as the 'safety limit', is the base of the "Brezovich criterion" which states the product of amplitude and magnetic field frequency $H \times f$ should not exceed $4.85 \times 10^8\ \mathrm{A\,m^{-1}\,s^{-1}}$ as can be seen below

$$\mathrm{SAR} = \frac{\sigma \left(\pi \mu_0\right)^2 (Hf)^2 r^2}{\rho} \Rightarrow H \times f \approx 4.85 \times 10^8 \mathrm{A\,m^{-1}\,s^{-1}} \tag{1.4}$$

where we have used $\sigma = 0.012\ \mathrm{S\,m^{-1}}$ [100], $\rho = 930\ \mathrm{kg/m^3}$, and $r \approx 29\ \mathrm{cm}$ [101]. While it is possible to increase the filed amplitude for higher power generation, it should be noted that frequencies lower than 50 kHz can result in nerve stimulation [85].

1.5.11 Side Effects of HT

Side effects of HT highly depend on the technique being used and the body part that is being treated. Simple skin burns and skin pain due to HT often heal, but excessive heating with the purpose of delivering heat to deep tissue can cause more serious side effects [15]. Whole body hyperthermia, which is more invasive, can cause dehydration, heat illness, cardiac disease, or thrombosis depending on the underlying physical condition. If the temperature does not exceed 44 °C, it rarely affects normal tissue, and in general, HT does not have any adverse effects. In very rare cases of chemotherapy, depending on drug efficacy, HT can increase the toxicity. Overall, the side effects are transient [15].

1.6 Hyperthermia as Adjuvant Treatment

Many studies have recently demonstrated that an optimal heat effect has anticancer potential and can improve the performance of various cancer treatments [41, 129]. Although it can be used alone and results in impressive shrinkage and even complete elimination of tumors, it usually does not last, and the tumors regrow. Combining HT with other therapeutic modalities, including chemotherapy and RT, has yielded higher complete and durable responses. HT in combination with RT or chemotherapy has been studied in several clinical studies [102–113]. Positive results with HT have been reported in systematic reviews and meta-analyses [114–116]. From 38 clinical studies of HT combined with RT vs. RT alone on 3478 patients with diverse tumor locations (RT, $n = 1717$; HT and RT, $n = 1761$), an overall complete response of 54.9% for HT combined with RT vs. 39.8% with RT alone was reported [117].

There is evidence that HT-induced immunogenicity can enhance the abscopal cytotoxicity of tumor cells and increase the radiation efficacy. Abscopal effect is referred to the process in which applying radiation at a distance from tumor suppresses the tumor progression. This is as systemic outcome that is cause by the immune system [118].

The effectiveness of HT is quantified by thermal enhancement ratio (TER), defined as the ratio of the respective radiation doses of RT alone divided by the combined RT and HT doses necessary to receive equal survival. [25].

TER for simultaneous application of RT and HT is linearly dependent on the heat dose and can sometimes be enhanced 5-fold compared to RT alone. However, it attains same values both in the tumor and healthy tissue. Studies show that by increasing the sequence time between HT and RT, TER plateaus to a value around 1 for healthy tissue and to 2 for tumor. Consequently, currently HT and RT are applied sequentially in clinical treatments, to ensure tumor-selective radiosensitization [119, 120].

1.6.1 Synergistic Effects of HT

Mild HT increases the blood flow and increases the oxygenation of the tumor cells, therefore, making them more vulnerable to radiation. Mild HT enhances the RT by direct cell kill through apoptosis and blocking DNA repair pathways. According to simulations, the additional effect of HT to RT total dose is about 10 Gy, meaning the same effect can be achieved with less radiation in the presence of HT [121, 122]. Therefore, it is expected that by combining RT with HT, due to the aforementioned positive effects of HT, such as radiosensitizing cells, the survival curves needs to be revisited, and the value of either single stand breaking coefficient (α) or double strand breaking coefficient (β) in the Linear Quadratic model should be increased

$$\frac{S(D)}{S(0)} = \mathrm{e}^{-\left(\alpha D+\beta D^2\right)} \tag{1.5}$$

where $S(D)$ fraction of cells to survive at exposure dose D. The first term in parenthesis represents the probability of cell death arising from a single hit producing a single-strand break and the second term represents the probability of cell death arising from double-hit events producing a double-strand break.

The synergistic effects of HT on chemotherapy and drug activation depend highly on the drug being used. Synergistic effects can be categorized into independent action in which the activation does not show any correlation with temperature; additive, in which the increase in temperature increases the activation of the drug showing positive correlation; and synergistic, in which the drug and temperature are complementary.

As discussed before, mild HT increases the blood flow and enhances drug delivery. HT at higher temperatures increases the possibility of heat-induced hypoxia in tumors and improves the effectiveness of certain drugs that are specifically cytotoxic to hypoxic cells. By combining chemotherapy and HT, the TER can be anywhere in the range of 1 to 3.6.

1.6.2 DNA Repair

HT as a standalone modality does not induce DNA damage; however, it can influence and hinder DNA repair pathways. Ionizing radiation is known to cause DNA damage, manifested as double-strand breaks (DSB) and single-strand breaks (SSB). Although DSBs occur at a lower rate, they are more lethal to cells. Unrepaired SSBs can lead to DSB formation. Consequently, disrupting SSB repair mechanisms is likely to yield therapeutic gains [123].

SSBs can be repaired through three distinct pathways: homologous recombination, classical non-homologous end joining, and alternative non-homologous end joining [124–127]. By increasing the temperature above 41 °C, HT can inhibit these repair mechanisms and DNA polymerase key enzymes in a multistep repair system.

1.6.3 Radiation-Heat Sequence

The best radiosensitization effects are observed at simultaneous application of HT and RT, and the effects decrease as the time interval between the modalities increases. Reduction in radiosensitivity over time is observed mainly because most DNA repairs happen between 4-6 hours after radiation. Therefore, for maximum effectiveness, HT should not be applied in an interval larger than 2 to 4 hours in sequence with RT [56] when simultaneous application is impractical. The TER for simultaneous application of HT and RT is 2-3 times higher than sequential application [128]. To maximize the therapeutic impact on the tumor and minimize toxicity to healthy tissue, it is essential to select the maximum achievable Target Enhancement Ratio (TER) for the tumor while keeping the TER for healthy tissue at a minimum [129].

1.7 Clinical Status of Adjuvant Synergistic Hyperthermia Therapy

Multiple phase II and phase III clinical trials where focused on the synergistic effect of HT specifically on hyperthermic intraperitoneal chemotherapy after cytoreductive surgery (HIPC) topic. These trials include local, interstitial, regional, and whole body techniques combined with both chemotherapy and RT [130–132]. These studies continuously show the positive impact of HT. Despite all the enhancement HT is still not used very frequently in clinical settings for cancer treatment.

To summarize, the ferromagnetic seeds that are used in interstitial HT, do not provide enough power to raise the temperature of the tissue to the desired temperatures. On the other hand the other methods of hyperthermia either have side effects and cannot localize the heat in the tumor area uniformly or logistically it is difficult to use them simultaneously with radiation.

In this study we have designed a novel thermo-brachytherapy (TB) seed that combines an LDR radioactive source with an HT source utilizing a ferrite core in magnetically mediated heat production. We present experimental measurements of the relative permeability for a soft ferrite core with MnZn(Fe_2O_4) formulation as a function of temperature.

Ferrimagnetic materials generate heat through hysteresis loss, but it is not enough for treatment due to small saturation magnetization. For this reason, ferrimagnetic materials are usually placed in a metallic sheath which will host a significant amount of Eddy current and generate much more heat than the hysteresis loss [83]. The hysteresis loss only accounts for a few percent of the total heat generated by the implant. The hyperthermia-only (HT-only) seeds to be used in empty spacers between radioisotope seeds for a uniform heat distribution.

Combining heat with radiation in a TB treatment may provide an effective and safe intensification strategy,which would have important implications in the radiation salvage setting. Moreover, with advanced functional imaging, such as Prostate-Specific Membrane Anti-gen Positron Emission Tomography (PSMA-PET) scan devices can detect locally recurrent prostate cancer and the need for salvage strategy considerably earlier.

PSMA-PET is a relatively new technique that targets PSMA, a transmembrane protein that exists on prostate cells, and its level increases as the degree of dysplasia rises [133,134]. Evidence for the usefulness of PSMA-PET, particularly those employing 68-Gallium based radioligands, has accumulated over the last few years. This imaging modality showed excellent potential for determining the site of disease in recurrence post-treatment setting, recognizing lymph node and bone metastases, and even in identifying the dominant lesion for primary staging. PSMA-PET has moderate sensitivity and excellent specificity for assessing local tumor extent in patients with PCa [135–138].

The TB seed structure is optimized with respect to conductive sheath thickness and material, which is in turn used in a finite element analysis (FEA) solver for a set of seeds implanted in a pattern representative of a real patient case. We have shown that by replacing brachytherapy seeds with TB seeds and using additional HT-only seeds within the same needles in a clinical patient plan, sufficient heat coverage can be achieved even in the presence of physiologic rates of blood perfusion.

Chapter 2

Theoretical Background

2.1 Seed Design

We designed the TB seed based on a standard commercial ^{125}I seed the BEST Model 2301 (Best Medical Inc. Springfield VA), with a few modifications. In our design, the tungsten marker is replaced with a ferrite core coated with a layer of organic iodine serving as a radioactive source. The core fills the space inside the capsule and iodine layer, removing the previously present air gap for additional heating power.

Ferrite is a ceramic substance made mostly of iron oxide (Fe_2O_3) with small quantities of metals, including barium (Ba), manganese (Mn), nickel (Ni), and zinc (Zn) from the ferrimagnetic family. Ferrites, in general, have a high permeability below a critical temperature, defined as Curie temperature, and a sharp drop-off in their magnetic properties at Curie temperature, providing self-regulating heat production [139]. In particular, we used soft ferrites, allowing for easier changes in magnetization and higher magnetic saturation.

The outer diameter (0.8 mm) and length (5 mm) of the seed are preserved in our design. The HT-only seeds on the other hand will only have the outer capsule, and the ferrite core will fill the entire interior (Figure 2-1). Their diameter (>0.8 mm) and length >5 mm) are by design slightly larger to be distinguished from the TB seeds in CT images facilitating a post-implant dosimetry evaluation. The thickness of the capsule will be optimized based on the ferrite core diameter and the material that is used to create the capsule.

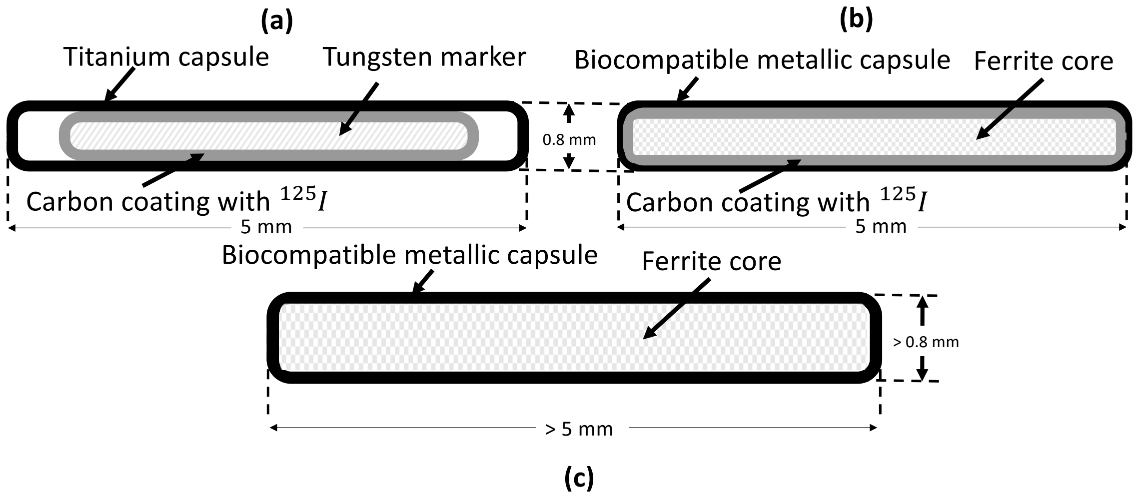

Figure 2-1: BEST ^{125}I, Model 2301 brachytherapy seed (a), the proposed TB seed (b), and HT-only seed (c), made larger to be distinguishable on CT scans.

When the seeds are placed in an alternating magnetic field, the ferrite core enhances the field amplitude and, consequently, the circulating eddy currents on the outer shell. The shell's resistance dissipates power and generates heat. Ferrite cores are also susceptible to eddy currents, but due to their low electrical conductivity, the power generated by the core itself is negligible and can be disregarded in comparison to the shell power. When the seed temperature exceeds the Curie temperature of the ferrite core, the core exhibits paramagnetic properties, as its relative permeability swiftly approaches unity. At this point, the ferrite core loses its ability to amplify the magnetic field, and accordingly, the eddy current on the shell decreases dramatically, thereby limiting the thermal power output. This characteristic of the ferrite core, known as thermal self-regulation, obviates the need for invasive thermometry.

Since the seeds are intended for use within the patient's body, it is essential that the shell material to be biocompatible. To generate more power, the capsule material should have a high electrical conductivity. Titanium and gold, or, in the second degree, their alloys with copper or silver, are the most biocompatible and electrically conductive materials.

2.2 Experimental Design for Magnetic Permeability Measurement

2.2.1 RL Circuits

A first-order series connected resistor-inductor (RL) circuit is composed of a resistor, and an inductor either in series with a voltage source or in parallel with a current source. RL circuits can be used to measure the inductance of an unknown inductor. In the case where the resistor and the inductor are placed in series (Figure 2-2) as in the current study, by measuring the voltage at each node of the resistor (R) and utilizing the circuit equations the inductance can be measured. Using an oscilloscope to conduct the measurements will introduce additional elements into the circuit, such as the intrinsic capacitance and a resistor associated with the signal input. Since the voltage source is producing a sinusoidal signal, there will be imaginary parts to the voltage and current, therefore we start by calculating the impedance across the inductor

$$\mathbf{Z}_L = \frac{1}{\frac{1}{R_0} + \mathrm{j}\omega c_0 + \frac{1}{R_L + \mathrm{j}\omega L}} = \frac{R_0(R_L + \mathrm{j}\omega L)}{R_L + \mathrm{j}\omega L + \mathrm{j}\omega c_0 R_0 R_L - \omega^2 c_0 R_0 L + R_0} \tag{2.1}$$

and the total impedance

$$\mathbf{Z}_{\text{tot}} = \mathbf{Z}_L + R = \frac{R_0(R_L + \mathrm{j}\omega L)}{R_L + \mathrm{j}\omega L + \mathrm{j}\omega c_0 R_0 R_L - \omega^2 c_0 R_0 L + R_0} + R \tag{2.2}$$

where $\mathrm{j} = \sqrt{-1}$, R_L and L are the intrinsic resistance and inductance of the inductor, R_0, and c_0 are the oscilloscope resistance and capacitance, R is the resistor in the RL circuit, and ω is the angular frequency of the applied voltage. Finally, we have

$$\frac{\mathbf{V}_B}{\mathbf{V}_A} = \frac{\mathbf{Z}_L}{\mathbf{Z}_{\text{tot}}} = \frac{R_0(R_L + \mathrm{j}\omega L)}{R_0(R_L + \mathrm{j}\omega L) + RR_0 + RR_L + \mathrm{j}R\omega L + \mathrm{j}\omega c_0 R_0 R R_L - \omega^2 R c_0 R_0 L} \tag{2.3}$$

where $\mathbf{V}_A$ and $\mathbf{V}_B$ are the complex input voltage and voltage across the inductor. This equation can be separated into imaginary and real parts

$$\frac{|\mathbf{V}_B|}{|\mathbf{V}_A|}\cos(\phi_B - \phi_A) = \frac{R_o^2 R_L^2 + R_o^2 R_L R + R_o R R_L^2 + \omega^2 R_o^2 L^2 + \omega^2 L^2 R_o R}{(R_o(R_L + R - \omega^2 R c_o L) + RR_L)^2 + (\omega L(R_o + R) + \omega c_o R_o R R_L)^2} \tag{2.4}$$

$$\frac{|\mathbf{V}_B|}{|\mathbf{V}_A|}\sin(\phi_B - \phi_A) = \frac{R_o^2 R\omega L - \omega^3 R_o^2 R c_o L^2 - \omega R_o^2 R R_L^2 c_o}{(R_o(R_L + R - \omega^2 R c_o L) + RR_L)^2 + (\omega L(R_o + R) + \omega c_o R_o R R_L)^2} \tag{2.5}$$

where $|\mathbf{V}_A|$ and ϕ_A are the amplitude and phase of the voltage at node A, and $|\mathbf{V}_B|$ and ϕ_B are the amplitude and phase of the voltage at node B. By solving the two algebraic equations above for the two unknowns (R_L, L) we can find the inductance and resistance present in the circuit.

The above equation can be simplified for the purposes of this study because $R_o \gg R \gg R_L$ and $1/(\omega c_o) \approx 10^6\ \Omega \gg R \gg R_L$

$$\frac{|\mathbf{V}_B|}{|\mathbf{V}_A|}\cos(\phi_B - \phi_A) = \frac{R_L^2 + R_L R + \omega^2 L^2}{(R_L + R)^2 + (\omega L)^2} \tag{2.6}$$

$$\frac{|\mathbf{V}_B|}{|\mathbf{V}_A|}\sin(\phi_B - \phi_A) = \frac{R\omega L}{(R_L + R)^2 + (\omega L)^2}. \tag{2.7}$$

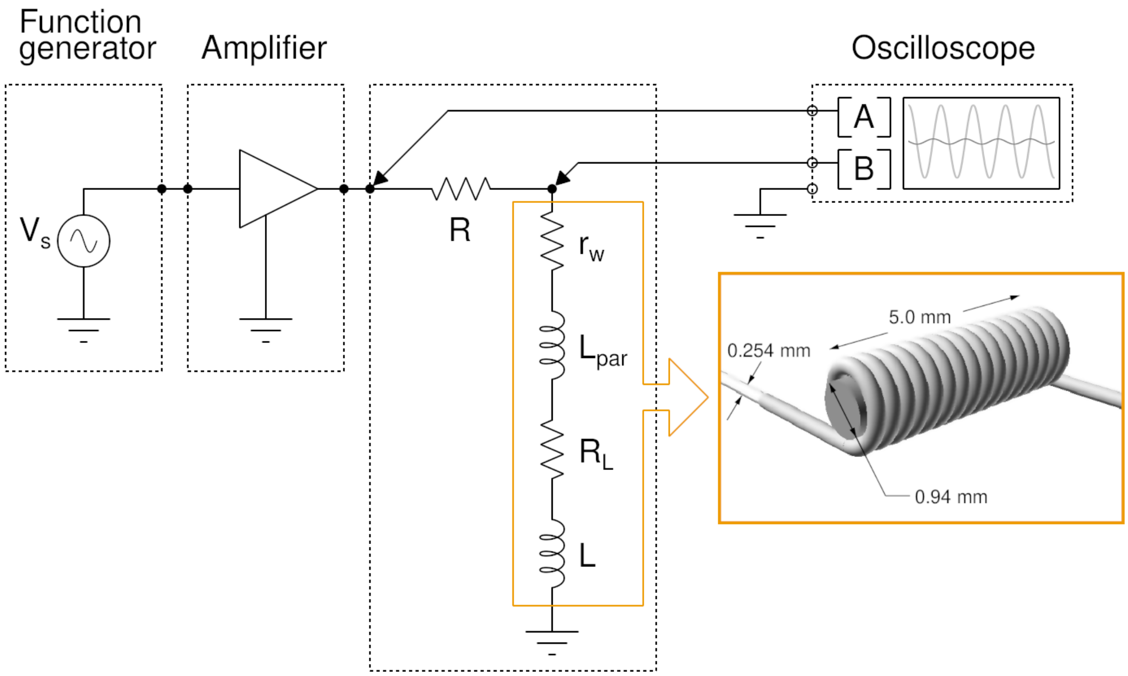

Figure 2-2: Series connected RL circuit used to derive ferrite core permeability. $R = (1.0 \pm 1\%)\ \Omega$, 10 ppm/°C, 2.5 W. The winding resistance of the copper wire (r_w), series loss resistance resulting from the complex permeability (R_L), and self-inductance of the cored or core-less solenoid (L) were used to model the non-ideal inductor. L_{par} was used to model parasitic inductance from external wiring. The physical properties of the solenoid and ferrite core used are depicted in the inset.

2.2.2 Inductance of a Practical Coil

Inductance of an ideal coil, i.e. a very long current-sheet coil at low frequencies, can be calculated by using Ampere's law due to its symmetry

$$\begin{cases} \Phi = LI = NBA_c \\ \oint B.d\ell = \mu_0 NI \end{cases} \Rightarrow L = \frac{\mu_0 N^2 A_c}{\ell_c} \tag{2.8}$$

where μ_0 is the permeability of the free space, Φ is the magnetic flux, B is magnetic flux density, A_c is the cross-sectional area of the coil, ℓ_c is the coil length, and N is the number of turns in the winding.

In practice, the above assumptions are not applicable anymore, due to broken axial symmetry, leakage of the magnetic field outside the coil, high frequency, round wire, etc. Therefore, Equation (2.8) requires significant corrections.

In the following we will discuss some of the contributing correction factors to the inductance.

2.2.2.1 Skin Effect

The skin effect delineates the boundary between the low- and high-frequency regimes, where the dependence of inductance and resistance on frequency becomes noticeable. The inductor's alternating current generates an alternating magnetic field, which in turn produces eddy current. The eddy current negates a portion of the main current, thereby creating a zero-sum area (area with no current). At high frequencies this cancellation is more significant and the main current flows near the surface of the inductor. The thickness of the layer in which the current is flowing can be calculated by the characteristic length known as the skin-depth (δ)

$$\delta = \sqrt{\frac{2}{\sigma\omega\mu}} \tag{2.9}$$

where ω is the angular frequency of the magnetic field, σ is the conductivity, and μ is the permeability of the conductor. The skin effect reduces the effective area of the conductor and therefore increases the effective resistance. The skin effect decreases the conductor's internal inductance by diminishing the current in the bulk of the conductor. In our study, we used a copper wire with radius of $r_w = 0.127$ mm. Plugging the values for copper in the above equation we obtain $\delta = 0.292$ mm$> r_w$

at frequency of 50 kHz, indicating no skin effect in our measurements.

2.2.2.2 Internal Inductance

Internal inductance is due to magnetic energy stored within the body of the inductor (i.e. the wires), and since it depends on the current distribution within the body of the wire, it decreases with increasing frequency and appearance of the skin effect. Even though increasing frequency diminishes the internal inductance, the correction is still significant for the thinner wires in the lower end of the high-frequency region (see Figure 2-3). In contrast to external inductance which is proportional to N^2, internal inductance, depends on N, and that is because it depends linearly on the length of the conductor (ℓ_w) [140]

$$L_i = \frac{\ell_w \mu_w}{8\pi} \Theta\left(q\right) \tag{2.10}$$

where $q = \frac{d_w}{\delta\sqrt{2}}$, μ_w is the permeability of the wire, d_w is the wire diameter, and

$$\ell_w = \sqrt{(\pi d_c N)^2 + \ell_c^2} \tag{2.11}$$

where d_c , and ℓ_c are the diameter, and length of the coil respectively, and

$$\begin{aligned} \Theta(q) &= \Theta_\infty(q)[1 - \exp(-\Theta_\infty(q)^{-1.5819})] \\ \Theta_\infty(q) &= \frac{4}{\sqrt{2}q}\left[1 + \frac{0.01209}{q+1} - \frac{0.63523}{q^2+1} + \frac{0.16476}{q^3+1}\right]. \end{aligned} \tag{2.12}$$

The ratio of the wire radius r_w and the skin depth can be used to understand whether we are working in a high frequency region i.e., the internal inductance value is negligible, or we are still in a sufficiently low frequency region for the internal inductance to be significant.

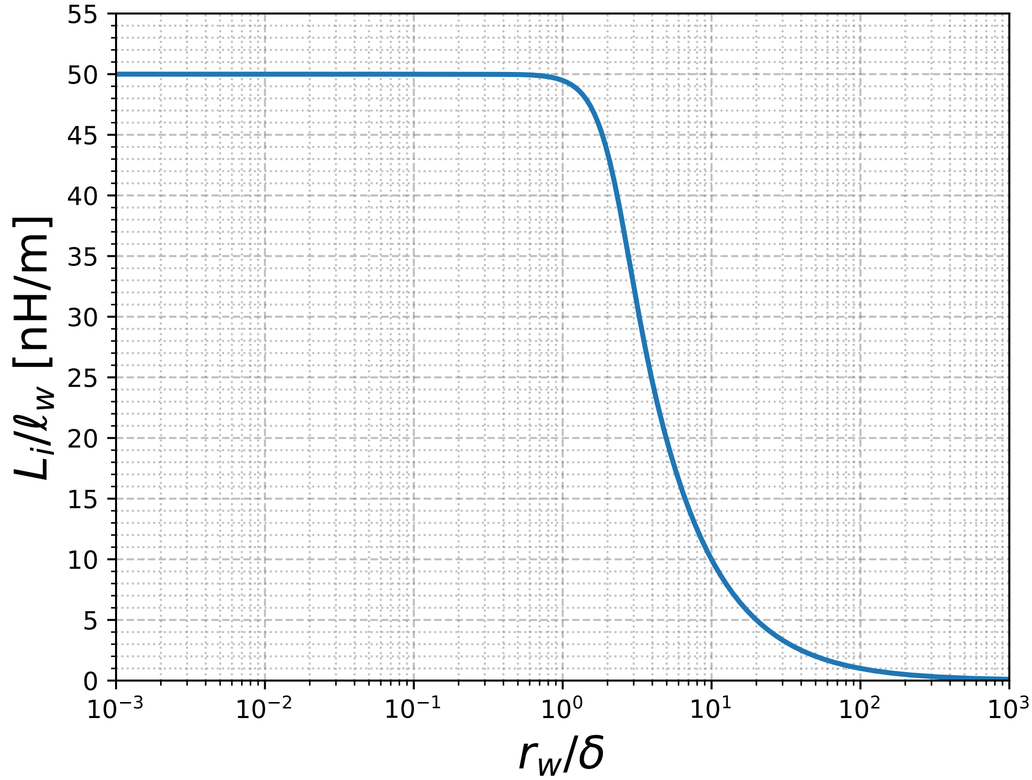

Figure 2-3: The internal inductance per unit length. The internal inductance diminishes quickly when the skin effect becomes prominent. The important limit $r_w = \delta$ happens at approximately $f = 263$ kHz.

2.2.2.3 Effective Diameter

When determining the inductance, the coil's effective diameter is a significant factor. The effective diameter of the coil can be affected by the curvature of the loops, the skin effect, and the effect of adjacent current loops on each other's current distribution, also known as the proximity effect, with the latter two being more pronounced in the high-frequency domain. In a loop of winding, the outer diameter is greater than the interior diameter, causing the wire to stretch. The difference in length produces a gradient in the wire's resistance and, consequently, a gradient in the current distribution with more current near the inner radius and less near the outer radius.

As a result, effective coil radius is bounded between $r_a \pm r_w$ where r_a is the distance from the central axis of the coil to the center of the wire. The effective diameter of the coil (d_∞) is obtained from a semi empirical formula [141]

$$d_\infty = \frac{d_a + d_{\min}\frac{a}{(p/d_w)-1}}{1 + \frac{a}{(p/d_w)-1}} \tag{2.13}$$

where $p = \ell_c/N$ is the pitch, a is an experimental constant value and it is chosen such that it has somewhat more bias towards $d_{\min}$ to consider the gradient. $d_{\min}$ is the lower limit on the coil effective diameter, and can be calculated by assuming two turns with diameter d_0 at two ends, where d_0 is the diameter at low frequency, and $N-2$ turns with diameter $d_a - d_w$

$$d_{\min} = \frac{(N-2)(d_a - d_w) + 2d_0}{N} \tag{2.14}$$

and

$$d_0 = d_a \left[1 - \left(\frac{d_w}{d_a}\right)^2\right] \tag{2.15}$$

It can be seen that at the limit $d_w \ll d_a$ we will have $d_0 \approx d_a$ and $d_{\min} \approx \frac{N+1}{N} d_a$ and therefore for a large number of turns where pitch is effectively zero, we will also have $d_\infty \approx d_a$.

2.2.2.4 Round Wire Correction

Since the wires have dimensions in a real situation, additional corrections are required for the difference between self-inductance, and mutual inductance of loops of round wire compared to single-turn current sheet and loops of current sheet respectively. According to Rosa [142], the round wire external inductance correction can be implemented by calculating a dimensionless coefficient

$$\kappa_s = \ln\left[1 + \frac{\pi d_c}{2p}\right] + \frac{1}{f\left(\frac{p}{d_c}\right)} - \ln\left(\frac{8d_c}{d_w}\right) + 2 - \frac{1}{8}\left(\frac{d_w}{d_c}\right)^2\left[\ln\left(\frac{8d_c}{d_w}\right) + \frac{1}{3}\right] \quad (2.16)$$

where

$$f(x) = \frac{1}{\ln\left(\frac{8}{\pi}\right) - \frac{1}{2}} + 3.437x + \frac{24}{3\pi^2 - 16}x^2 - \frac{0.47}{\left(0.755 + \frac{1}{x}\right)^1.44}. \quad (2.17)$$

Mutual inductance corrections can be incorporated with a separate dimensionless coefficient

$$\kappa_m = \frac{4}{N}\sum_{m=1}^{N-1}(N - m)\left[\frac{K(\alpha_s) - E(\alpha_s)}{\sqrt{\alpha_s}} - \frac{K(\alpha_w) - E(\alpha_w)}{\sqrt{\alpha_w}}\right] \quad (2.18)$$

where N is the number of turns, $E(x)$, and $K(x)$ are elliptical integrals of the first and second kind respectively, and

$$\alpha_s = \frac{\sqrt{1 + \left(\frac{d_c}{g_s}\right)^2} - 1}{(\sqrt{1 + \left(\frac{d_c}{g_s}\right)^2} + 1} \quad (2.19)$$

$$\alpha_w = \frac{\sqrt{1 + \left(\frac{d_c}{g_w}\right)^2} - 1}{\sqrt{1 + \left(\frac{d_c}{g_w}\right)^2} + 1} \quad (2.20)$$

and $g_s = mp$, $g_s = g_w \exp(-\gamma_m)$, and finally

$$\gamma_m = (m^2 + 1)\ln(m) + \frac{3}{2} - \frac{(m + 1)^2}{2}\ln(m + 1) - \frac{(m - 1)^2}{2}\ln(m - 1) \quad (2.21)$$

Which is basically obtained from the difference of the mutual inductance of loops of current sheet, subtracted from that of round wire loops.

2.2.2.5 Magnetic Non-uniformity

When the diameter and length of a coil are comparable, the magnetic non-uniformity effects become the most significant correction. To quantify the terms "long", and "short", we define aspect ratio parameter (γ)

$$\gamma = \frac{\ell_c}{d_c}. \tag{2.22}$$

The amount that short coil inductance deviates from long coil equation depends highly on the aspect ratio (see Figure 2-4). When $\gamma \gg 1$ the deviation is small and vice versa.

The correction to the linear infinitely long coil formula due to magnetic nonlinearity can be calculated by introducing a dimensionless coefficient κ_L, known as Nagaoka's coefficient [143], who introduced and developed a closed-form equation for calculating it across all ℓ_c/d_c spectrum

$$L_N = \mu \frac{N^2}{l_c} A_c \kappa_L = \mu N^2 \frac{d_c^3}{3l_c^2} \left[\frac{2y^2 - 1}{y^3} E(y^2) + \frac{1 - y^2}{y^3} K(y^2) - 1 \right]. \tag{2.23}$$

From this equation the non-uniformity factor (κ_L) can be written as

$$\kappa_L = \frac{4(d_c/\ell_c)}{3\pi} \left[\frac{2y^2 - 1}{y^3} E(y^2) + \frac{1 - y^2}{y^3} K(y^2) - 1 \right] \tag{2.24}$$

where $y = d_c/\sqrt{d_c^2 + l_c^2}$.

By combining the correction discussed above, the general formula for the inductance of a short coil with round wire winding can be written as

$$L = \mu \frac{N^2}{l_c} A_c \kappa_L - \mu \frac{d_c N}{2} (\kappa_s + \kappa_m) + L_i. \tag{2.25}$$

In this study we used the above formulation to compare our experimental results to

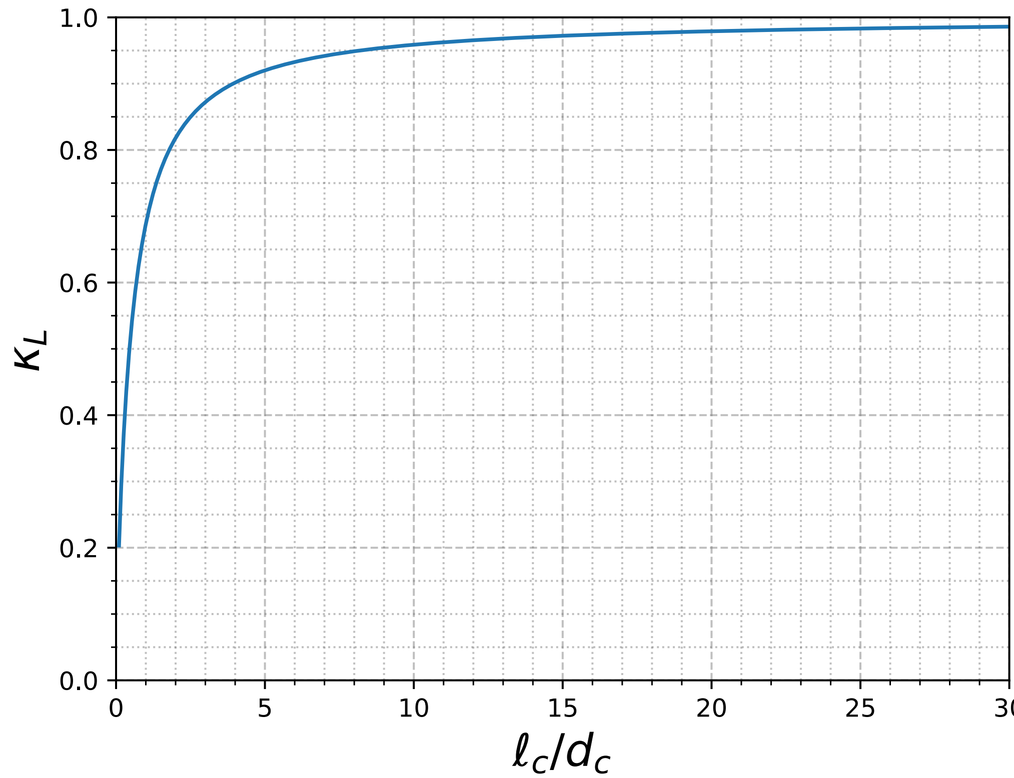

Figure 2-4: The dimensionless non-linearity correction κ_L as a function of length to diameter ratio. As the coil gets longer compared to its radius the correction gets smaller and less significant.

theory and COMSOL simulations.

2.2.3 Parasitic Inductance

Parasitic inductance (PI) is an inseparable part of any circuit. This undesirable inductance is caused by the flow of current in the circuit and is dependent on the length and diameter of the circuit's wires. In this study, the effect of PI is especially significant because its value is comparable to that of the coil in the circuit. Since PI is only dependent on the wires in the circuit, its value should remain unaffected when different coils with different numbers of turns are used. Using the fact that PI is independent of the coil as long as the same length of wire is used, we hypothesized that by measuring the inductance of multiple coils with the same wire type while keeping all other parts of the circuit constant, it is possible to determine the circuit's PI

$$L = L_{\mathrm{par}} + \frac{\beta N^2}{\ell_c} \tag{2.26}$$

where L_{par} is the parasitic inductance, and $\beta = \mu_0 \kappa_L A_c$ is a constant. It should be noted that to write equation (2.26) we have assumed that κ_m, κ_s, L_i are small compared to the first term in equation (2.25).

2.2.4 Magnetic Field and Flux Density

In our experimental setup the oscilloscope obtains the voltage across the inductor (V_B), and the voltage across the input source (V_A). By acquiring the entire time-series signals from the probes, the magnetic field and the magnetic flux density inside the coil can be calculated. To determine the current we calculated the electric potential across the resistor (V_R)

$$I(t) = \frac{V_R(t)}{R} = \frac{V_A(t) - V_B(t)}{R}. \tag{2.27}$$

By using the calculated current in the long coil formula, we can calculate the magnetic field

$$H(t) = \frac{N}{\ell_c} I(t). \tag{2.28}$$

If the coil is not an ideal, very long solenoid with a current sheet, the magnetic field inside it will not be uniform. However, if the coil's aspect ratio (γ_c) is large enough, the field will remain uniform within the coil, with the exception of its ends. The value

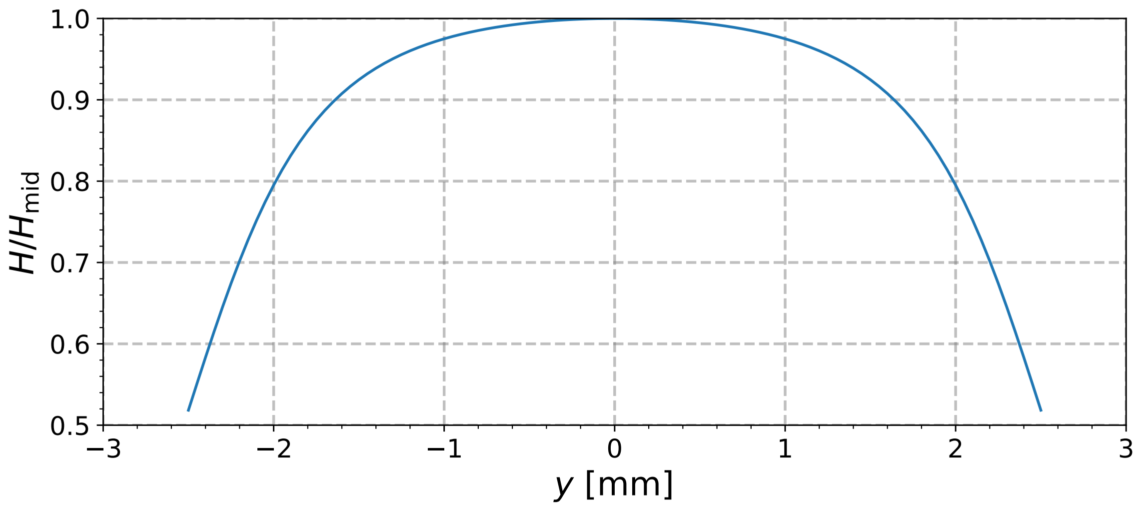

Figure 2-5: The value of the field amplitude inside a solenoid compared to its value at the center for a 16-turn solenoid of diameter 1.6 mm and length 5 mm when a 1 A current is running through the wires. Using the formula for field amplitude on the axis inside a short coil the average field inside the solenoid is about 90% of the field at the center. Only near the edges the field is significantly different.

of the field on the axis of a core-less short solenoid is obtained from

$$H = \frac{NI}{2\ell_c}\left(\sin(\theta_2) - \sin(\theta_1)\right) \tag{2.29}$$

where $\sin(\theta) = y/\sqrt{y^2 + r_c^2}$, y is the distance from the desired point to the end of the coil, and r_c is the radius of the coil. According to the equation (2.29), the magnetic field along the central axis of the coil, employed in the current experiment, changes as illustrated in Figure 2-5. Notably, the average field value across the axis is determined to be 90% of the field at the center.

The magnetic flux inside the coil, from the measured parameters can be obtained by measuring the electric potential across only the coil

$$V_c(t) = V_B(t) - V_{\text{par}}(t) - V_{r_w}(t,T) \tag{2.30}$$

where $V_{\text{par}}(t) = -L_{\text{par}}\frac{\mathrm{d}I(t)}{\mathrm{d}t}$, is the electric potential due to parasitic inductance, and $V_{r_w}(t,T) = r_w(T)I(t)$ is the electric potential due to wire resistance at temperature T in the circuit. Using the Lenz's law, we can write

$$V_c(t) = -N\frac{\mathrm{d}\Phi}{\mathrm{d}t} = -\frac{\mathrm{d}B(t)}{\mathrm{d}t}A_cN \tag{2.31}$$

therefore

$$B(t) - B(0) = -\frac{1}{NA_c}\int_0^t V_c(t')\mathrm{d}t'. \tag{2.32}$$

$B(0)$ (the flux density at time $t = 0$), is the offset necessary to ensure that the highest flux density occurs when the magnetic field strength is at its maximum (H_{max}). From $H(t)$, $B(t)$, the B-H curve can be generated.

2.2.5 Magnetic Permeability

A material's magnetic permeability determines its response to magnetic field. For diamagnetic and paramagnetic materials, the magnetic permeability is constant and independent of the applied magnetic field. However, for ferro- and ferri-magnetic materials with permanent magnetic properties, the magnetic permeability has a nonlinear relationship with the applied magnetic field. In the presence of an alternating magnetic field, permeability is represented by a complex number ($\mu_r = \mu' - \mathrm{j}\mu''$), where the real component relates to the interaction with the magnetic field and the imaginary component relates to the magnetic losses which will be discussed in more detail later. Another property of the ferro- and ferri-magnetic materials is the temperature dependence of their magnetic permeability. There is a critical temperature, namely the Curie temperature (T_c) at which these materials lose their magnetic properties and become paramagnetic. Therefore, conveniently, we use temperature (T) as an argument when we are discussing magnetic permeability.

Under the influence of a magnetic field, the magnetic domains within the ferrite reorient so that they align with the external magnetic field (H), thereby generate a magnetization field (M) and magnetic poles on the extremities of the sample. The magnetization field enhances the magnetic flux, but the poles at the ends generate a demagnetization field (H_d) in the opposite direction

$$B(t, T) = \mu_0(H(t) + M(t, T) - H_d(t, T)). \tag{2.33}$$

When the object is short and consequently its magnetic poles are closer together, the demagnetization field is stronger. For topologically infinite objects such as toroid demagnetization field does not exist ($H_d = 0$). Since some of the applied field inside the sample is cancelled by the pole field, the permeability obtained from the B-H curve indicates an effective relative permeability ($\mu' = B/\mu_0 H$) which is different from the intrinsic permeability of the material ($\mu'_i = B/(\mu_0 H - \mu_0 H_d)$).

The demagnetization field inside the cylinder placed in an external field in z direction is approximated by $H_d = N_z M$ where N_z is the demagnetization factor along the z direction of an ellipsoid with the same aspect ratio as the cylinder [144–147]. The demagnetization factor in all directions for an ellipsoid is analytically known based on the orientation of the ellipsoid with respect to the direction of the magnetic field. For an ellipsoid we have $N_x + N_y + N_z = 1$, which means that in the case of complete symmetry (a sphere) the demagnetization in all directions is equal to 1/3. The demagnetization factor for a cylinder can be approximated by using a special case of the ellipsoid formula where one of the dimensions is longer and the other two are equal. In the case of a cylinder of length ℓ, and diameter d, where $\ell > d$, with the field and long axis in parallel along the z direction the demagnetization factor is [145]

$$N_z = \frac{1-\psi^2}{\psi^3}\left(\frac{1}{2}\ln\left(\frac{1+\psi}{1-\psi}\right) - \psi\right) \tag{2.34}$$

where $\psi = \sqrt{1-\left(\frac{d}{\ell}\right)^2}$.

If the amplitude of the external magnetic field increases, more magnetic domains align, and consequently, M and H_d values increase. At some point during the magnetic field amplitude elevation, all the domains will be aligned with the field, at which point the material will be saturated ($M = M_s$) and the magnetic flux density will no longer increase in response to an increase in the external magnetic field. By looking at the definition of permeability [144]

$$\mu'(T) = 1 + (1 - N_z)\frac{M(T)}{H} \tag{2.35}$$

one can understand that magnetic saturation and demagnetization effect both put a cap on the value of magnetic permeability. At extremely high magnetic field amplitudes, relative permeability reaches the asymptotic value of 1.

Due to the nonlinear relationship between magnetic flux (B) and magnetic field (H) in ferrite materials, the applied sinusoidal magnetic field waveform results in a distorted magnetic flux signal. The amount of distortion depends on the amplitude of the magnetic field and the area of the hysteresis loop, and it can be expressed in terms of the odd harmonics of magnetic field when there is symmetry around the origin [144].

2.2.5.1 Low Field Amplitude

At very low field amplitudes, distortions are relatively small, and the waveform can still be very well approximated by a sine wave, while the magnetic permeability

(μ) stays nearly constant. In such a case, the relative permeability ($\mu_r = \mu/\mu_0$) can be calculated by using coil inductance equations (2.6) and (2.7) [144]

$$\text{Real}(\mu_r) = \mu'(T) = \frac{L'(T)}{L_{c_{\text{air}}}} = \frac{L(T) - L_{\text{par}}}{L_0 - L_{\text{par}}}. \tag{2.36}$$

The reason this method is only used for low amplitude application is that in writing equation (2.3), V_A, and V_B are assumed to be sinusoidal. Note that the parasitic inductance is subtracted from the calculated inductance, as parasitic inductance resembles a second inductor connected in series with the coil (Figure 2-2).

The alternating magnetic field inside the coil can cause energy loss in the core in a variety of ways. Hysteresis loss, which occurs when some domains retain their orientation and do not release their energy when the magnetic field is turned off. Eddy current loss results from the core's resistance to the induced electrical currents. Residual losses, refer to any residual process that may cause energy loss. The energy loss of the core causes its permeability to have a complex value when placed in an alternating magnetic field, and it can be correlated with its characteristic resistance.

At low field amplitudes, equations (2.6), and (2.7) can be used to calculate the characteristic resistance of the core

$$R_L(T) = R_c(T) - r_w(T) \tag{2.37}$$

where the wire resistance r_w, which appears in the circuit as a series resistance to the inductor, is subtracted from the coil's total resistance R_c (Figure 2-2).

Once the characteristic resistance is calculated the imaginary component of the permeability follows as [144]

$$\text{Im}(\mu_r) = \mu''(T) = \frac{R_L(T)}{\omega L_{c_{\text{air}}}}. \tag{2.38}$$

2.2.5.2 High Field Amplitude

When there is a significant distortion in the waveforms (Figure 2-6), μ_r can be calculated by using the extrinsic B-H curve of the core as opposed to the solutions from equations (2.6), and (2.7) that rely on sinusoidal output waveforms. Since hysteresis area of the B-H curve is nonzero for ferrite, $B(H)$ is not single-valued therefore, there is not a well-defined approach to calculate the real component of μ_r. However, in an alternating magnetization it is usually relevant only to consider the peak amplitude of B, and H, i.e. the tips of the loop, usually considered as amplitude permeability [144]

$$\mu'(T) = \frac{B(H_0, T)}{\mu_0 H_0}. \tag{2.39}$$

The energy loss during each cycle in a unit volume of the material is equal to the loop area

$$w_h = \oint B(T, H)\mathrm{d}H. \tag{2.40}$$

Consequently, the characteristic resistance of the coil can be found by [144]

$$R_L(T) = \frac{A_c \ell_c \omega w_h}{I_{\mathrm{rms}}^2}. \tag{2.41}$$

After finding the characteristic resistance, the imaginary component of the permeability can be obtained from equation (2.38). It is important to note that if the wire resistance (r_w) is not subtracted properly from the potential (equation (2.30)), the loss obtained from the B-H curve will not be purely through the core loss and the calculated μ'' will not be accurate.

Note that the results obtained from the B-H curve is applicable in both low and high magnetic field amplitudes, and for the case of low amplitudes it should yield the same results as Section 2.2.5.1. The permeability obtained from both methods, is the apparent permeability of the sample diminished by demagnetization and magnetic saturation. The relation between intrinsic relative permeability, and the apparent permeability can be found by

$$\mu' = \frac{\mu_i'}{1 + N_z(\mu_i' - 1)}. \tag{2.42}$$

2.2.6 Theoretical Justification of B-H Curve Results

In the absence of a core, we expect B, and H to be linearly related and the area of the B-H curve to be zero ($R_L = 0$), or in other words as we expect $B = \mu_0 H$. Starting from a general ideal case where $r_w = 0$, and $L_{\text{par}} = 0$, we can analytically solve the field, and flux equations. Using the voltages at points A, and B (Figure 2-2)

$$\mathbf{V}_A = V_A \sin(\omega t + \phi_A) \tag{2.43}$$

$$\mathbf{V}_B = V_B \sin(\omega t + \phi_B) \tag{2.44}$$

where V_A, and V_B are positive real numbers, and replacing them in equations (2.28), and (2.32) we find

$$H(t) = \frac{N}{\ell_c} I(t) = \frac{N}{\ell_c R} (V_A \sin(\omega t + \phi_A) - V_B \sin(\omega t + \phi_B)) \tag{2.45}$$

by expanding the terms in parenthesis we obtain

$$\begin{aligned} H(t) &= \frac{N}{\ell_c R} ((V_A \cos(\phi_A) - V_B \cos(\phi_B)) \sin(\omega t) \\ &+ (V_A \sin(\phi_A) - V_B \sin(\phi_B)) \cos(\omega t)) \\ &= \alpha (H_s \sin(\omega t) + H_c \cos(\omega t)), \end{aligned} \tag{2.46}$$

where $\alpha = N/(\ell_c R)$. The flux density can be calculated as

$$\begin{aligned}
B(t) - B(0) &= \frac{1}{NA_c}\int_0^t (V_B(t'))\,\mathrm{d}t' \\
\Rightarrow B(t) &= \frac{1}{NA_c\omega}V_B \sin(\phi_B)\sin(\omega t) - \frac{1}{NA_c\omega}V_B\cos(\phi_B)\cos(\omega t) \\
&= \beta\left(B_s \sin(\omega t) + B_c\cos(\omega t)\right), \qquad (2.47)
\end{aligned}$$

where $\beta = 1/(NA_c\omega)$. By solving equations (2.46), and (2.47) for $\sin(\omega t)$, and $\cos(\omega t)$ one finds

$$\sin(\omega t) = \frac{\beta B_c H(t) - \mu_0\alpha H_c B(t)}{\alpha\beta\left(H_s B_c - B_s H_c\right)} \qquad (2.48)$$

$$\cos(\omega t) = \frac{\mu_0\alpha H_s B(t) - \beta B_s H(t)}{\alpha\beta\left(H_s B_c - B_s H_c\right)} \qquad (2.49)$$

where to obtain the results we have divided equation (2.47) by μ_0 so both of the equations have the same dimensions. By using the identity $\sin^2(\omega t) + \cos^2(\omega t) = 1$ one gets

$$\begin{aligned}
\left(\frac{1}{\alpha\beta\chi}\right)^2 \Big[\mu_0^2\alpha^2\left(H_s^2 + H_c^2\right)B^2(t) + \beta^2\left(B_s^2 + B_c^2\right)H^2(t) \\
- 2\mu_0\alpha\beta\left(H_s B_s + H_c B_c\right)H(t)B(t)\Big] = 1 \qquad (2.50)
\end{aligned}$$

where

$$\chi = H_s B_c - B_s H_c. \qquad (2.51)$$

This equation has the same form as general formula for an ellipse

$$\underbrace{\left(\frac{\cos^2\theta}{a^2} + \frac{\sin^2\theta}{b^2}\right)}_{\eta} x^2 + \underbrace{2\cos\theta\sin\theta\left(\frac{1}{a^2} - \frac{1}{b^2}\right)}_{\zeta} xy + \underbrace{\left(\frac{\sin^2\theta}{a^2} + \frac{\cos^2\theta}{b^2}\right)}_{\xi} y^2 = 1 \quad (2.52)$$

where θ is the angle of the rotation, and a, b are the semi minor, and semi major axis. For equation (2.50) to truly represent an ellipse, the following conditions should be satisfied

$$c1 : \eta > 0$$
$$c2 : \xi > 0$$
$$c3 : \zeta^2 - 4\eta\xi < 0$$

Conditions $c1$, and $c2$ are both clearly satisfied as $\mu_0^2(H_s^2 + H_c^2)/\beta^2\chi^2 > 0$, and $(B_s^2 + B_c^2)/\alpha^2\chi^2 > 0$. The last condition also can be easily verified by

$$4\frac{\mu_0^2(H_sB_s + H_cB_c)^2}{\alpha^2\beta^2\chi^4} - 4\frac{\mu_0^2(H_s^2 + H_c^2)(B_s^2 + B_c^2)}{\alpha^2\beta^2\chi^4} = -4\frac{\mu_0^2(H_cB_s - H_sB_c)^2}{\alpha^2\beta^2\chi^4}$$
$$= -\frac{4\mu_0^2}{\alpha^2\beta^2\chi^2} < 0.$$

Now that the conditions hold, one can solve for the parameters of the ellipse, i.e. a, b, and θ by solving three equations for three unknowns

$$\frac{\mu_0^2(H_s^2 + H_c^2)}{\beta^2\chi^2} = \left(\frac{\cos^2\theta}{a^2} + \frac{\sin^2\theta}{b^2}\right) \tag{2.53}$$
$$\frac{B_s^2 + B_c^2}{\alpha^2\chi^2} = \left(\frac{\sin^2\theta}{a^2} + \frac{\cos^2\theta}{b^2}\right) \tag{2.54}$$
$$\frac{\mu_0(H_sB_s + H_cB_c)}{\alpha\beta\chi^2} = -\cos\theta\sin\theta\left(\frac{1}{a^2} - \frac{1}{b^2}\right). \tag{2.55}$$

After some manipulations we obtain

$$\theta = -\frac{1}{2}\arctan\left(\frac{2\alpha\beta\mu_0(H_sB_s + H_cB_c)}{\alpha^2\mu_0^2(H_s^2 + H_c^2) - \beta^2(B_s^2 + B_c^2)}\right) \tag{2.56}$$
$$\frac{1}{a^2} = \frac{\frac{1}{2}\left(\alpha^2\mu_0^2(H_s^2 + H_c^2) + \beta^2(B_s^2 + B_c^2)\right)\sin 2\theta - \alpha\beta\mu_0(H_sB_s + H_cB_c)}{\alpha^2\beta^2\chi^2\sin 2\theta} \tag{2.57}$$
$$\frac{1}{b^2} = \frac{\frac{1}{2}\left(\alpha^2\mu_0^2(H_s^2 + H_c^2) + \beta^2(B_s^2 + B_c^2)\right)\sin 2\theta + \alpha\beta\mu_0(H_sB_s + H_cB_c)}{\alpha^2\beta^2\chi^2\sin 2\theta} \tag{2.58}$$

where the following identities hold

$$H_s^2 + H_c^2 = V_A^2 + V_B^2 - 2V_AV_B\cos\delta\phi \tag{2.59}$$

$$B_s^2 + B_c^2 = V_B^2 \tag{2.60}$$

$$H_sB_s + H_cB_c = -V_AV_B\sin\delta\phi. \tag{2.61}$$

Using the core-less RL circuit equations when $R_L = 0$ and plugging into the above equations they reduce to

$$H_s^2 + H_c^2 = V_A^2\left(1 - \frac{\omega^2L^2}{R^2+\omega^2L^2}\right) = V_A^2\frac{R^2}{R^2+\omega^2L^2} \tag{2.62}$$

$$B_s^2 + B_c^2 = V_A^2\frac{\omega^2L^2}{R^2+\omega^2L^2} \tag{2.63}$$

$$H_sB_s + H_cB_c = -V_A^2\frac{R\omega L}{R^2+\omega^2L^2}. \tag{2.64}$$

If we plug these values in equations (2.56) usnig $\beta/\alpha = \kappa_L\mu_0R/\omega L$ we find that

$$\theta = \frac{1}{2}\arctan\left(\frac{2\kappa_L}{1-\kappa_L^2}\right). \tag{2.65}$$

In the case when the non-uniformity is not very strong and $\kappa_L \approx 1$, we have

$$\theta \approx \frac{\pi}{4} - \frac{1}{2}(1-\kappa_L) \Rightarrow \tan\theta \approx \kappa_L \tag{2.66}$$

and finally the equation (2.56) through (2.58)

$$\frac{1}{a^2} = \frac{2\mu_0^2V_A^2R^2}{\beta^2\chi^2} = \infty \to a = 0 \tag{2.67}$$

$$\frac{1}{b^2} = \frac{0}{\beta^2\chi^2} = \infty \to b = 0 \tag{2.68}$$

where in an ideal case with no nonlinearity $\kappa_L = 1$ and $B = \mu_0 H$ as one expects. With either $a = 0$ or $b = 0$ the ellipse equation results in a line equation with the formula $x = \tan\theta\ y$.

These calculations show that indeed the formulas from B-H curve calculations and the RL circuit equations yield equivalent results in an ideal case and B-H curve will have no area.

2.3 Intrinsic Permeability Measurements

Due to its infinite topology a toroid-shaped sample does not experience the demagnetization effects. This means that investigating the magnetic properties of a toroid ferrite sample with the same chemical structure and concentration will provide us with the intrinsic permeability. Intrinsic permeability is the intrinsic response of the ferrite material to the magnetic field without demagnetization field interfering. Its value is tipically much larger than the permeability of short cylindrical samples.

To find the permeability of the sample, it is wound by wire and placed in the same RL circuit. For high field amplitude regime we can use Equation (2.39) to find the permeability.

2.4 Heat Power Generated by HT-only and TB Seeds

The ferrite can independently generate power via hysteresis loss, eddy current loss, and other residual losses. However, the overall loss caused by the ferrite is insufficient to adequately raise the tissue temperature for effective hyperthermia, so a biocompatible metal shell with the appropriate electrical properties is added to function as the primary heat source (Figure 2-1). The ferrite core enhances the magnetic field inside the shell and increases the resulting eddy current. Therefore, the total power generated by the seed is equal to the sum of the power generated by the shell and ferrite core. In the sections that follow, we will look into the specifics of how the shell and its core generate power.

2.4.1 Heat Production by Cylindrical Implants

The hysteresis losses for a soft ferrite are very small, whereas the eddy current loss depends on the field strength and frequency. By measuring the area of the B-H curve, the total power produced by the core, including all types of losses, can be determined.

Theoretically the eddy current volumetric power loss can be calculated by

$$P_e = \frac{|J_{\text{ext}}|^2}{2\sigma_c} \tag{2.69}$$

where J_{ext} is the external current density and is calculated by solving the following equation

$$J_{\text{ext}} = \left(\mathrm{j}\omega\sigma_c - \omega^2\epsilon_c\right)\vec{A} + \vec{\nabla} \times \left(\frac{1}{\mu_c}\vec{\nabla} \times \vec{A}\right) \tag{2.70}$$

where μ_c, and ϵ_c are the core magnetic permeability and electric permittivity respectively, and $\vec{A}$ is the magnetic vector potential. Davies and Simpson [148] solved Equation (2.70) analytically and calculated the power per unit length for a cylinder

$$P_a(x) = \pi x \frac{H_0^2}{\sigma} \frac{ber(x)ber'(x) + bei(x)bei'(x)}{ber^2(x) + bei^2(x)} \tag{2.71}$$

where $x = r_c\sqrt{\omega\mu'\mu_0\sigma_c}$ is the inductance number, $ber(x)$ and $bei(x)$ are Kelvin's form of the first order Bessel function J_0, r_c is the radius of the core, ω is the angular frequency of the magnetic field, μ' is the relative magnetic permeability, and σ is the electrical conductivity of the ferrite core. When P_a is linearized in terms of inductance number x, total power can be approximated as

$$P(T) = \ell_c P_a(x) \approx r_c^2 \ell_c \mu'(T, H_0, \gamma) \mu_0 \omega H_0^2 \tag{2.72}$$

where $\gamma = \ell_c/d_c$ is the geometrical aspect ratio, and ℓ_c is the core length. Note that the temperature dependence is contained in relative permeability.

Equation (2.71) is derived under the assumption of linear relationship between the the magnetization and magnetic field strength and does not include the dependence of the permeability on the field strength. Additionally, the core is assumed to be isotropic, and the electrical conductivity, and dielectric constant to be real and independent of the field strength. Moreover, to derive it, demagnetization effect is neglected by assuming long seeds.

Since the demagnetization effects significantly reduce the value of the permeability, equation (2.71) may overestimate the power generated by the core. On the other hand the non-linear relationship between the field and permeability results in a higher power loss and the combination of the two factors might make this formula relatively acceptable [149]. Due to uncertainties mentioned above, instead of using the theoretical approach to find the power loss by the core, using the area inside the B-H curve is more accurate.

The seed's shell produces power solely through resistive heating. As eddy current circulates inside the shell the resistivity of the shell causes some power loss. The ferrite core enhances the magnetic field, which in turn amplifies the eddy current inside the shell. On the other hand the field generated by eddy current reduces the overall field strength. The approximate resistive power generation by the seed shell can be found by [150]

$$P(T) = \frac{\left(\mu' \mu_0 \omega A_c\right)^2 \sigma_s t_s H_0^2 \ell_c}{2\pi r_s} \left[\frac{1}{1 + \left(\frac{\mu' \mu_0 \omega \sigma_s t_s A_c}{2\pi r_s} \right)^2} \right] = \frac{\left(\chi_L(T) \ell H_0\right)^2}{2R_s \left(1 + \frac{\chi_L^2(T)}{R_s^2}\right)} \qquad (2.73)$$

where the term in the bracket is the shielding effect by the eddy currents, $\chi_L(T) = \pi r_c^2 \mu'(T, H, \gamma)\mu_0 \omega / \ell_c$ is the core inductive reactance, and $R_s = (2\pi r_s)/(\sigma_s t_s \ell_c)$ is the shell's resistance, r_s, t_s, σ_s are radius, thickness, and electrical conductivity of the shell respectively. Equation (2.73) is calculated assuming magnetic field, and magnetic flux density are linearly related to each other. However, in the case of nonlinear relation an effective permeability such as the one calculated in equation (2.39) can be used [150]. The above formula implies that the optimal combination of size, permeability, frequency, and field magnitude can generate the required thermal power. Some of these factors, such as the size of the seeds or the frequency and strength of the magnetic field, are dictated by clinical specifications, but the remainder can be adjusted.

2.4.2 Optimizing Power Generation

As previously mentioned, the power generated by the ferrite core itself is a negligible portion of the total power generated by the seed; therefore, for the purposes of optimization, we will focus on optimizing the seed structure to extract the maximum power from the shell for a given core permeability. There are two methods to determine the optimal combination of the parameters to extract maximum power from the sheath. The first method is to fix the outer diameter ($d_s = 2r_s$) and simultaneously optimize for the best core radius (r_c), and shell thickness (t_s). Finding the derivative is not simple because the core permeability due to demagnetization effects also depends on the core radius via aspect ratio ($\gamma = r_c/\ell_c$). The apparent permeability depends on the aspect ratio through demagnetization factor as shown in equation (2.34).

The value of the permeability is also dependent on the field strength H at the surface of the ferrite core attenuated by the tissue and the shell

$$H = H_0 \exp\left(\frac{-t_t}{\delta_t}\right) \exp\left(\frac{-t_s}{\delta_s}\right) \tag{2.74}$$

where t_t, δ_t are the tissue average thickness, and tissue skin depth respectively, and δ_s is the shell skin depth. The skin effect in the shell is a limiting factor on how much field can penetrate to the ferrite core, and this directly affects the permeability of the core. Higher frequencies result in more attenuation and therefore, this is another reason to choose the lowest possible frequency when treating with TB, and HT-only seeds.

Taking the derivative with respect to the shell thickness we get

$$\frac{\partial P}{\partial t_s} = 0 \Rightarrow \frac{\ell_c^2 H_0^2}{2} \frac{\left(2\chi_L R_s \frac{\partial \chi_L}{\partial t_s} + \chi_L^2 \frac{\partial R_s}{\partial t_s}\right)(\chi_L^2 + R_s^2) - 2\left(\chi_L \frac{\partial \chi_L}{\partial t_s} + R_s \frac{\partial R_s}{\partial t_s}\right)\chi_L^2 R_s}{\left(\chi_L^2 + R_s^2\right)^2} = 0 \tag{2.75}$$

After substituting $\partial R_s / \partial t_s = -R_s / t_s$ in the above equation and some simplification one can write

$$2R_s^2 t_s \frac{\partial \chi_L}{\partial t_s} - \chi_L^3 + \chi_L R_s^2 = 0 \tag{2.76}$$

where

$$\frac{\partial \chi_L}{\partial t_s} = -\left(2\mu'(T,H,\gamma) + \frac{H}{\delta_s}\frac{\partial \mu'(T,H,\gamma)}{\partial H} r_c + 2\mu'^2(T,H,\gamma)\frac{\gamma^2}{\psi}\frac{\partial N_z}{\partial \psi}\right)\frac{\pi \mu_0 \omega}{\ell_c} r_c \tag{2.77}$$

By substituting the above equations and simplifying the common factors we get

$$\mu'^2 \mu_0^2 \sigma_s^2 \omega^2 r_c^5 t_s^2 + 8\left(2 + \frac{H}{\delta_s}\frac{\partial \ln \mu'}{\partial H} r_c + 2\mu'(T,H,\gamma)\frac{\gamma^2}{\psi}\frac{\partial N_z}{\partial \psi}\right) r_s^2 t_s - 4 r_s^2 r_c = 0 \tag{2.78}$$

where $r_c = \lambda - t_s$. For the case of HT-only seed $\lambda = r_s$, and for TB seed $\lambda = r_s - t_i$, where t_i is the thickness of the radioactive carbon-iodine layer. The equation above can only be solved by numerical solutions. If one neglects the attenuation of the field due to the shell thickness i.e. the limit where $\delta_s \to \infty$ the equation simplifies to

$$\mu'^2 \mu_0^2 \omega^2 \sigma_s^2 r_c^5 t_s^2 + 16 r_s^2 t_s - 4 r_s^2 r_c = 0. \tag{2.79}$$

Second method for optimization is to fix the core radius (therefore keeping the aspect ratio γ as constant) and allow shell radius change and find the optical thickness for highest power extraction. In this method we start with Equation (2.75) and then substitute $\partial R_s/\partial t_s = -\lambda R_s/t_s r_s$ where for HT-only seeds we have $\lambda = r_c$, and for TB seeds we have $\lambda = r_c + t_i$

$$-\frac{\lambda \chi_L^3}{t_s} + 2 r_s R_s^2 \frac{\partial \chi_L}{\partial t_s} + \frac{\lambda \chi_L R_s^2}{t_s} = 0 \tag{2.80}$$

and we can analytically find the optimal thickness by solving the following equations

$$\lambda \mu'^2 \mu_0^2 \sigma_s^2 \omega^2 r_c^4 t_s^2 - 8 \frac{H}{\delta_s} \frac{\partial \ln \mu'}{\partial H} r_s^3 t_s + 4 \lambda r_s^2 = 0 \tag{2.81}$$

where $r_s = r_c + \lambda$. In the limit at which $\delta_s \to \infty$ the equation simplifies to

$$R_s = \chi_L \Rightarrow \frac{\partial \chi_L}{\partial t_s} = 0 \Rightarrow t_s = \frac{2\lambda}{\mu' \mu_0 \omega \sigma_s r_c^2 - 2}. \tag{2.82}$$

Note that equations (2.78) and (2.81) optimize the thickness for a given frequency and sheath conductivity.

2.5 Heat Transfer

2.5.1 Heat Transfer Equation

The heat generated by the seeds can be transferred through conduction, radiation and convection based on the boundary conditions, and the medium. The heat transfer equation is written as

$$\rho C_p \frac{\partial T}{\partial t} + \vec{\nabla} \cdot \left(-k \vec{\nabla} T \right) = Q_{\text{ext}} \tag{2.83}$$

where ρ is the tissue density, C_p is the specific heat capacity at constant pressure, k is the thermal conductivity, and Q_{ext} is any external heat sink/source. Conductive heat transfer is represented by the second term on the left-hand side of Equation (2.83).

Radiative heat transfer can be added to the right-hand side of the Equation (2.83) as a heat sink. The amount of heat transferred through radiation can be found by using the surface to ambient radiation formula

$$Q_{\text{rad}} = \varepsilon_e \sigma_{\text{SB}} \left(T_s^4 - T_a^4 \right) \tag{2.84}$$

where ε_e is the emissivity of the surface, σ_{SB} is the Stefan-Boltzmann constant, T_s is the surface temperature, and T_a is the ambient temperature with the condition that $T_s > T_a$.

In the areas where convective heat transfer exists, such as fluids, an extra source for heat sink can be added to the Equation (2.83)

$$Q_{\text{conv}} = h \Delta T \tag{2.85}$$

where ΔT is the temperature difference between the surface and the fluid, and h is the heat transfer coefficient that depends on the geometry. For natural convection of air over a flat surface [151]

$$h \approx C \left(\xi \frac{\Delta T}{l} \right)^{n} \tag{2.86}$$

where l is the length/diameter of the surface, ξ is chosen as 1 $\mathrm{m\,K^{-1}}$ such that the quantity in the parenthesis is dimensionless, and C, and n are empirical constants.

2.5.2 Blood Perfusion Effects

In real prostate tissue, blood perfusion is the primary source of heat dissipation and the most significant obstacle to overcome to obtain uniform clinical-range temperature distribution in the target tissue. Blood flow is quantitatively measured by volumetric blood perfusion rate (ω_b), obtained by the product of the vascular perfusion rate by tissue density. The amount of heat dissipated by the blood flow depends linearly on the vascular perfusion rate [152]

$$Q_{\mathrm{per}} = \rho_b C_b \omega_b \left(T_b - T \right) \tag{2.87}$$

where ρ_b is the blood density, C_b is the blood heat capacity, T_b is the temperature of the flowing arterial blood, and T is the temperature at a certain point inside the tissue. Q_{per} should be added to the right-hand side of Equation (2.83) as heat sink when solving heat transfer equations in the tissue.

2.6 Thermal Expansion

As the seeds generate power and increase the surrounding temperature, both the shell and the core undergo thermal expansion. It is important to study the thermal expansion of the seed, to make sure that the seed remains integral in the desired temperature range, and no cracks appear on the seeds, as this can result in radioactive material leakage. In theory the volume expansion can be explained by

$$\frac{\Delta V}{V} = \alpha_V \Delta T \tag{2.88}$$

where V is the volume of the object and α_V is the coefficient of volume thermal expansion, and it is defined as

$$\alpha_V = \frac{1}{V}\frac{\mathrm{d}V}{\mathrm{d}T} \tag{2.89}$$

when the changes are small, volume thermal expansion coefficient is approximately 3 times larger than the linear thermal expansion coefficient ($\alpha_V \approx 3\alpha_L$).

The value of the thermal expansion coefficient depends on the material, therefore, the shell, and the core, each expand a different amount. The shell should be able to tolerate the amount of stress caused by the core strain. The difference in the ferrite length change $\Delta\ell_c$, and the shell length change $\Delta\ell_s$, will be the source of stress on the shell

$$\Delta\ell = \Delta\ell_c - \Delta\ell_s. \tag{2.90}$$

The pressure on the shell can be calculated by using the Young's modulus (Y)

$$Y = \frac{\frac{F}{A_c}}{\frac{\Delta\ell}{\ell_0}} \Rightarrow \frac{F}{A_c} = Y\frac{\Delta\ell}{\ell_0}. \tag{2.91}$$

By comparing the resulting pressure with the elastic limit of the shell material we can verify if the pressure can be tolerated by the shell.

2.7 Magnetic Interaction of Seeds

Using TB and HT-only seeds in a thermo-brachytherapy plan increases the number of seeds compared to conventional LDR brachytherapy plan. This raises the question of whether the presence of many seeds in the volume of the prostate and/or the presence of multiple seeds back-to-back within the same needle causes any deviations in the magnetic field and heat distribution in the prostate.

In conventional brachytherapy the needles are spaced about 1 cm away from each other [153]. Since the dipole fields generated by the seeds decays with the inverse cube of the distance [154] and the lateral separation of the needles are much bigger than the diameter of the seeds (∼1 mm), we expect the seeds in the neighboring needles to impose no magnetic effect on each other.

On the other hand, seeds that are located in the same needle can potentially act as a longer seed and result in higher relative permeability (lower demagnetization) and higher power production compared to the conservative assumption of disjoint seeds. The difference in power production depends on the combination of the seeds, which is impossible to know until they are implanted by the physician. To find the effect of seeds abutting each other on the same needle, we start with equation (2.73). With the thickness constant, a longer seed ($\tilde{\ell} = n\ell$), will only have a different permeability

$$P_{n\ell} = \frac{\left(\chi_{n\ell}\tilde{\ell}H_0\right)^2}{2R_{s,n\ell}\left(1+\frac{\chi_{n\ell}^2}{R_{s,n\ell}^2}\right)} = n\left(\frac{\mu'_{n\ell}}{\mu'_\ell}\right)^2 \frac{(\chi_\ell \ell H_0)^2}{2R_{s,\ell}\left(1+\left(\frac{\mu'_{n\ell}}{\mu'_\ell}\right)^2\frac{\chi_\ell^2}{R_{s,\ell}^2}\right)}. \tag{2.92}$$

To see the difference in the power production when n seeds of length ℓ act as a long seed of length $n\ell$ we divide the long seed power by nP_ℓ

$$\frac{P_{n\ell}}{P_\ell} = \left(\frac{\mu'_{n\ell}}{\mu'_\ell}\right)^2 \frac{\left(1+\frac{\chi_\ell^2}{R_{s,\ell}^2}\right)}{1+\left(\frac{\mu'_{n\ell}}{\mu'_\ell}\right)^2\frac{\chi_\ell^2}{R_{s,\ell}^2}}. \tag{2.93}$$

In the limiting case when $\mu'_{n\ell} \gg \mu'_\ell$ this ratio simplifies to

$$\lim_{\mu'_{n\ell}/\mu \gg 1} \frac{P_{n\ell}}{P_\ell} \approx \frac{1+\frac{\chi_\ell^2}{R_{s,\ell}^2}}{\frac{\chi_\ell^2}{R_{s,\ell}^2}}. \tag{2.94}$$

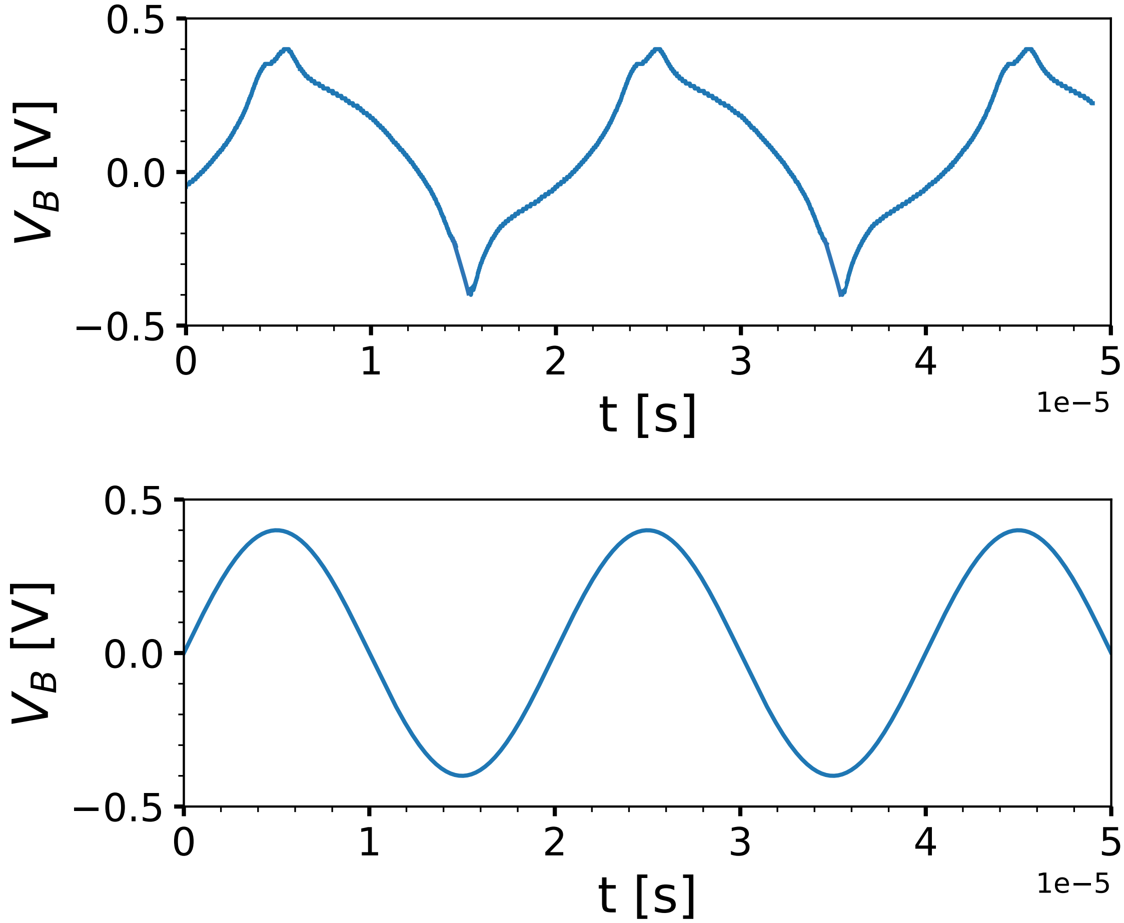

Figure 2-6: Top: An example of a waveform that has been distorted by the presence of the ferrite core in the coil at temperature 55 °C, frequency of 50 kHz, and magnetic field strength 3.5 $\mathrm{kA\,m^{-1}}$. Bottom: An undistorted sine wave with the same frequency and amplitude.

Chapter 3

Materials and Methods

3.1 Experimental Setup

Cylindrical ferrite core samples with the desired Curie temperature (55 °C) and dimensions (0.94 mm in diameter, 5.0 mm in length) were manufactured by National Magnetics Group Inc., Bethlehem, PA. In order to study the magnetic permeability of the sample, an enamel coated copper wire with a diameter of 0.254 mm was helically wrapped to accommodate the ferrite core dimensions. As depicted in Figure 2, the tightly wound solenoid served as an inductor in a first-order series connected RL circuit. A function generator (Wavetek Model 166, San Diego, CA) was used to generate a sinusoidal voltage with frequencies ranging from 50 kHz to 200 kHz. This signal was routed to a custom-built amplifier stage based on an operational amplifier (TI OPA548, Dallas, TX), which could supply the required currents to yield relatively high magnetic field strengths (8 $\mathrm{kA\,m^{-1}}$) within the solenoid. An oscilloscope (Tektronix TDS 2022B, Beaverton, OR) was used to monitor voltages at each node of the resistor R in the RL circuit. The resistor R was composed of ten (10.0 ± 1%) Ω, 100 ppm/°C, 0.25 W metal film resistors (Vishay RN60 series, Malvern, PA) that were connected in parallel to provide an effective resistance of (1.0 ± 1%) Ω, 10 ppm/°C, 2.5 W. The oscilloscope input impedance was a 20 pF capacitance in parallel with a 1 MΩ resistance to ground. However, simulations of the circuit with the oscilloscope's input impedance in place had no significant effect on the results and were thus omitted from the circuit model and analysis.

The temperature dependence of ferrite core permeability was investigated using a vertically mounted enclosure consisting of a cylindrical polyvinyl chloride (PVC) pipe (10 cm in diameter and 14 cm in length) with an incandescent lamp heat source at the top and the solenoid at the base (Figure 3-1). A thermocouple (Omega CN7500, Norwalk, CT) was used to measure temperature near the solenoid, and a source meter (Keithley 2636A, Solon, OH) was used to programmatically increase the power to the lamp. The solenoid and thermocouple were located at the base of the enclosure, while the rest of the circuitry was located outside. A computer running a Python script written in-house handled all process control and data collection for the experiment. The temperature of the solenoid was gradually raised, and once the temperature had stabilized, two time-based voltage waveforms of interest were measured and acquired from the oscilloscope. A typical set of measurements for a temperature range of 20 °C to 70 °C took about four hours to complete.

3.2 Validation of Calculated Coil Inductance with COMSOL

By developing a finite element program in COMSOL Multiphysics, the results obtained from Equation (2.25) were confirmed. The geometry of the coil was estimated with an array of symmetrical loops of wire with loop diameter 1.33 mm and wire diameter 0.25 mm. Through electrical circuit physics the coil was connected to a circuit with a resistor, creating an RL circuit. The Electrical Circuit physics node then was coupled to a Magnetic Field physics node for modeling the magnetic field inside and outside of the coil. An infinite boundary domain was used at distance 5

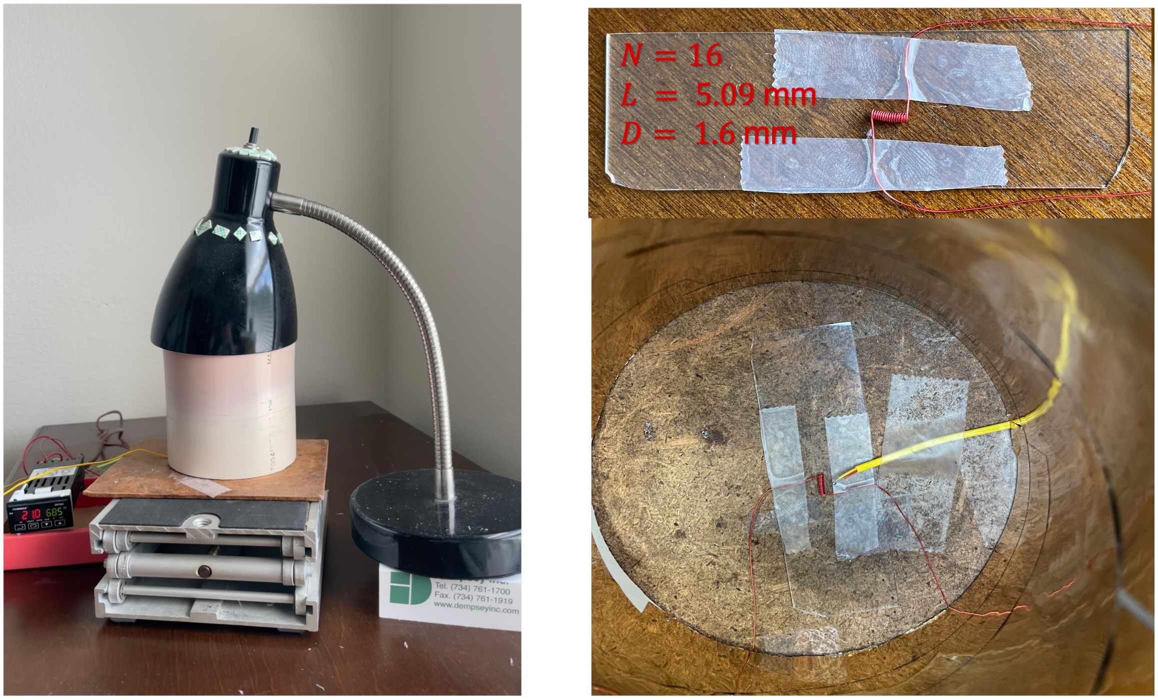

Figure 3-1: The setup used for insulating, increasing, and measuring the temperature.

cm away from the axis of symmetry. The differential equations were solved in the frequency domain, with an absolute tolerance of 0.001, and 25 maximum iterations. The geometry was tiled with an adaptive mesh with an average density of 2×10^9 elements/m^2 in the coil region and 5×10^7 elements/m^2 in the surroundings.

3.3 Validation of Power versus Temperature Formula by Using B-H Curve and Joule Heating

As previously described we used the amplitude permeability in the strong field regime (Equation (2.39)). The permeability is required to calculate the power generated by the seed (Equation (2.73)). To verify the accuracy of the approximated power we

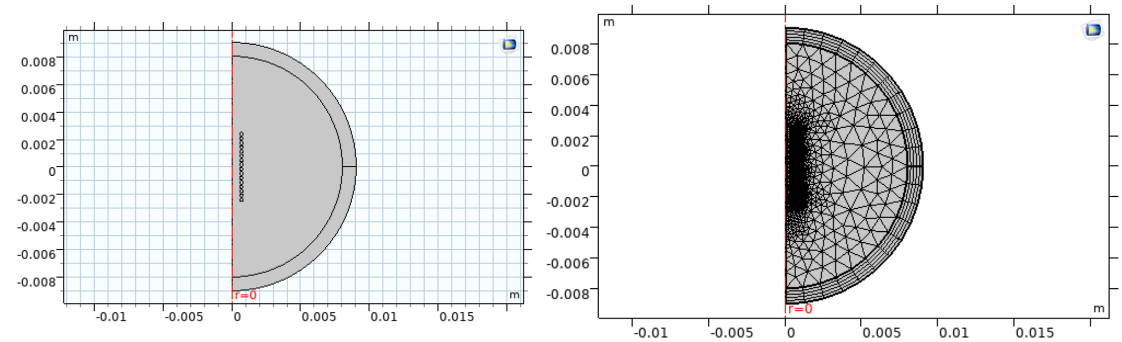

Figure 3-2: Left: The geometry of an empty coil defined in COMSOL Multiphysics for validation of theoretical calculations. Right: The mesh Used for FEA analysis.

developed a two-dimensional axisymmetric model to calculate the power generated by a single seed in the presence of an alternating magnetic field. The B-H curve obtained from measurement was used as the magnetic properties of the ferrite core.

The model's geometry included a ferrite core surrounded by a shell with the optimal thickness. The seed was placed at the center of a large coil carrying alternating current and generating magnetic field around the seed.

A combination of "Magnetic Fields", and "Bioheat Transfer" physics were used to solve this problem in a frequency-transient study. The "Magnetic Field" physics calculates the magnetic field propagating in the medium and the eddy currents generated on the shell, and the "Bioheat Transfer" translates the heat generated from the eddy currents to a heat source in the heat transfer equations.

The absolute tolerance for numerical calculations is set to 10^{-6}, and the maximum number of iterations were set to be 25. The mesh used for this geometry was adaptive with special considerations on the boundaries of the shell due to very small dimensions and the importance of capturing the skin effect and eddy current generated on it. The mesh has the average density of 2.6×10^9 elements/m^2 in the seed region of geometry, 1.2×10^7 elemenst/m^2 in the coil region, and 6×10^5 elements/m^2 over the rest of the geometry (Figure 3-3).

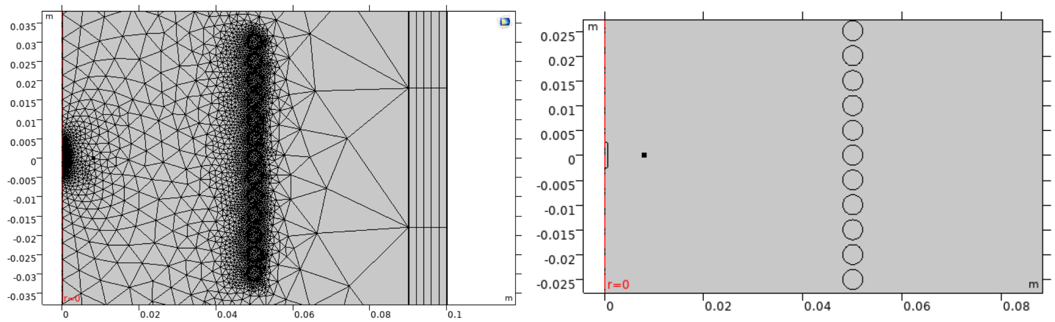

Figure 3-3: The geometry and mesh structure used for calculating the power generated by the seed using B-H curve.

3.4 Experimental Measurement of Temperature Distribution in Agar Phantom

For a practical test of the power generated by the seed, they were placed in a 0.6%w/v agar phantom made by mixing 0.9 g of agarose powder (HiMedia, Plot No. C40, Road No. 21Y, MIDC, Wagle Industrial Estate, Thane - 400604, Maharashtra, India) with 150 mL of distilled water [155]. The phantom was created in the shape of a cylinder with a diameter of 77.20 mm, and a length of 21.47 mm. Due to the low concentration of the agar solution, the specific heat at constant pressure and the density were similar to those of water, with values of $C_p = 4200\ \mathrm{J\,kg^{-1}\,K^{-1}}$, and $\rho = 1000\ \mathrm{kg/m^3}$ respectively. The thermal conductivity of the agar phantom was $k = 0.6\ \mathrm{W\,m^{-1}\,K^{-1}}$ [155]. For this experiment, 16 long seeds ($\ell = 1$ cm) were initially coated by vapor deposition to create a very thin layer of gold on the seeds to allow gold material to stick on the seeds by dipping method, and then they were coated with 14-carat gold by Jeweler's shop. The initial weight of the 16 seeds was 547 mg and the final weight was 548 mg resulting in a coating with an average thickness of 0.1 µm. The seeds were placed inside the phantom in the shape of a 4×4 array with 1 cm separation and an axis perpendicular to the surface of the phantom. A 10 kW industrial induction heater (Across International Model IHG10) with a four-loop

Figure 3-4: The agar phantom with the implanted seed array.

coil of 15 cm diameter was used to generate the alternating magnetic field with a frequency of 122 kHz (Figure 3-4).

The temperature distribution on the surface was measured by a microbolometer-based infrared camera (Fluke Ti100 thermal imager).

The phantom was placed at the center of the coil until it reached thermal equilibrium with its surroundings. The field produced by the four-loop coil attached to the induction heater with different current settings can be obtained from

$$H = 0.4848 I_{\text{set}} + 3.2769 \tag{3.1}$$

where I_{set} is the current setting of the induction heater, and H is the resultant field inside the coil. The current flowing in the coil (I) in Ampere is related to the I_{set}

through [156]

$$I = (18I_{\text{set}}) + 140. \tag{3.2}$$

For this experiment the current setting was set such that the field generated by the coil reaches approximately 14.5 $\text{kA}\,\text{m}^{-1}$.

3.5 COMSOL Simulation of Temperature Distribution in Agar Phantom

The experimental setup explained in Section 3.4 was reproduced in COMSOL to validate the temperature distribution of the seeds from theoretical calculations.

The “Heat Transfer in Solids” physics with surface to ambient radiation cooling boundary conditions on the surface of the phantom and convective cooling in the surroundings was used in a time-dependent study to find the temperature distribution inside the phantom. The calculated power for the long seeds was used as the heat source in the model, and the only initial condition in the model was the initial temperature of the phantom, for which the measured temperature by the probe was used (Figure 3-5).

The geometry of the model was subdivided into seeds with average mesh density of 9×10^{14} elements/m^3 and 5×10^{7} elements/m^3 within the tissue mimicking phantom and the seed prototypes.

The surface temperature obtained from the COMSOL model, and the experiment was compared by using a modified form of a gamma analysis

$$\Gamma(r_m, r_c) = \sqrt{\frac{|r_c - r_m|^2}{\Delta d_m^2} + \frac{[T_c(r_c) - T_m(r_m)]^2}{\Delta T_m^2}} \tag{3.3}$$

where r_c, and r_m are position vectors of the points in the calculated and measured

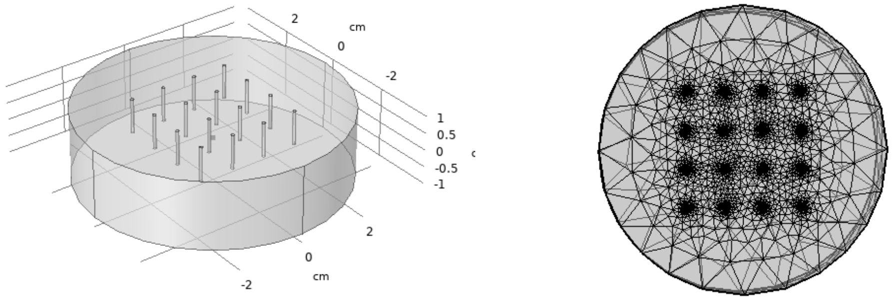

Figure 3-5: The geometry and mesh used for modeling the temperature distribution inside agar phantom.

temperature distribution maps respectively, and T_c, and T_m are the value of the temperature at the corresponding location inside the calculated and measured temperature map respectively. The distance-to-agreement criterion, and temperature difference criterion are denoted by Δd_m^2, and ΔT_m^2 respectively. Given that for every r_m position vector, there is a corresponding r_c, any point that satisfies $\Gamma(r_m, r_c) \leq 1$ will be accepted.

3.6 Modeling Temperautre Distribution in a Prostate for Realistic Patient-Specific Seed Distribution

An FEA program in COMSOL Multiphysics version 5.5 was used to model the temperature distribution within a realistic patient-specific prostate seed implant. A past permanent LDR prostate brachytherapy plan was used as a template to generate seed configuration: the LDR seeds were replaced by the TB seeds, and HT-only seeds were placed within the needles in the locations where the TB seeds were absent (Figure 3-6). The resulting geometry contains 94 TB seeds and 122 HT-only seeds (216 total) for this specific plan. The Bioheat Transfer was added as the physics to the geometry in COMSOL to solve the heat transfer equations in the tissue. The evolution of temperature distribution was carried out by a time dependent study. For time-dependent calculations the generalized minimal residual method (GMRES) solver was applied in which the iterative solution uses 0.001 absolute tolerance and 10^4 limit for maximum number of iterations. The geometry used to embed the patients plan consisted of a 8 cm in diameter and 6.5 cm in height cylindrical region depicting the prostate and a coaxial larger cylinder with 20 cm in diameter and 10 cm in height surrounding the inner cylinder representing the body tissue. The granularity of the mesh utilized for the geometry was chosen based on the size of the objects and adjusted for obtaining stable results. The final choice was based on the most efficient granularity with stable results. The mesh density for the seeds was typically 1.2×10^{13} elements/m^3, whereas for the prostate and the exterior section it was 5.6×10^{10} and 8.8×10^6 elements/m^3 respectively (Figure 3-6).

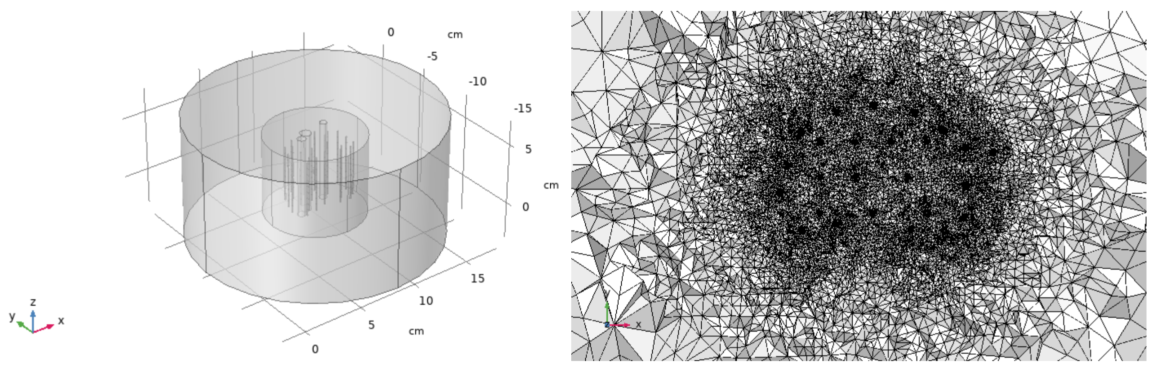

Figure 3-6: Modeled geometry for one of the patient-specific seed distributions in the patient phantom (left) and corresponding mesh (right).

On top of each of these granularized regions we have used mesh adaptation for more efficiency, and accuracy. The reason for this choice is the significant difference between the dimensions of the TB seeds and the total area of the prostate and the necessity of continuous transition on the boundaries. COMSOL Multiphysics can do the adaptation based on built-in error estimates.

Multiple studies have shown the blood perfusion inside prostate is heterogeneous with concentrated high blood perfusion spots in cancerous areas [157, 158]. A study with multimodality imaging methods revealed that the average vascular perfusion rate for normal prostate is 0.21 $\mathrm{mL\,g^{-1}\,min^{-1}}$ and for prostate cancer is 0.64 $\mathrm{mL\,g^{-1}\,min^{-1}}$ [157]. As a result, these values were used in our study for the normal and high vascular perfusion regions. The high vascular perfusion regions were added to the geometry in the simulation as multiple small cylinders.

3.7 Magnetic Field Distribution inside the Tissue

To investigate the magnetic field distribution in the presence of multiple seeds (>200) that are laterally separated by about 1 cm and validate our assumptions in Section 2.7 a frequency domain model in COMSOL multiphysics was used.

The physics for this model was Magnetic Field, and the geometry was similar to the geometry in Section 3.6 to understand the effects in a real situation with large number of seeds. The relative tolerance used for the multifrontal massively parallel sparse direct solver (MUMPS) was 0.01. The average density of mesh used for this model was 4×10^{13} elements/m^3 in the seed regions, 3×10^{12} elements/m^3 in the prostate region, and 1.2×10^9 elements/m^3 in the rest of the geometry with some adaptive meshing at the time of solution.

For all FEA simulations in this chapter in COMSOL Multiphysics, a desktop computer with forty-eight 2.2 GHz CPU cores and 128GB of RAM was utilized.

Chapter 4

Results

4.1 Parasitic Inductance

The correction terms for a practical core (Section 2.2.2) were calculated by using the values of the circuit elements. At input frequency range between 50 kHz to 200 kHz, our calculations show, among the corrections, non-linearity correction (κ_L), has the highest effect, and all the others can be neglected. This confirms that equation (2.26) can be used to find the parasitic inductance (Table 4.1).

Table 4.1: The magnitude of the correction terms for the 16-turn coil at frequency values of 50 kHz and 200 kHz.

correction	$f = 50$ kHz	$f = 200$ kHz
κ_L	0.90	0.90
L_s	4.2 nH	4.2 nH
L_m	3.7 nH	3.7 nH
L_i	0.25 nH	0.18 nH

To calculate the parasitic inductance, we used 5 helical windings of 12, 14, 16, 18, 20 turns (Table 4.2) and measured their inductance and fitted the results with N^2/ℓ_c as parameter. The results show that the parasitic inductance is in the range

141 ± 6.78 nH (Figure 4-1).

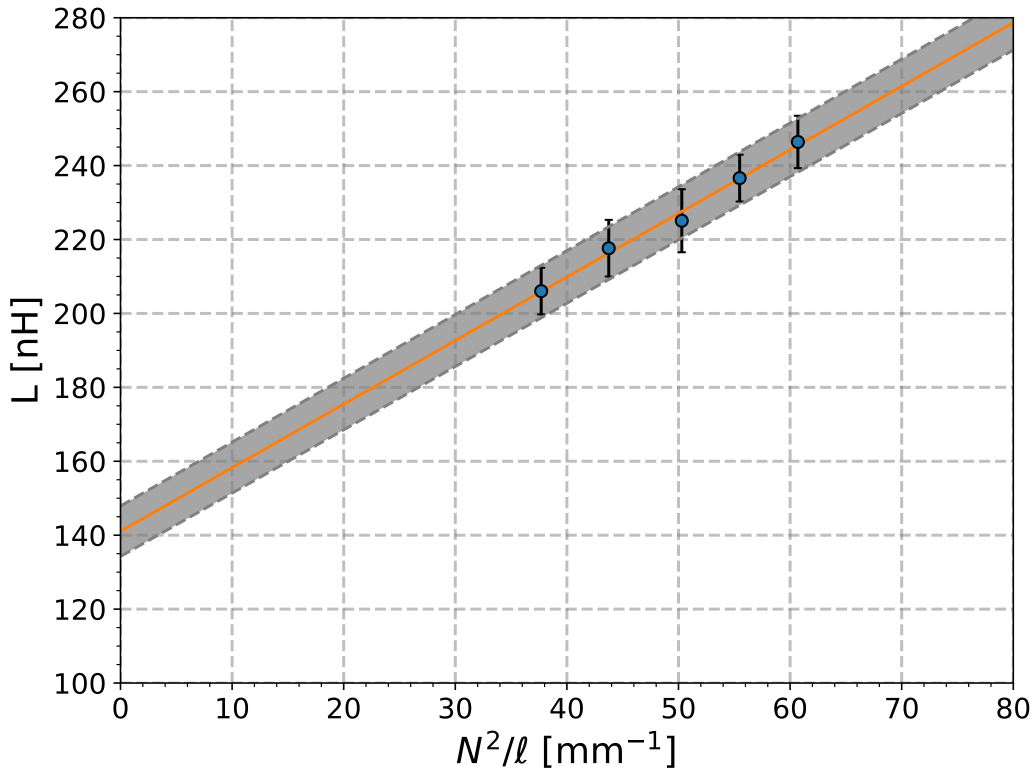

Figure 4-1: Inductance of the solenoids over a range of five N^2/ℓ values. The yellow solid line is the linear fit to the data. The ordinate intercept represents the value of the parasitic inductance (L_{par}). The error bars represent $\pm 2\sigma$.

The 16-turn helical solenoid is the one used as the tight winding around the ferrite core in what follows, therefore, measuring its inductance and resistance when the core is not present allowed us to calculate $L_{c_{\text{air}}}$ used in equation (2.36), and winding resistance r_w in equation (2.38). The value of $L_{c_{\text{air}}}$ was then compared to the results obtained from COMSOL simulations from Section 3.2 (Table 4.3).

Since for air one expects to have $\mu'' = 0$, the measured resistance for a coreless

Table 4.2: The coils used in the circuit to find the parasitic inductance.

turns	length [mm]	outer diameter [mm]
12	3.82 ± 0.05	1.6 ± 0.05
14	4.48 ± 0.05	1.6 ± 0.05
16	5.09 ± 0.05	1.6 ± 0.05
18	5.84 ± 0.05	1.6 ± 0.05
20	6.59 ± 0.05	1.6 ± 0.05

Table 4.3: The inductance values obtained from theory, COMSOL simulations, and measurements.

turns	Theory [nH]	COMSOL [nH]	Measured [nH]
16	73	70.4	82 ± 12

solenoid from equation (2.7) is entirely from winding resistance and some small corrections due to discreteness. Both inductance and resistance of the 16-turn coreless solenoid was measured (Figure 4-2). The measured values were used to calibrate the calculated inductance in the presence of a core.

Three key parameters were calculated: the value for $r_w = 107.6 \pm 2.6$ mΩ from Equation (2.7), as well as $\beta = 1.72 \pm 0.13$ nH mm from Equation (2.26) and $L_{\mathrm{par}} = 141 \pm 6.78$ nH from the linear regression fit shown in Figure 4-2. The fit value for β corresponds to a solenoid diameter of 1.39 ± 0.05 mm, which is within the error margin of the estimated diameter (1.33 ± 0.05 mm) and acts as a check of the experimental method.

The winding resistance was expected to vary linearly with temperature because the solenoid's temperature was changed during the experiments [159]. To characterize this, measurements were taken on a core-less solenoid with 16 turns exposed to temperatures ranging from 30 °C to 60 °C. The results in Figure 4-2 demonstrate

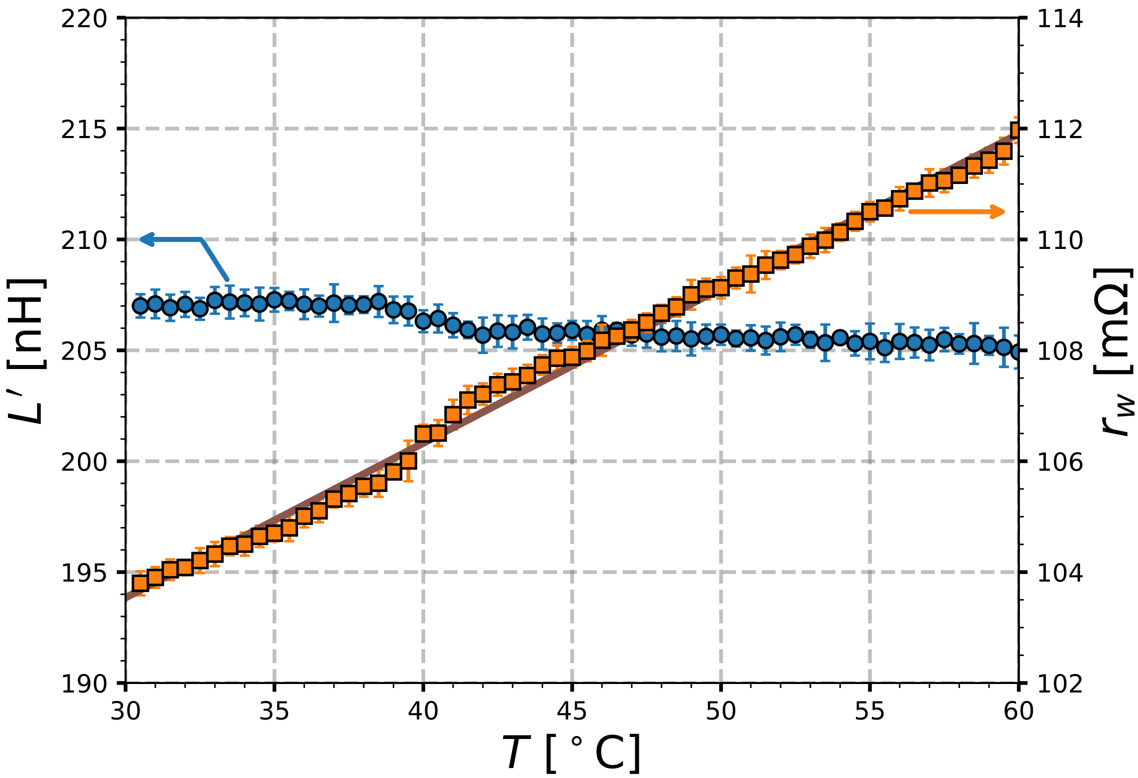

Figure 4-2: Dependence of the winding resistance r_w and measured inductance L' on temperature. The errorbars represent $\pm 2\sigma$.

that the inductance $L' = 206.1 \pm 0.8$ nH has a negligible temperature dependence, whereas the winding resistance varied with a linear fit $r_w = 0.279T + 95.17$ mΩ, where T was the temperature in degrees Celsius. In subsequent experiments, a solenoid with 16 turns, an effective diameter of 1.28 mm, and a nominal length of 5.0 mm was used. The corresponding L_{par} and temperature-corrected r_w were used to calibrate the measurements in the presence of the ferrite core.

When dealing with a discrete set of points obtained with some sampling rate via oscilloscope the fit to the data does not result in accurate fitting parameters and this results in some finite area in the B-H curve. The impact of discreteness on the B-H curve area is embedded in the calculated parameter r_w and is subsequently deducted from the B-H curve area upon the removal of r_w. The size of the area depends on the sampling rate of the oscilloscope (Figure 4-3). The sampling rate of the oscilloscope was set to 2×10^{-8} s, which according to Figure 4-3, creates $\sim$1 J/m^3 error for $\mu' = 10$.

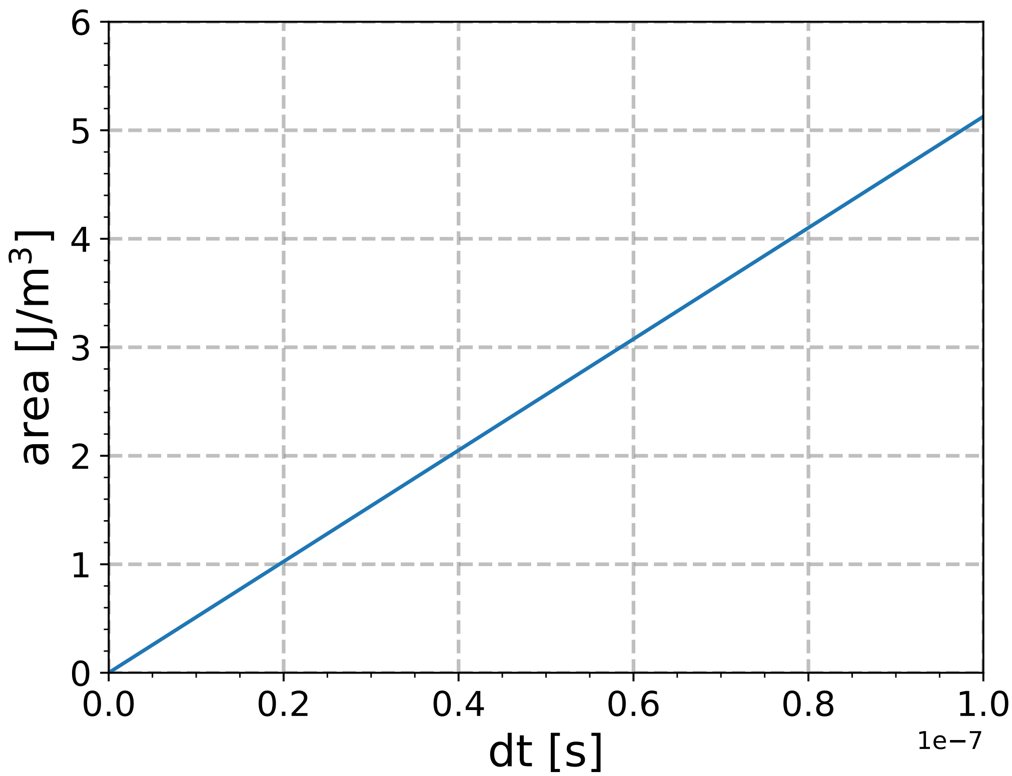

Figure 4-3: The area of the B-H curve due to errors raised from fitting the discrete data at $\mu' = 10$. As the sampling rate increases the error decreases.

4.2 Relative Permeability

The generator was set to provide a sine wave with frequency 50 kHz according to SAR limit (Section 1.5.10). The measured voltage at the nodes A, and B at low field amplitudes were close to sinusoidal, whereas at higher values voltage at point B showed nonlinearity.

A 0.94 mm diameter sample and a 0.46 mm diameter both 5 mm long were investigated, with the former as a core sample for an HT-only seed and the latter as a core sample for TB seeds.

Figure 4-4 depicts the extrinsic B-H curves obtained for the ferrite sample at different temperatures and the peak field amplitude of 3.5 $\mathrm{kA\,m^{-1}}$.

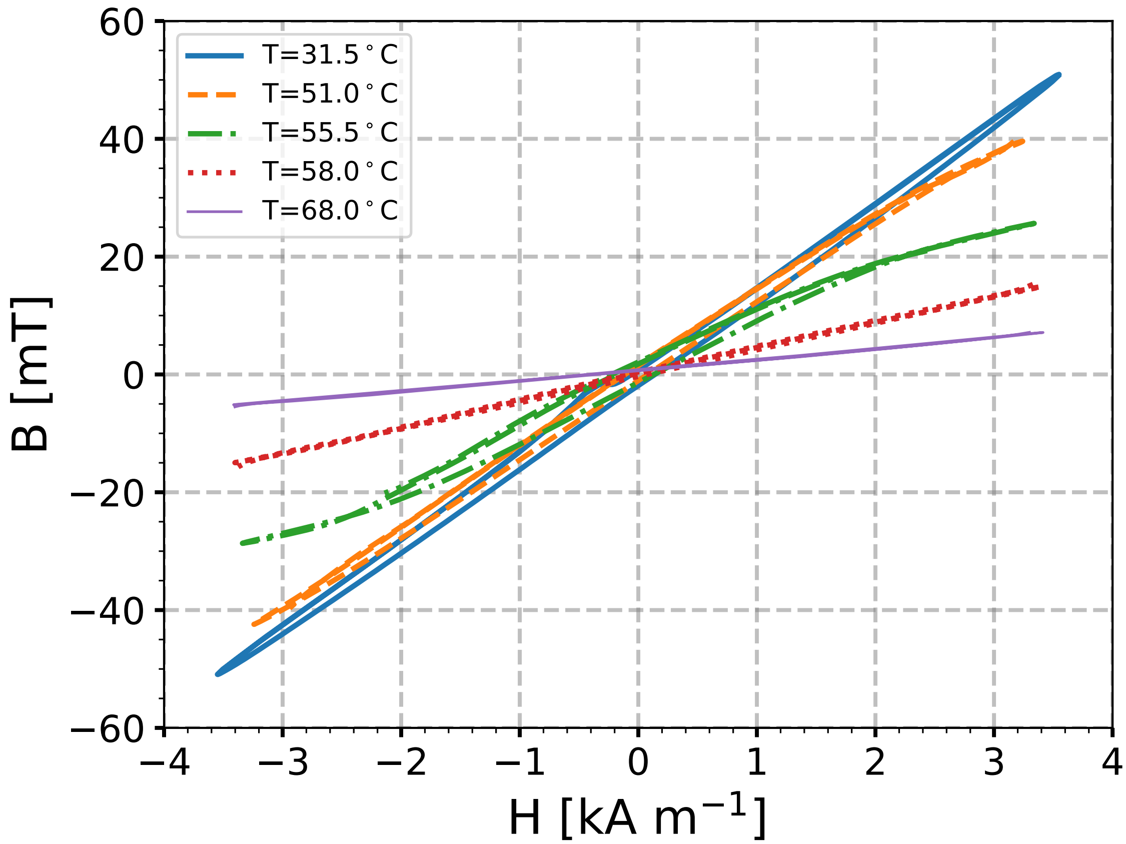

Figure 4-4: B-H curve of the ferrite sample (0.94 mm in diameter, 5.0 mm in length) in a range of temperature at 50 kHz frequency and peak magnetic field of 3.5 $\mathrm{kA\,m^{-1}}$.

The permeability of the ferrite samples was measured using equations (2.39), and (2.36) depending on the strength of the magnetic field and the results are presented in Figure 4-5. The saturation magnetization (M_s) of the ferrite is temperature dependent, because as the temperature rises the thermal energy disaligns more of the domains and leaves less domains to align with the magnetic field and the saturation point is reached sooner. Therefore, at higher temperatures there are less number of domains to align and the permeability drops (see constant field amplitude lines in Figure 4-5). On the other hand, at a constant temperature it is clear that as field strength increases the saturation effects appear and the permeability drops. As a result of these two effects, the sharpness of the Curie transition diminishes at higher field amplitudes. This is attributed to a preceding drop in permeability occurring before reaching the Curie temperature.

The permeability of the TB core is higher than HT-only core, since the aspect ratio is smaller and demagnetization effect is less significant (Figure 4-6).

In addition to magnetic field amplitude, and temperature the permeability depends on the frequency (Figure 4-7).

The permeability of cylindrical ferrite samples of different lengths and same diameter are compared in Figure 4-8. The effect of the demagnetization factor on the aspect ratio can be seen clearly in this figure when the sample is longer, and the poles are farther from each other.

The imaginary component of the relative permeability is calculated from equation (2.38) for low and high magnetic field amplitudes, and the results are shown in Figure 4-9.

As we expect, the imaginary component of the permeability is much smaller compared to the real component $\mu'/\mu'' \sim 33$, since soft ferrites have relatively small hysteresis area.

Figure 4-10 shows, the permeability of a toroid sample. The huge difference between the permeability of the toroid and the cylindrical sample shows the significant impact of the demagnetization factor.

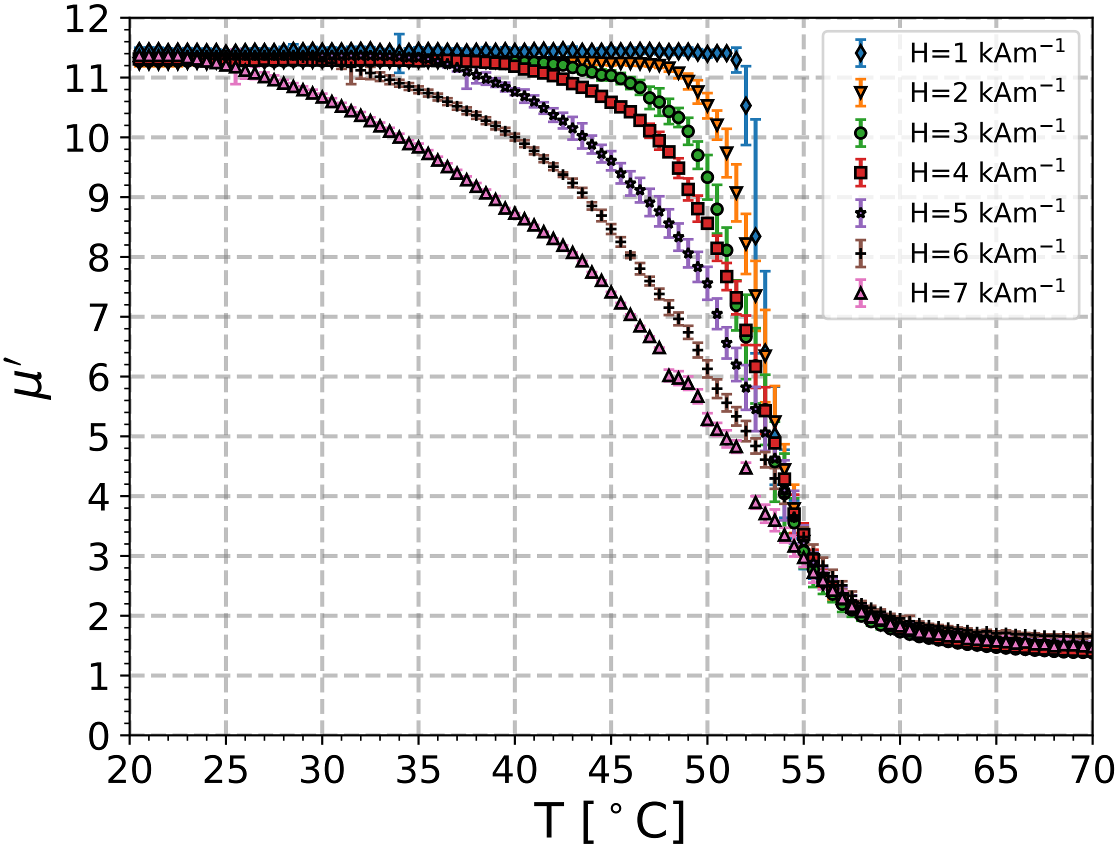

Figure 4-5: The permeability of the ferrite sample (0.94 mm in diameter, 5.0 mm in length) as a function of temperature at 50 kHz in a range of magnetic field strengths. The errorbars represent $\pm 2\sigma$.

4.3 Power Generation

The optimum shell thickness to generate maximum power at frequency 50 kHz, was calculated by finding the maximum of the power vs temperature model for three different type of shell materials (Figure 4-11).

For a HT-only seed with a golden shell the optimum thickness is 0.038 mm bringing the total seed's diameter to 1.016 mm which is within the acceptable clinical range (i.e. 17 gauge needle, 1.067 mm inner diameter). With this thickness the power

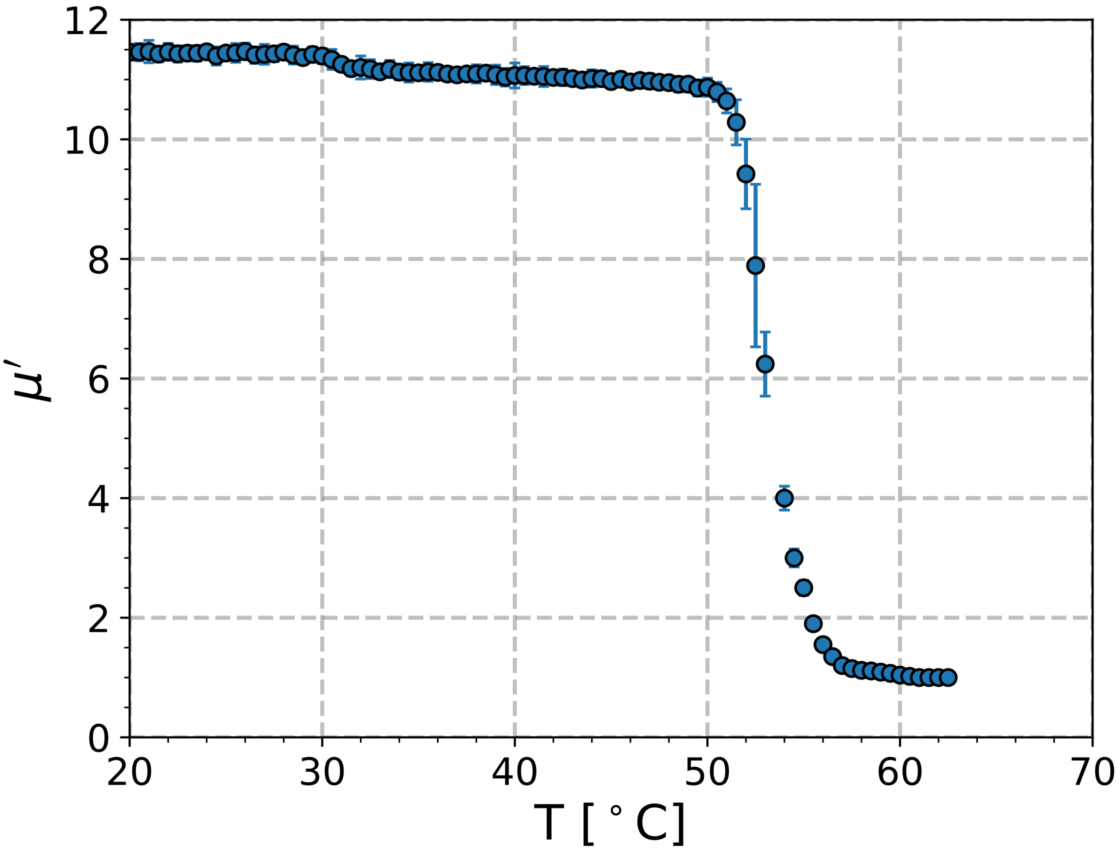

Figure 4-6: The permeability of a ferrite core designed for TB seed with diameter 0.44 mm, and length 5 mm at peak magnetic field strength of 1 $\mathrm{kA\,m^{-1}}$. The errorbar represents $\pm 2\sigma$.

generated by the HT-only seed at 37 °C is 248 mW. A TB seed needs to have a 0.2 mm thick golden shell to achieve its maximum power of 47 mW (Figure 4-12). The total diameter of the TB seed with this choice will be 0.84 mm which is also in the acceptable clinical range, and it is thin enough to be visually distinguishable from the HT-only seeds when the physician is inserting them.

At a peak field amplitude of 10 $\mathrm{kA\,m^{-1}}$ after attenuation by body tissue and the shell, the field amplitude that reaches the HT-only seed's ferrite core is $\sim$8.5 $\mathrm{kA\,m^{-1}}$ and for TB seed is $\sim$6 $\mathrm{kA\,m^{-1}}$ for an average person. To calculate the attenuation

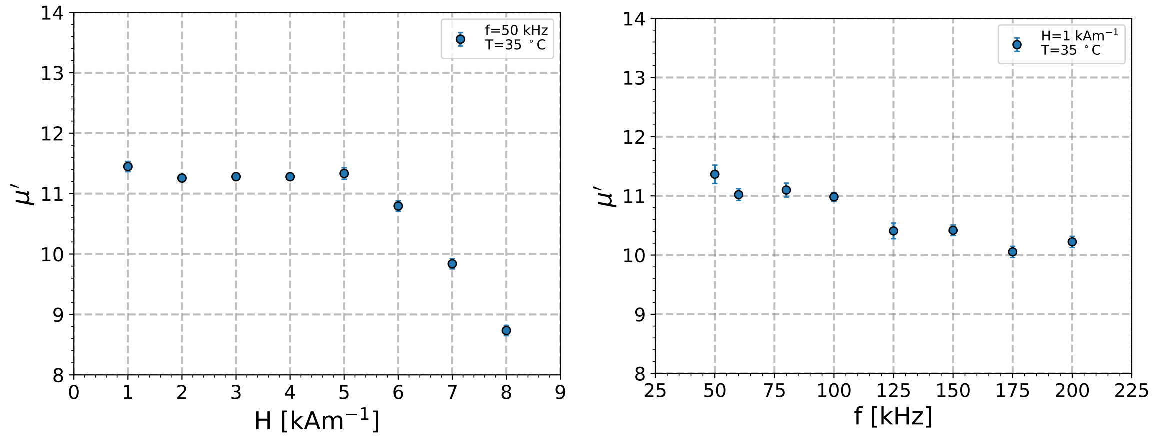

Figure 4-7: Left: Permeability of the sample at a fixed magnetic field 1 $\mathrm{kA\,m^{-1}}$ in frequency range of 50 kHz to 200 kHz Right: Permeability of the sample at a fixed frequency 50 kHz in a range of magnetic field amplitudes. The errorbars represent $\pm 2\sigma$.

by the tissue we have used an average thickness value of 3.6 cm for fat, 9 cm for muscle, 2.8 cm for cancellous bone, 0.8 cm for cordial bone, and finally 2.5 cm for prostate, which was obtained by direct measurements on multiple patients CT images. The electrical properties of different components of body tissue are obtained from S. Gabriel et al. [95, 97, 160]. The power generated by the eddy current and hysteresis losses of the HT-only seed's ferrite core was on the order 8 mW, which was a ∼33 times smaller than the power generated by the shell (Figure 4-13).

Compared to other materials such as copper and titanium, gold is the better choice, since a golden shell can generate more power than titanium with less thickness. Gold is also biocompatible, in contrast to copper, and has a higher maximal power.

Upon determining the optimal thickness, the resultant power generated by the seed, as obtained from COMSOL simulations incorporating B-H curves derived from measurements, was compared to the calculated power from the power versus temperature model. Figure 4-14 demonstrates that, on average, both techniques show agreement

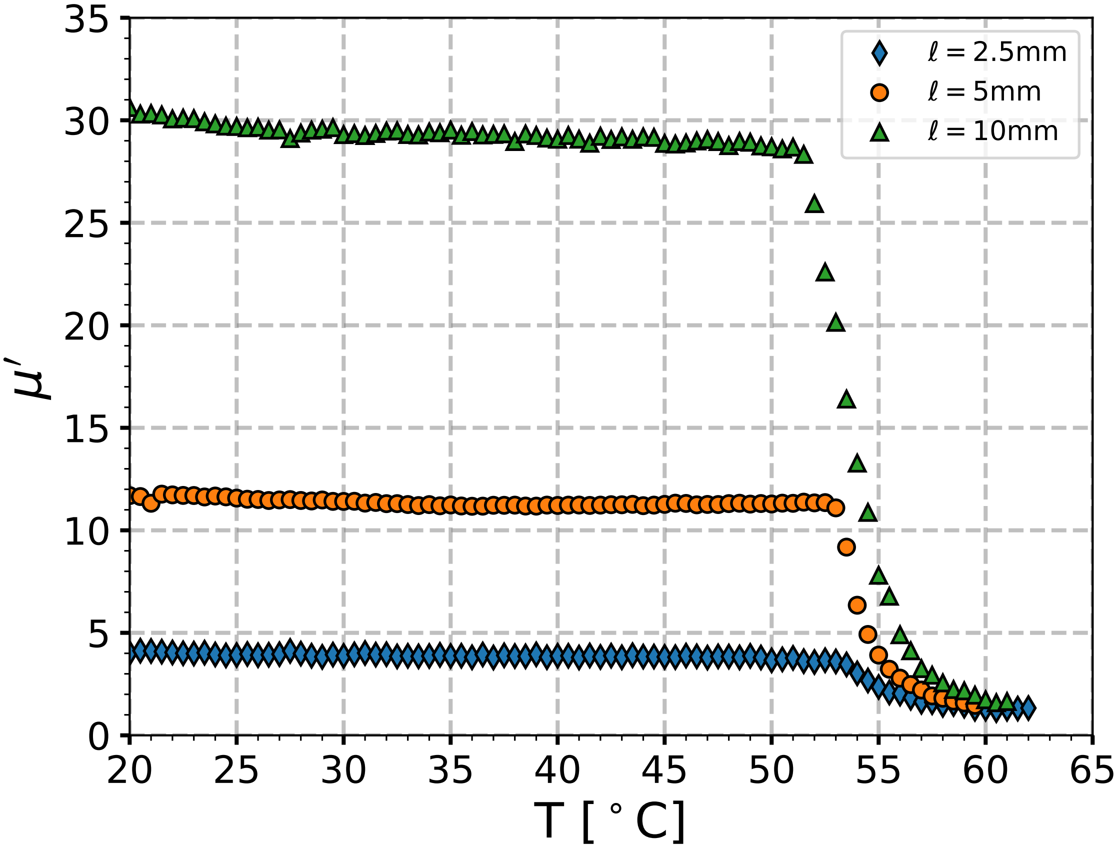

Figure 4-8: Permeability of the long ferrite (1 cm), normal size ferrite (0.5 cm), and a short ferrite (0.25 cm) samples at 50 kHz and 1 $\mathrm{kA\,m^{-1}}$. The demagnetization effect becomes more pronounced as length decreases.

within 7%.

Note that the COMSOL simulations were conducted for a single seed in an axisymmetric manner. Extending this analysis to a general case, where axial symmetry is broken, and performing direct temperature distribution calculations for hundreds of seeds in three dimensions through Joule heating, would be computationally overwhelming. Consequently, although we utilized the power versus temperature model to determine the optimum thickness, for a three-dimensional geometry, we can employ

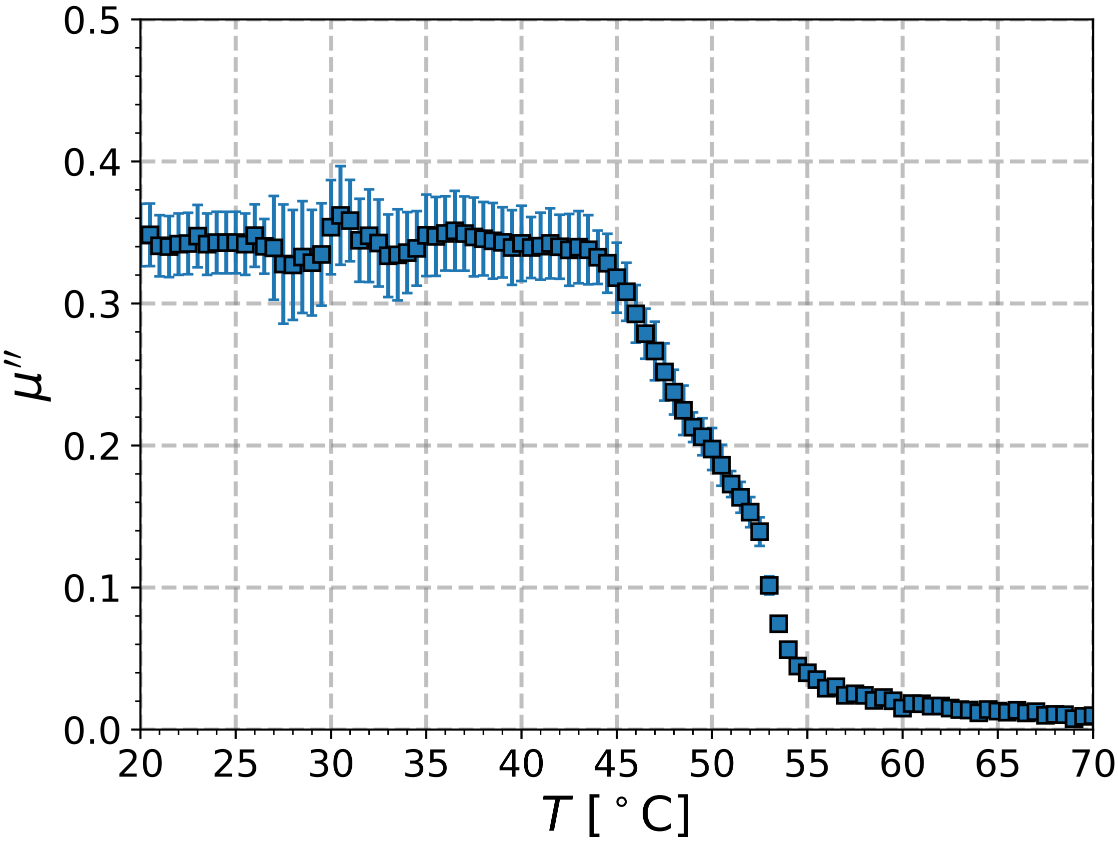

Figure 4-9: Imaginary component of the magnetic permeability for the ferrite sample at 50 kHz and 3.5 kA m^{-1} (0.94 mm in diameter, 5.0 mm in length). The errorbars represent $\pm 2\sigma$.

either the power obtained from COMSOL or the power versus temperature model as a heat source to ascertain the temperature distribution within the tissue.

4.4 Structural Resilience of Seeds under Thermal Expansion Stress

The resilience of the seed shell under thermal expansion stress was assessed by quantifying the changes in length for both the shell and the ferrite core. The results of

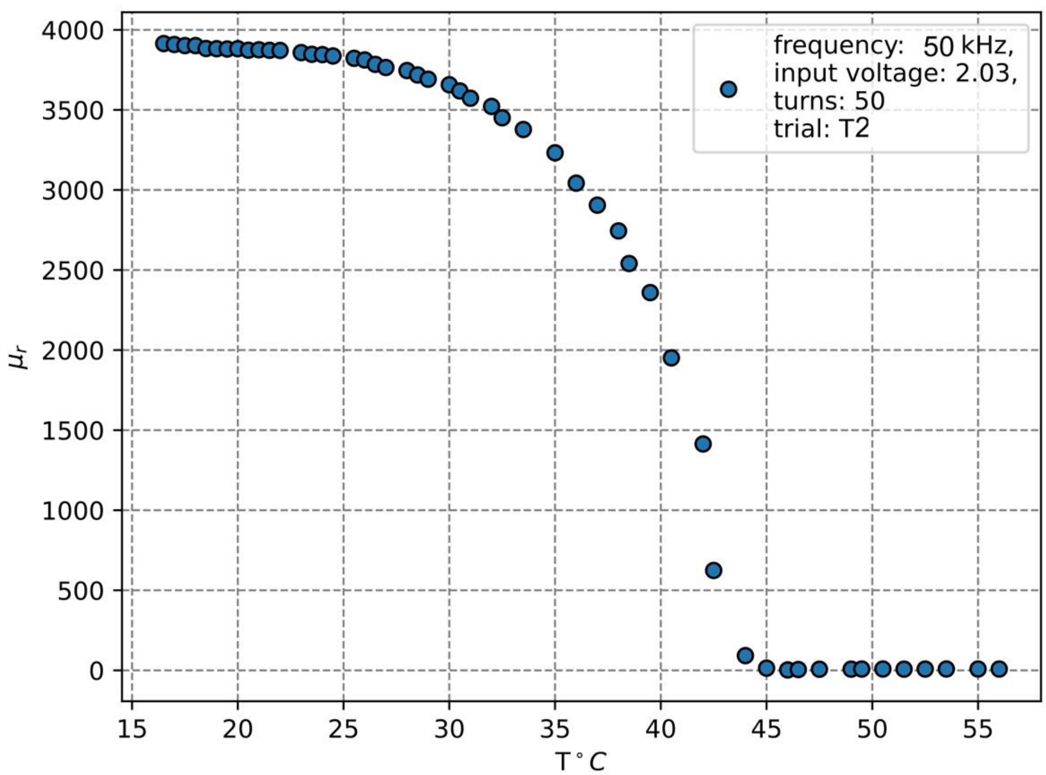

Figure 4-10: Permeability of a toroid ferrite sample.

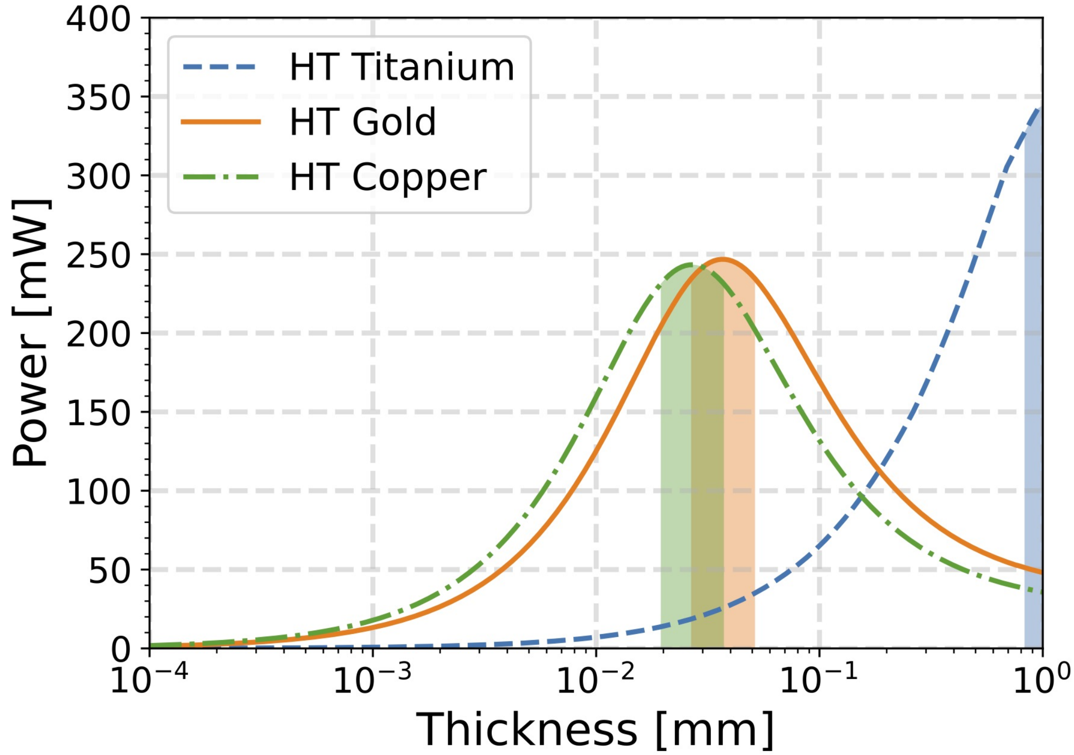

Figure 4-11: The change in power versus shell thickness for gold, copper, and titanium shell materials for HT-only seeds (0.94 mm in diameter, 5.0 mm in length) at temperature 37 °C. The shaded area represents the range of thickness at which the power remains at 90% of the maximum. The power drops rapidly as the thickness deviates from the optimal value.

our calculations within a temperature range of 20-70°C are presented in Table 4.4. The stress applied to the cap of the seed in the case of the golden shell is zero, as the golden shell expands more than the ferrite core. In contrast, the titanium capsule expands at a slower rate than the ferrite core. The stress exerted on the cap of the titanium shell is approximately 1.9×10^7 N/m^2, which falls below the maximum tolerable plastic

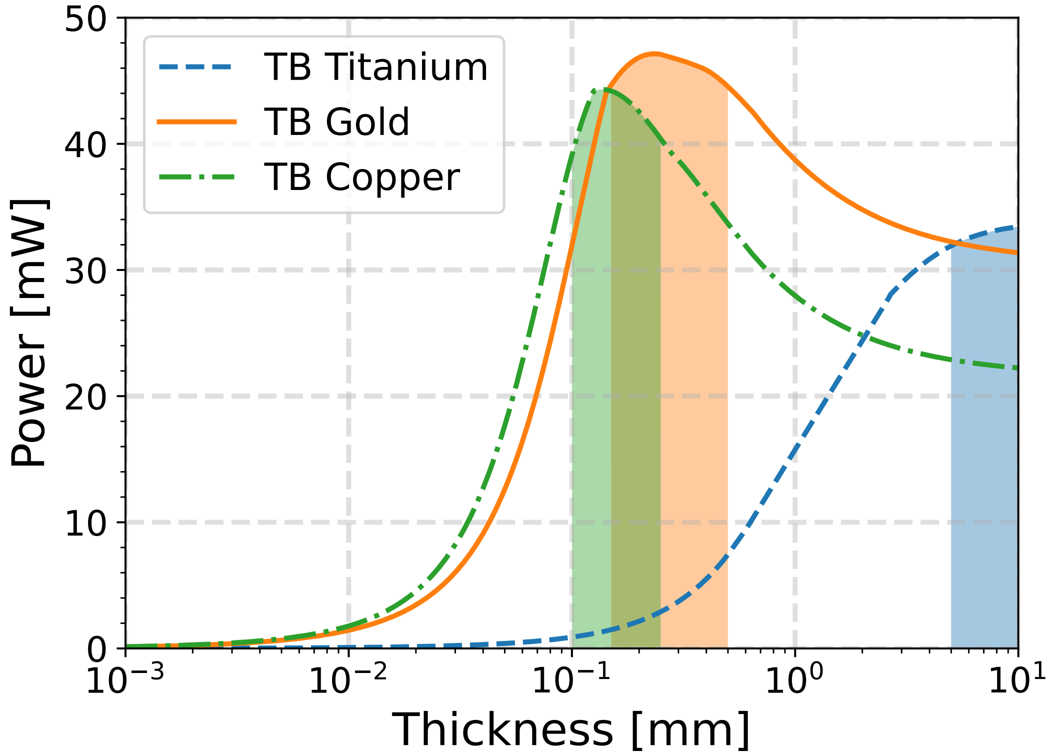

Figure 4-12: The change in power versus shell thickness for gold, copper, and titanium shell materials for TB seeds (0.44 mm in diameter, 5.0 mm in length) at temperature 37 °C. The shaded area represents the range of thickness at which the power remains at 90% of the maximum. The power drops rapidly as the thickness deviates from the optimal value.

deformation limit for titanium ($\sim 24 \times 10^7$ N/m^2) [161]. Consequently, the titanium shell does not experience failure due to the thermal expansion of the core.

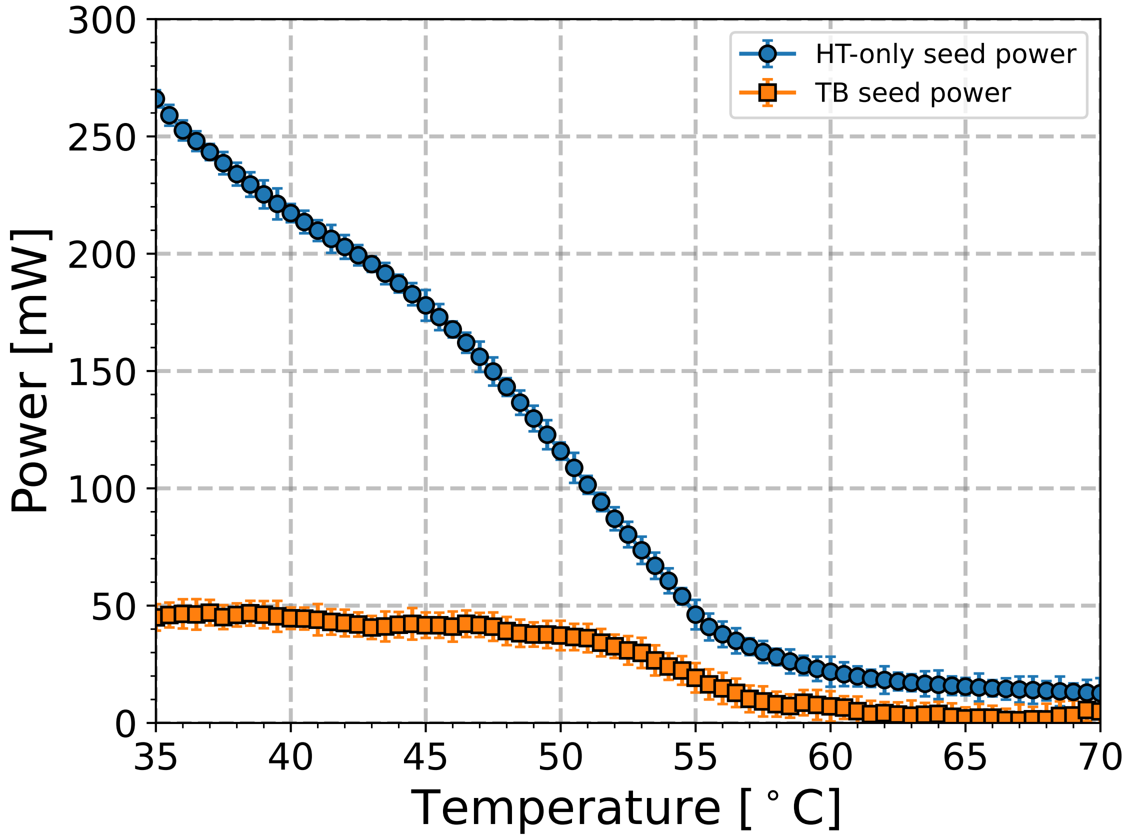

Figure 4-13: Power generated by the HT-only seed compared to the power generated by the TB seeds. The errorbars represents $\pm 2\sigma$.

4.5 Temperature Distribution in Agar Phantom vs COMSOL Simulations

Figure 4-15 shows temperature distribution at the surface of the agar phantom 30 seconds and 30 minutes after turning on the induction heater. The infrared images that were acquired from the agar phantom with the infrared camera after 30 minutes of heating were compared to the results obtained from COMSOL simulations. The ambient temperature of the surroundings (20.5 °C) at the time of experiment was given to the COMSOL model as initial condition. Using the gamma analysis with

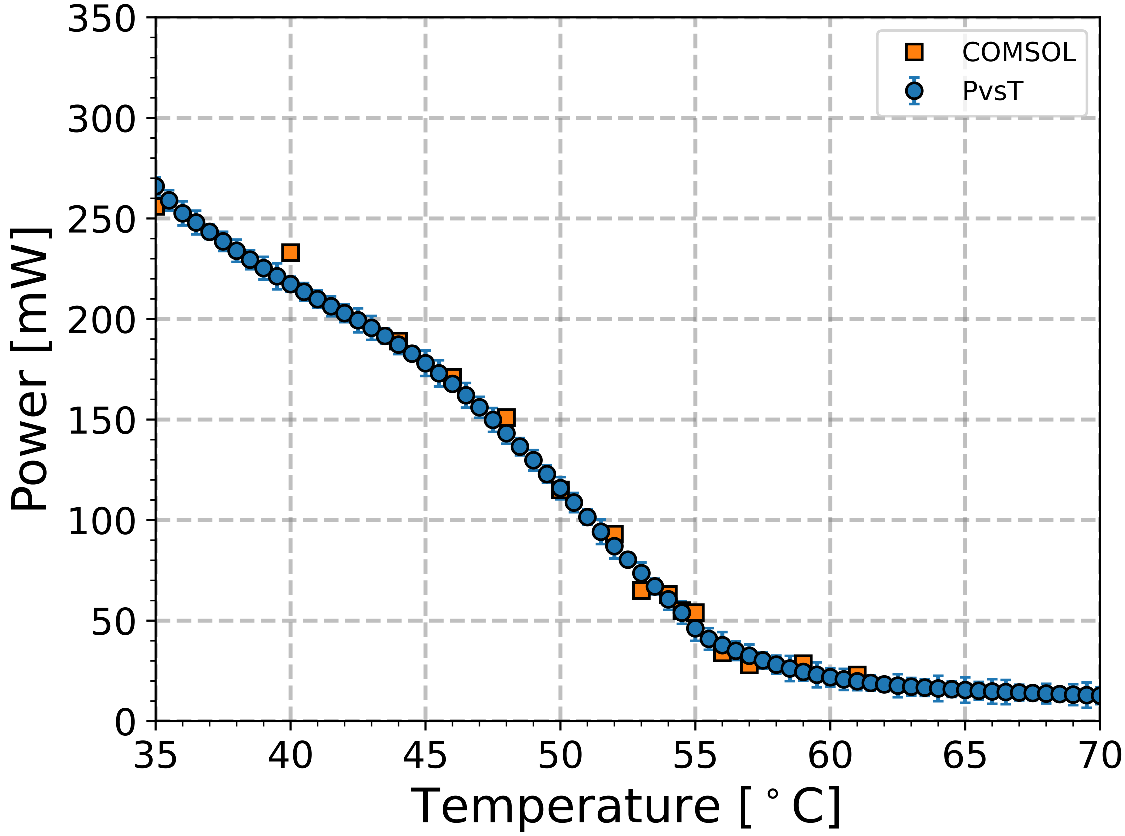

Figure 4-14: A comparison between the power calculated directly from Joule heating in COMSOL and the power versus temperature model. The average error between the two is 7%. The errorbars represent $\pm 2\sigma$.

$\Delta T_m = 1$ °C and $\Delta d_m = 1$ mm within 15 mm radius from the center of the images in Figure 4-16 resulted in a passing rate of 91.3%. Increasing ΔT_m to 1.5 °C increased the passing rate to 97.5%. The discrepancy between the two images resulted from the low resolution of the infrared camera (1.71 mm/pixel), which was not able to distinguish small sizes of the seeds (0.94 mm), and the fact that the low power generated by the seeds did not increase the temperature much above the surroundings, and therefore the thermal noise from the surroundings was significant.

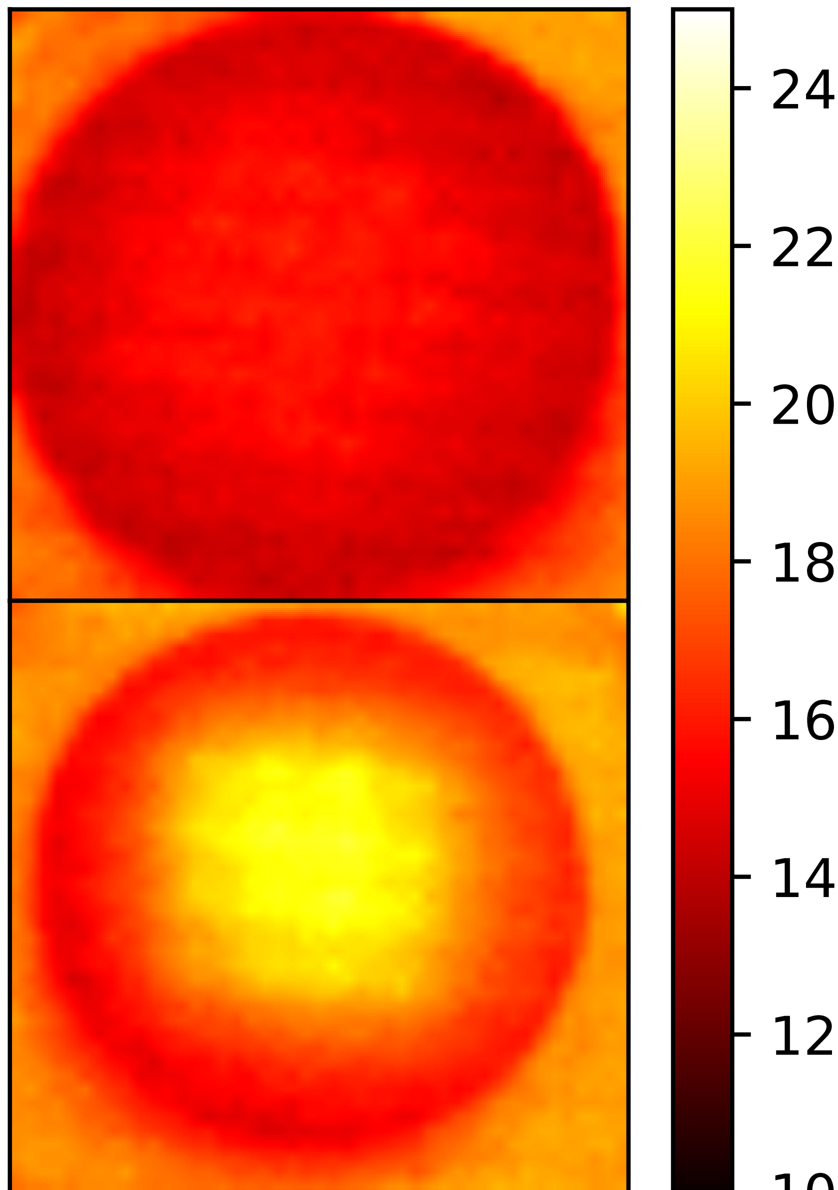

Figure 4-15: The temperature distribution at the surface of the agar phantom at (top) 30 s and (bottom) 30 min after turning on the induction heater.

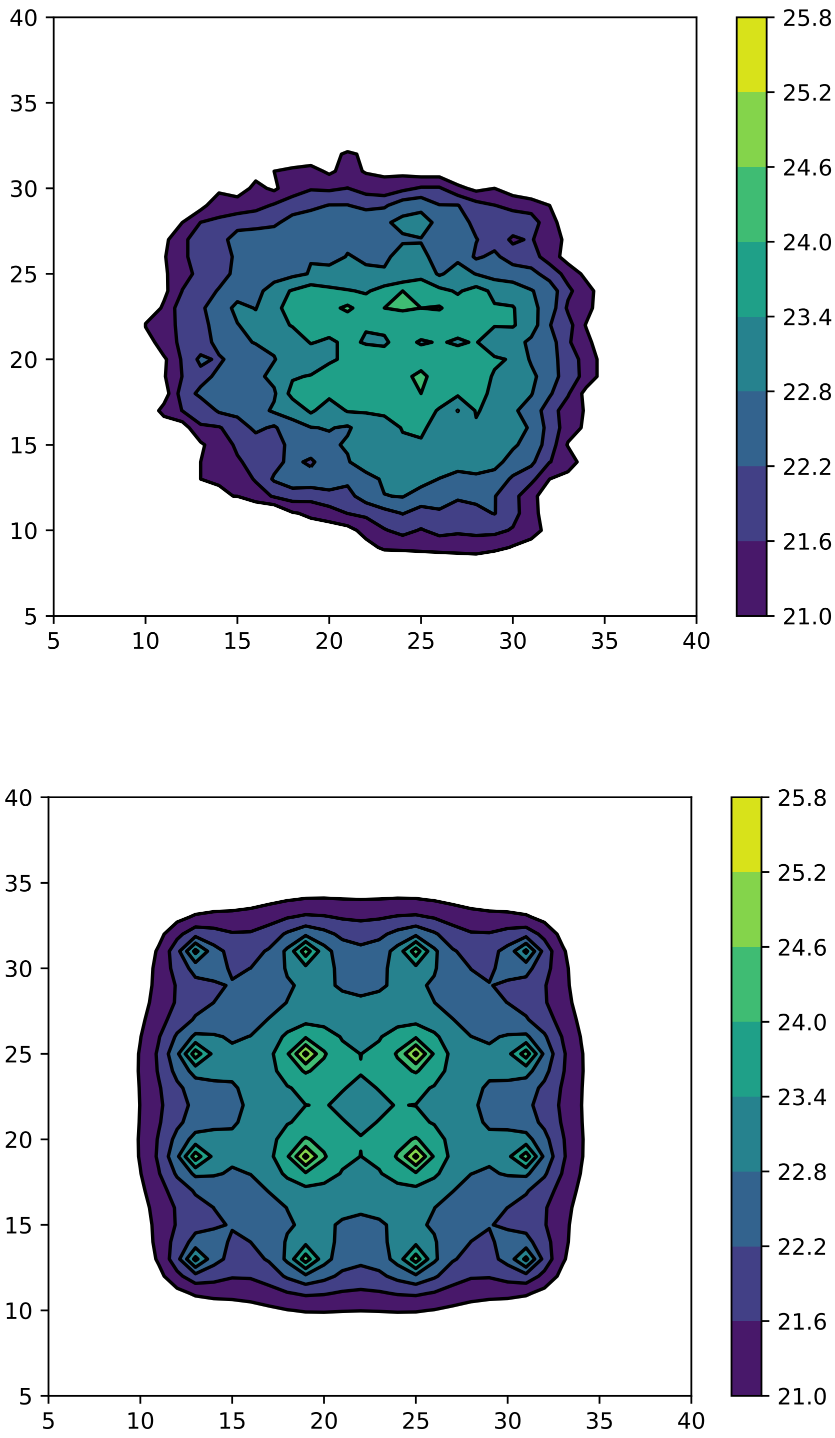

Figure 4-16: The heat map generated from temperature distribution in the phantom from the measurements on agar phantom (Top) and COMSOL simulations (Bottom) after 30 minutes of heating.

Table 4.4: The information about thermal expansion of ferrite and different materials in the temperature range of 20-70 °C that can be used as a shell surrounding the core. Other than titanium all the other shell materials have higher thermal expansion coefficient than the ferrite core indicating that there is little chance of radio active material leakage. Even in the case of titanium the shell has enough tolerance to withstand the strain from the core.

Parameter	Mn-Zn ferrite	Carbon coating	Gold	Titanium	Copper
Init. Length [mm]	4.54	4.84	5	5	5
Thermal Exp. Coef. [$\times 10^{-6}$ °C]	12.5	4.3	14.2	8.41	16
Length Chng. [mm]	0.00286	0.00107	0.00355	0.00210	0.00400
Rel. Length Chng.	6.3×10^{-4}	2.2×10^{-4}	7.1×10^{-4}	4.2×10^{-4}	8.0×10^{-4}

4.6 Modeling Temperature Distribution for Realistic Patient-Specific Seed Distribution

The results of simulations explained in Section 3.6 are depicted in Figure 4-17. It can be seen that the joint utilization of TB and HT-only seeds produces an adequate power supply for the hyperthermia treatment of the planning target volume (PTV). Our calculations for 4 different values of blood perfusion rates starting from 0.21 mL/g/min to 0.64 mL/g/min with the latter being the average extreme case, shows that the volume coverage for the 42 °C isotemperature surface is over 90% of the PTV (Figure 4-18).This indicates that the seeds provided enough power for hyperthermia treatment.

The power generated by the seed increases the temperature in the tissue until the seed reaches the Curie temperature at which point the ferrite core inside the seed loses

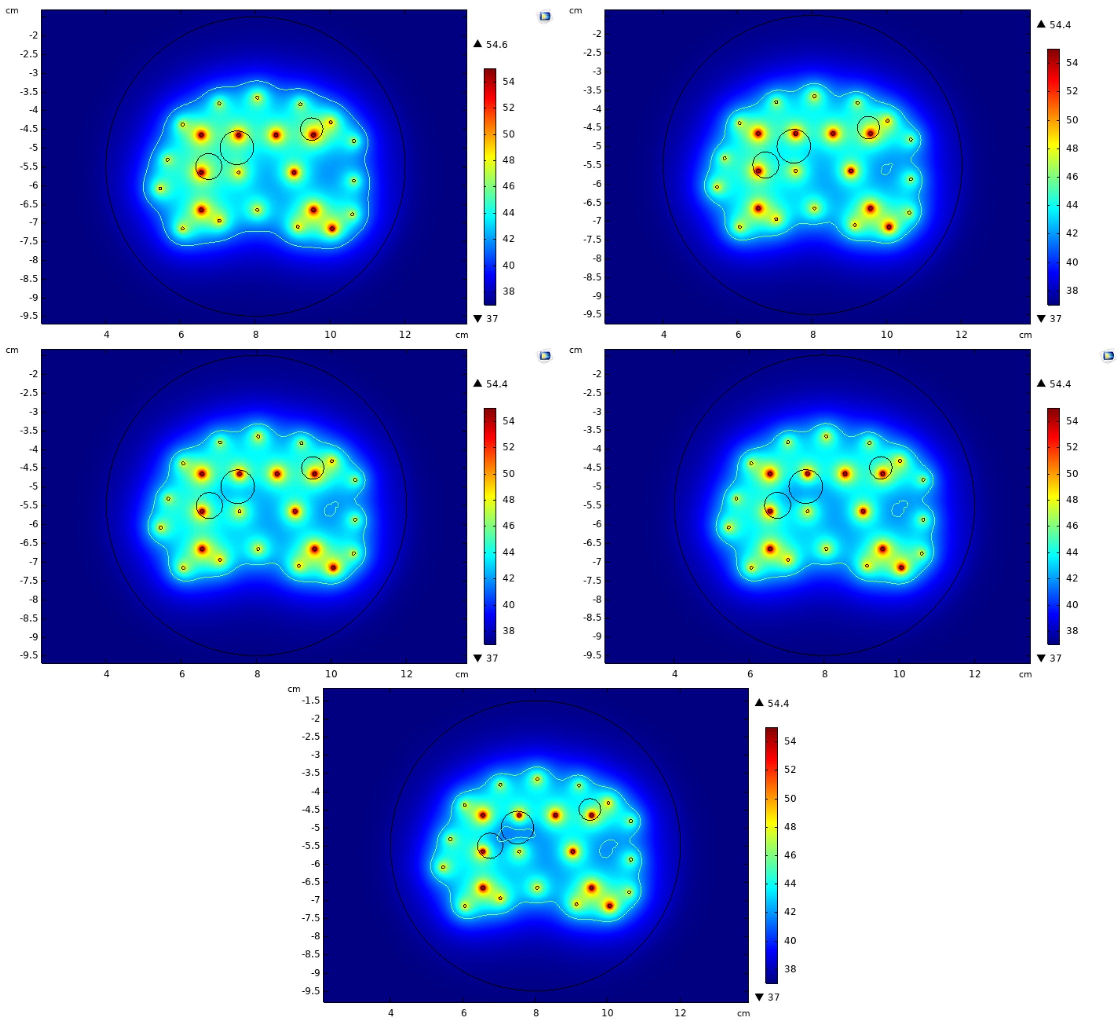

Figure 4-17: COMSOL-computed temperature distribution for a patient-specific TB and HT seed arrangement in the presence of vascular perfusion (top-left) 0.21 $\mathrm{mL\,g^{-1}\,min^{-1}}$, (top-right) 0.3 $\mathrm{mL\,g^{-1}\,min^{-1}}$, (middle-left) 0.4 $\mathrm{mL\,g^{-1}\,min^{-1}}$, (middle-right) 0.5 $\mathrm{mL\,g^{-1}\,min^{-1}}$, and (bottom) 0.64 $\mathrm{mL\,g^{-1}\,min^{-1}}$. The cyan line is the 42 °C isotemperature line and the three high blood perfusion regions are shown in small back circles.

its magnetic properties, and the power production drops. The dropped temperature allows the core to regain its magnetic properties and start to generate higher power again. This process stabilizes the temperature within the tissue at some constant

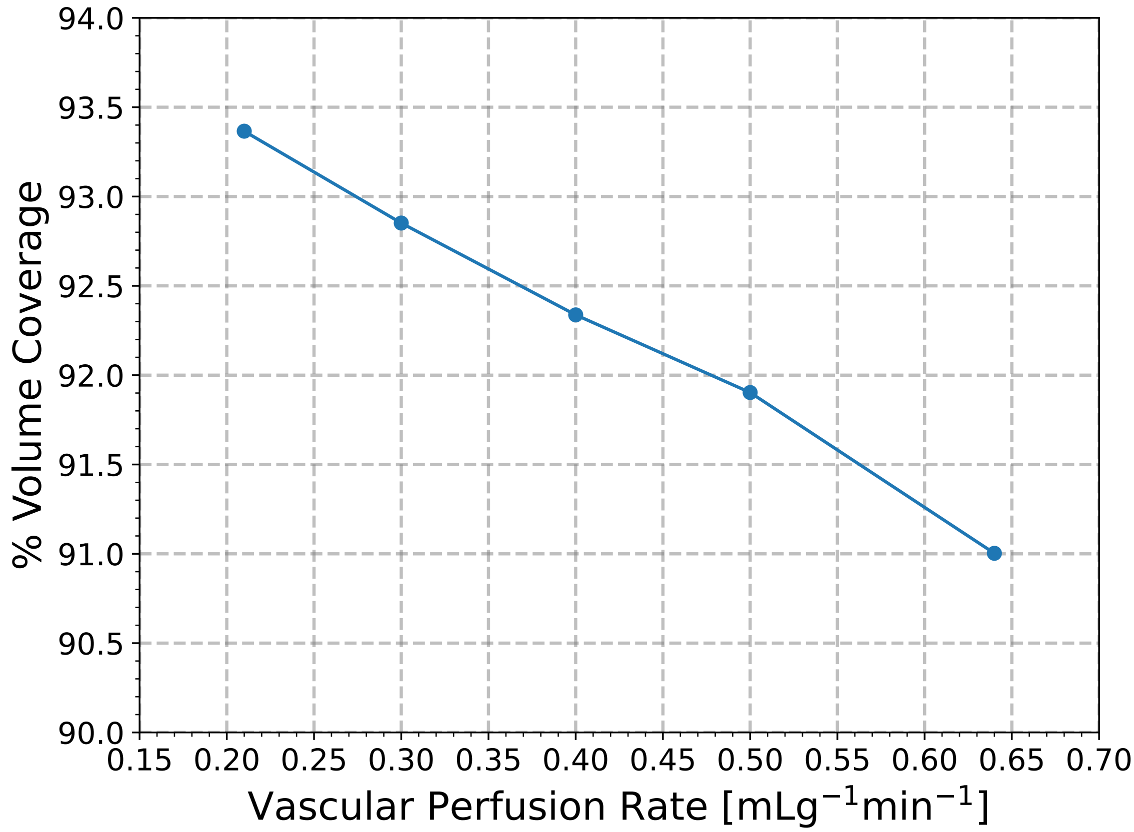

Figure 4-18: Percentage of the PTV with temperatures equal to and above 42 °C over a range of vascular perfusion rates.

temperature which is dependent on the Curie temperature of the ferrite, and the power generated by the seeds. Figure 4-19 shows that for current design of the seeds explained in Section 4.3 how the temperature in the center of the prostate changes with time. After a sharp raise in temperature in the first 10 minutes the temperature plateaus to an equilibrium value.

Table 4.5: Material properties used in COMSOL Multiphysics simulations and seed power optimization.

Material	Density $[\mathrm{kg/m^3}]$	Thermal Conductivity $[\mathrm{W\,m^{-1}\,K^{-1}}]$	Heat Capacity C_p $[\mathrm{J\,kg^{-1}\,K^{-1}}]$	Electrical Conductivity [S/m]
Adipose Tissue [162]	909	0.21	2065	N/A
Prostate Tissue [163–165]	1045	0.51	3760	N/A
Blood [162]	1147	0.46	3306	N/A
Ferrite[a]	750	4.27	4800	0.17
Titanium [166]	4540	21	523	2.4×10^6
Gold [167]	19320	310	126	4.11×10^7
Carbon[b]	2667	140	709	3×10^5

[a] Provided by National Magnetics Group, Inc.

[b] COMSOL Multiphysics coefficient library.

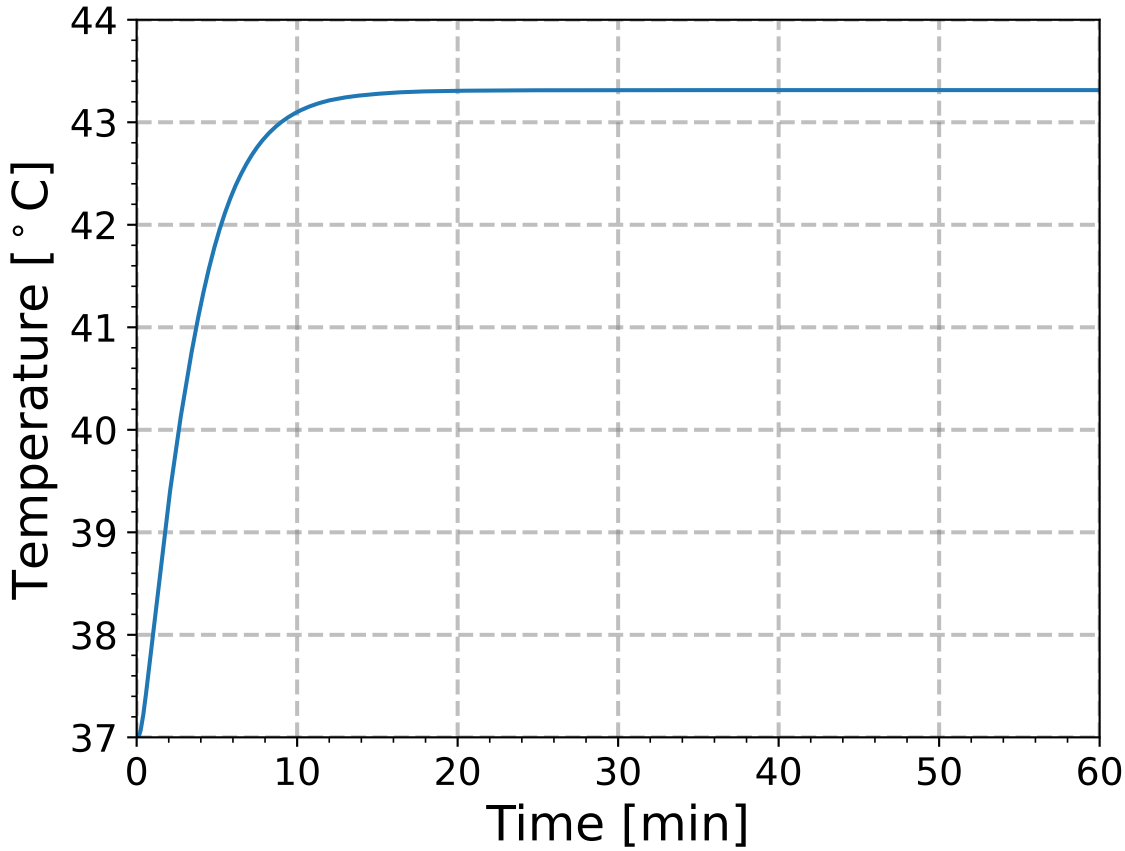

Figure 4-19: The time elapsed as the temperature in the center of the seed arrangement reaches its maximum for vascular perfusion 0.21 $\mathrm{mL\,g^{-1}\,min^{-1}}$

4.7 Interseed Effects on Magnetic Field Distribution

The field distribution inside the tissue obtained from simulations explained in Section 3.7 and was discussed in Section 2.7, shows minimal effect from the neighboring seeds in agreement with the expectations. The nearly complete cylindrical symmetry of the geometry and the small dimensions of the seeds compared to their lateral separation distance results in no masking effect by the outer seeds on the inner seeds (see Figure 4-20).

The seeds that are located in the same needle abutting each other increase the permeability and potentially the power. Even though these changes depends highly on the conditions and the seed ordering in the needle in the limiting case relative power increases no more than ~25% for an all-TB stack and ~45% for the all-HT-only stack (Figure 4-21).

The increase in the power only enhances thermal volume coverage of the prostate tissue compared to the conservative approach of treating seeds independently (see Figure 4-22). However, since the distribution is not known beforehand it is better to use the more conservative approach.

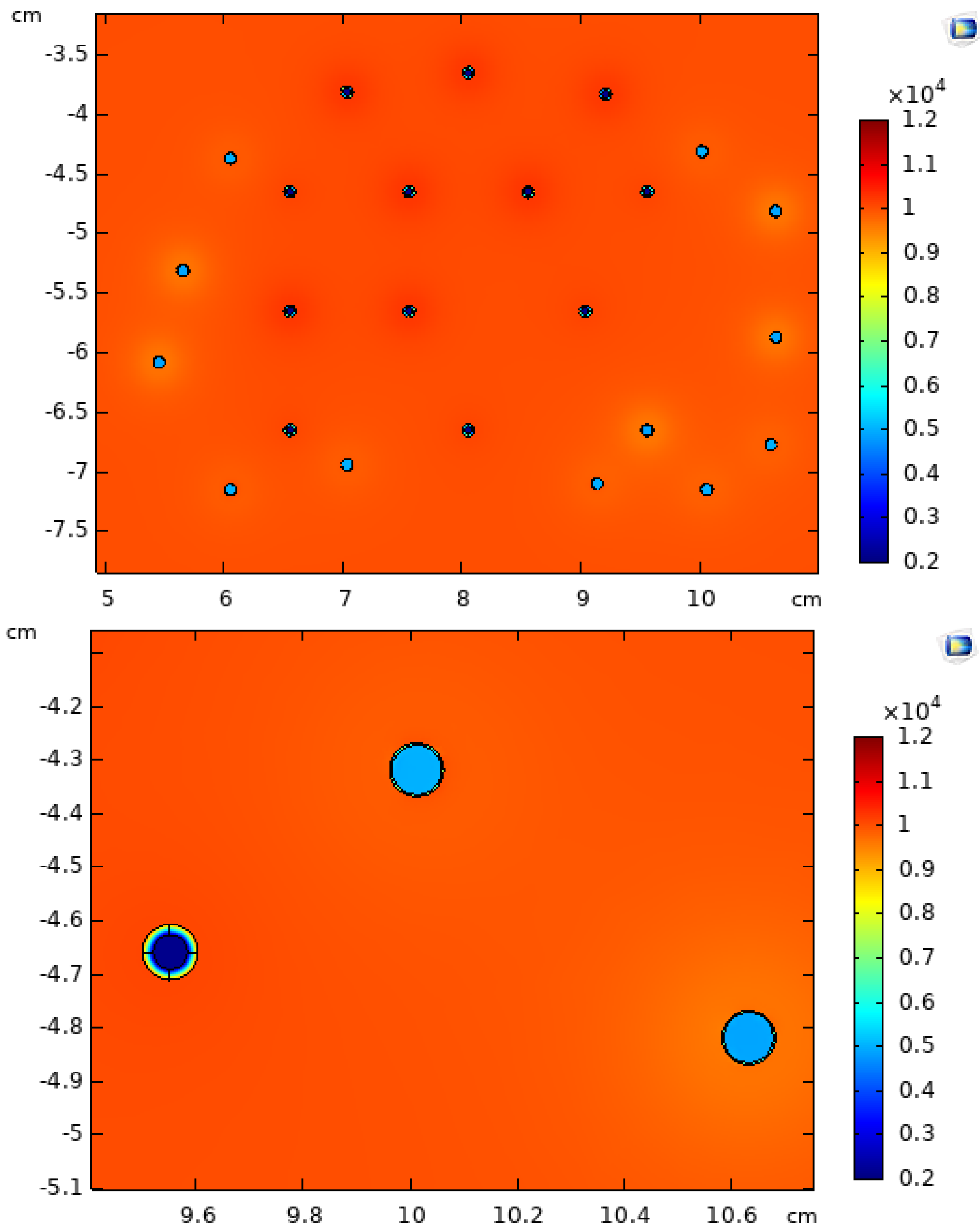

Figure 4-20: Top: The field distribution inside the Tissue. The small circles show the seeds, and the color represents the magnetic field strength. The field inside the volume is nearly uniform except for locations very close to the seeds. Bottom: The close up of two HT-only and on TB seed and the variation of the field in and around those seeds.

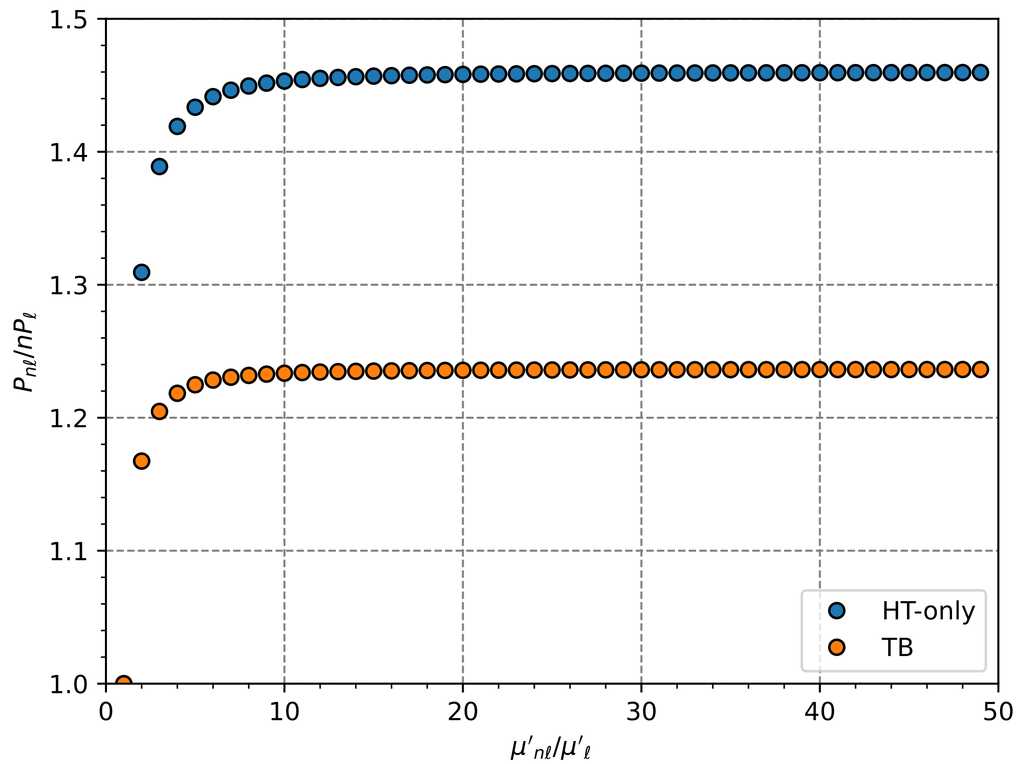

Figure 4-21: Relative change in power production for a range of $\mu'_{n\ell}/\mu'_\ell$ when the seeds in the needle act like a longer seed with higher permeability.

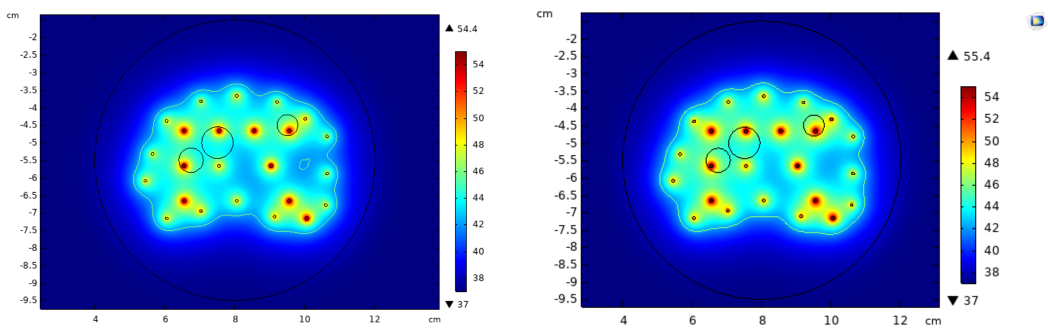

Figure 4-22: The temperature distribution inside the tissue with vascular perfusion rate of 0.3 $\mathrm{mL\,g^{-1}\,min^{-1}}$ excluding the end to end effect (left) and including the most extreme end to end case, which increases the power generation of TB seeds by 25% and HT-only seeds by 45%.(right)

Chapter 5

Discussion

Temperature and field amplitude dependence of the magnetic permeability was evaluated based on RL circuit parameter measurements. An increase in magnetic field amplitude took the sample deeper into saturation, hence the relative permeability decreased in agreement with previous studies [150]. At high field amplitudes, magnetic saturation resulted in smaller magnetic permeability and reduced the change in permeability at Curie temperature. Moreover, the magnetic saturation is temperature dependent, and higher temperatures, the same field amplitude took the ferrite core more into saturation, and the permeability gradually decreased with temperature (Figure 4-7).

The demagnetization effect in the cylindrical ferrite sample was another reason for reduced permeability values. For toroid shape ferrites where the topological length is infinite, the demagnetization effect does not exist, and permeability is in the order of a few thousand (our measurements show 5000 for current ferrite formulation), but for cylindrical shape samples as soon as they are placed in a magnetic field, magnetic poles form at each end. The magnetic poles generate a magnetic field proportional and in the opposite direction of the magnetization thus reduce magnetic permeability [144]

$$B = \mu_0 \left(H + M + H_d\right) = \mu_0 \left(H + M - N_d M\right) \Rightarrow \mu_r = \left(1 + \frac{M(1 - N_d)}{H}\right) \tag{5.1}$$

where M is the magnetization, N_d is the demagnetization factor. For longer seeds the demagnetization effects are smaller and therefore the permeability is higher than the standard seeds (Figure 4-8).

The optimized shell thickness was successfully obtained for TB and HT-only seeds. At 10 $\mathrm{kA\,m^{-1}}$ and 50 kHz, copper and gold can produce enough power with a thickness applicable for medical use. It is known that gold discharges the secondary electrons following irradiation, and acts as an electron affinity sensitizer which increases production of free radicals. This plays an important role in the chemical process of cell destruction after irradiation. Along with radiation sensitizing, gold is also biocompatible making it a great candidate for our purpose. Therefore the seeds used in the simulation had gold shells [168]. An alloy made of a combination of metals used in this study can also be used with proper thickness to reinforce the shell and protect the patient from radioactive material leakage.

Through COMSOL simulations we have shown that when the brachytherapy seeds are replaced with TB seeds, and HT seeds are placed in the empty locations in the needle in a real plan, the optimized seed design can generate sufficient power to raise and maintain the temperature of the PTV at 42 °C. Without additional HT seeds, the coverage was not enough due to the smaller size of the ferrite core within TB seeds especially at the presence of high blood perfusion regions. The sharpness of the Curie transition of the ferrite allowed the seeds to maintain power production at a sufficient rate, keeping the temperature constant while acting as a thermal regulator (Figure 4-19). The temperature within the seed arrangement rose above normal but rapidly fell off with distance. Therefore, the heat was contained within the local region where the heat application was intended and little to no toxicity was expected for normal tissue surrounding the prostate. It should be noted that even though we reached more than 90% volume coverage, the seed distribution that was used in the simulation was designed for radiation purposes and was not optimized for simultaneous delivery of brachytherapy and HT. Seeds implanted with the same needle in succession potentially increase the effective length, resulting in higher effective permeability. Our calculations indicate that in these instances, the relative power increases no more than ∼25% for an all-TB stack and ∼45% for the all-HT-only stack. This leads to enhanced thermal volume coverage of the prostate tissue compared to the conservative approach of treating seeds independently.

The calculated power was used as the heat source in the simulations. Another way this simulation could be carried out was by using the permeability of the ferrite as input values and directly solving for the eddy current generated by the seed through COMSOL Multiphysics modeling. The latter method is computationally much more expensive, and the same calculation for only one seed takes hours to finish. Using the power versus temperature model not only increases the efficiency significantly, but the obtained results only have a 2% deviation in temperature distribution compared to the direct simulation of Joule heat generated by seeds over a range of blood perfusion rates.

As indicated in the results, the temperature within the high blood perfusion regions does not increase to the same level as the low perfusion regions. It is known that hyperthermia at temperatures higher than 42.5 °C results in direct cell kill through necrosis, and mild hyperthermia (<42.5 °C) enhances the immune response and radiosensitivity of the tissue with minor direct cell kill through apoptosis. Therefore, we continue to get significant benefits from mild hyperthermia in the high blood perfusion regions. The above indicates that it will be more effective if we use more TB seeds in the high blood perfusion regions that are radiosensitized by mild HT to benefit more from a higher radiation dose. By using multimodality imaging methods, we can reveal the heterogeneity of blood perfusion rate in the prostate, decide whether TB, and HT-only seeds can provide the required power, plan the distribution of the seeds, and take the appropriate action at the time of planning a patient. Addition of more seeds to the arrangement for better heat coverage is also possible since the temperature can only raise up to the curie temperature and will not increase the overall temperature in an unlimited fashion. Another advantage of this method is that the process of designing seed distribution and seed insertion is already well-known and established. Physicians who have experience with brachytherapy seeds will find it easy to transition to using both TB and HT-only seeds in combination. This familiarity ensures a smooth adaptation to the new treatment approach, enhancing the comfort and confidence of healthcare professionals in implementing TB and HT therapies concurrently.

Even though the generated power can be further increased by increasing frequency (f), and magnetic field amplitude H_0 according to equation (2.73), the safety limit for SAR bounds us within a range of frequencies and magnetic field amplitudes. SAR safety limit states that the product of frequency and magnetic field amplitude should not exceed 5×10^8 A m^{-1} s^{-1} to keep the rise in tissue temperature in a range that does not cause any harmful physiological effects [99]. Therefore, to extract the maximum power, we compromise by reducing the frequency and increasing field amplitude since the power depends on H_0^2. On the other hand, frequency cannot be arbitrarily decreased, because frequencies lower than 50 kHz can cause nerve stimulation [99], which forces us to choose 50 kHz as the lower bound for frequency and 10 kA m^{-1} as higher bound for field amplitude to extract maximum power while SAR is in the safe range.

While the external magnetic field can be increased up to 10 kA m^{-1}, the field amplitude that reaches the seeds is attenuated by the tissue, and the field that reaches the core is attenuated both by tissue, and the shell. The amount by which the field decreases depends on the thickness of the layer, and the skin depth (δ) of the material. For tissue and prostate, the field is attenuated by about 4% reaching 96% of its initial amplitude for typical values provided in Section 4.3 before reaching the seed.

Thermal expansion of the seeds was also studied to ensure the structural integrity of the seeds and the safety of the patients. It was verified that the stress due to ferrite core strain in the temperature range 20 to 60 °C remains well within the tolerance limit, and there is no risk of radioactive material leakage.

Utilizing TB seeds, and HT-only seeds for treatment simultaneously causes more attenuation and scatter to the radiation, known as Interseed Scatter, and Attenuation (ISA) effect [169]. Gautam et al. showed that the presence of extra HT-only seeds in the plan and the ferrite core inside the TB seeds does not affect the radiation dose significantly, and it can be corrected by prescribing to isodoseline about 1.1 times that of desired prescription i.e. ISA effect will reduce the planned dose to the desired prescription dose. Our COMSOL simulations show that the magnetic field on the other hand remains more or less uniform in the region where the seeds are implanted and there will not be a shielding effect by outer seeds when the needles are separated by the typical brachytherapy separation of ∼1 cm [153].The dipole field created by the seeds in response to the magnetic field decays with distance r as $1/r^3$ and the effects remain local.

While HT can increase the Thermal Enhancement Ratio (TER) up to 5-fold, it should be noted that the TER for normal tissue also increases by the same amount. Normally the solution is to apply the modalities in sequence and taking advantage of slower loss of radiosensitivity of the cancerous cells. By increasing the interval between modalities TER of the cancerous tissue will be 2 compared to TER of 1 for normal tissue. However in this process the effectiveness of the radiation is compromised. TB seeds take advantage of highest TER possible by applying HT and radiation simultaneously while leaving the TER for normal tissue untouched because HT effects are confined within the tumor volume [120] (Figure 5-1).

Another factor that could affect HT treatment is thermotolerance. Thermotolerance is the result of the rapid production of HSPs which protect the cells and regulate

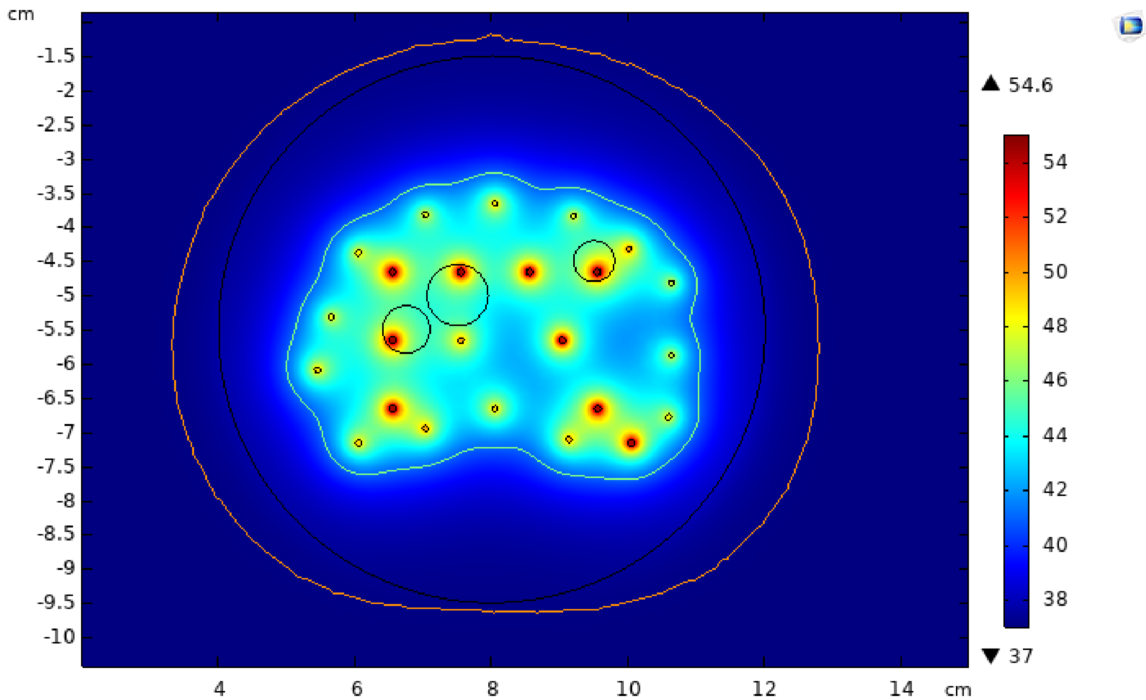

Figure 5-1: The temperature distribution inside the PTV with volumetric blood perfusion of 0.21 $\mathrm{mL\,g^{-1}\,min^{-1}}$. The area inside the cyan contour has temperatures above 42 °C and inside the orange contour the temperature is above 37.1 °C. As it can be seen from the figure the heat is contained within the PTV even when the volumetric blood perfusion is at its normal value.

homeostasis. The studies have shown, by choosing an appropriate interval between treatment sessions (ideally 48 to 72 hours) the thermotolerance effect of the HSPs will be dissipated [42, 56].

Chapter 6

Conclusion and Future Work

The ferrite core permeability was experimentally determined based on measured RL circuit parameters for a range of frequencies and magnetic field amplitudes relevant to the induction of magnetically mediated hyperthermia. The results were used to model seed implants consisting of a ferrite ceramic core and metal shell, optimizing the design both in terms of the material and the shell thickness for two configurations: TB and HT-only. While the TB seeds provided the ability to simultaneously deliver heat and radiation to the target, the HT-only seeds, placed in the empty spaces within already inserted implantation needles, served to increase the heat production and uniformity of the temperature distribution. The small size of the investigated ferrite core samples resulted in demagnetization significantly decreasing the relative permeability from its intrinsic value of $\sim$5000 to about 11. Despite such a drastic decrease, the power generated by the optimized TB and HT-only seeds was 45 mW and 267 mW respectively. The configuration of a clinical LDR brachytherapy plan, numerically simulated with the COMSOL Multiphysics package, was sufficient for hyperthermia coverage even in regions with high blood perfusion. The toxicity of the surrounding normal tissues was found to be minimal due to the rapid temperature fall off within a few millimeters distance from a seed.

Rapid Curie transition of the ferrite core facilitated heat self-regulation, eliminating most of the challenges of concurrent application of radiation and hyperthermia, such as logistics and invasive thermometry. We expect the current formulation of the ferrite material to be used for seed prototypes in animal studies and future clinical implementations [170].

The next step for this project involves studies of efficacy of TB vs. standard BEST Model 2301 seeds in animal tumor models:

- Detailed manufacturing specifications of the proposed seed
- Dosimetric verification of radiation properties of the TB seeds
- Comparing the the efficacy of the TB seeds to brachytherapy seeds

For the animal work the control group will be implanted with a conventional seed whereas the experimental group will be implanted with a thermobrachytherapy seed along with fiber optic temperature sensors. By verifying the location of the seeds before treatment and using their positions to plan radiation and hyperthermia treatments, the treatment outcome of the two groups can be compared for qualitative analysis of TB seed effects.

References

[1] **Siegel, R.L.**, **Miller, K.D.**, **Fuchs, H.E.** and **Jemal, A.**, 2022. "Cancer statistics, 2022. CA", *a cancer journal for clinicians*, **72**(1), 7-33.

[2] **Cooperberg, M.R., Hilton, J.F.**, and **Carroll, P.R.**, "The CAPRA-S score: a straightforward tool for improved prediction of outcomes after radical prostatectomy", *Cancer*, 2011, 117(22): p. 5039-5046.

[3] **Venturini NJ**, **Drake CG**, "Immunotherapy for prostate cancer", *Cold Spring Harbor Perspectives in Medicine*, 2019 May;**9**(5).

[4] **Dahiya, M.**, "Brachytherapy: A review", *J Crit Rev*, 2016. 3: p. 6-10.

[5] **Stish, B.J.**, et al., "Low dose rate prostate brachytherapy", *Translational andrology and urology*, 2018. 7(3): p. 341.

[6] **Jani, A.B.**, et al., "Biological effective dose for comparison and combination of external beam and low-dose rate interstitial brachytherapy prostate cancer treatment plans", *Medical Dosimetry*, 2004. 29(1): p. 42-48.

[7] **Wang, H.**, et al., "Cancer radiosensitizers", *Trends in pharmacological sciences*, 2018. 39(1): p. 24-48.

[8] **Citrin, D.E.**, "Radiation modifiers", *Hematology/Oncology Clinics*, 2019. 33(6): p. 1041-1055.

[9] **Bush, W.**, "Uber den Finfluss wetchen heftigere Eryspelen zuweilen auf organlsierte Neubildungen dusuben", *Verh Natruch Preuss Rhein Westphal*, 1886. 23: p. 28-30.

[10] **Westermark, F.**, "Uber die Behandlung des ulcerirenden Cervix carcinoma mittels Knonstanter Warme", *Zentralblatt für Gynäkologie*, 1898. 22: p. 1335-7.

[11] **Field, S.B.** and **J.W. Hand**, "An introduction to the practical aspects of clinical hyperthermia", 1990: *Taylor & Francis Group*.

[12] **Jones, E.**, et al., "Prospective thermal dosimetry: the key to hyperthermia's future", *International Journal of Hyperthermia*, 2006. 22(3): p. 247-253.

[13] **Masunaga, S.**, et al., "The usefulness of continuous administration of hypoxic cytotoxin combined with mild temperature hyperthermia with reference to effects on quiescent tumour cell populations", *International journal of hyperthermia*, 2005. 21(4): p. 305-318.

[14] **Song, C.W.**, "Effect of local hyperthermia on blood flow and microenvironment: a review", *Cancer research*, 1984. 44(10 Supplement): p. 4721s-4730s.

[15] **Yagawa, Y.**, et al., "Cancer immunity and therapy using hyperthermia with immunotherapy, radiotherapy, chemotherapy, and surgery", *Journal of Cancer Metastasis and Treatment*, 2017. 3: p. 218-230.

[16] **Pontiggia, P.**, et al., "The biological responses to heat", *Consensus on Hyperthermia for the 1990s*, 1990: p. 271-291.

[17] **Raaphorst, G.**, "Fudamental aspects of hyperthermic biology", *An introduction to the practical aspects of clinical hyperthermia*, 1990: p. 10-54.

[18] **Ahmed, K., Tabuchi, Y.**, and **Kondo, T.**, "Hyperthermia: an effective strategy to induce apoptosis in cancer cells", *Apoptosis*, 2015. 20(11): p. 1411-1419.

[19] **Habash, R.W.**, et al., “Thermal therapy, part 1: an introduction to thermal therapy”, *Critical Reviews in Biomedical Engineering*, 2006. 34(6).

[20] **Sardari, D.** and **N. Verga**, “Cancer treatment with hyperthermia”, 2011: *Citeseer.*

[21] **Boedtkjer E**, **Pedersen SF**, “The Acidic Tumor Microenvironment as a Driver of Cancer”, *Annu Rev Physiol.* 2020; 82:103-126.

[22] **Vaupel, P., F. Kallinowski**, and **P. Okunieff**, “Blood flow, oxygen and nutrient supply, and metabolic microenvironment of human tumors: a review”, *Cancer research*, 1989. 49(23): p. 6449-6465.

[23] **Gillies, R.J.**, et al., “Causes and effects of heterogeneous perfusion in tumors”, *Neoplasia*, 1999. 1(3): p. 197-207.

[24] **Dewhirst, M.**, et al., “The effect of rate of heating or cooling prior to heating on tumor and normal tissue microcirculatory blood flow”, *Biorheology*, 1984. 21(4): p. 539-558.

[25] **Datta, N.R.**, et al., “Integrating loco-regional hyperthermia into the current oncology practice: SWOT and TOWS analyses”, *Frontiers in oncology*, 2020. 10: p. 819.

[26] **Vaupel, P.W**. and **Kelleher, D.K.**, “Pathophysiological and vascular characteristics of tumours and their importance for hyperthermia: heterogeneity is the key issue”, *International Journal of Hyperthermia*, 2010. 26(3): p. 211-223.

[27] **Horsman, M.R.**, “Angiogenesis and vascular targeting: relevance for hyperthermia”, *International journal of hyperthermia*, 2008. 24(1): p. 57-65.

[28] **Hokland, S.** and **M. Horsman**, "The new vascular disrupting agent combretastatin-A1-disodium-phosphate (OXi4503) enhances tumour response to mild hyperthermia and thermoradiosensitization", *International journal of hyperthermia*, 2007. 23(7): p. 599-606.

[29] **Murata, R., J. Overgaard**, and **M.R. Horsman**, "Combretastatin A-4 disodium phosphate: a vascular targeting agent that improves that improves the anti-tumor effects of hyperthermia, radiation, and mild thermoradiotheraphy", *International Journal of Radiation Oncology Biology Physics*, 2001. 51(4): p. 1018-1024.

[30] **Horsman, M.R.**, "Tissue physiology and the response to heat", *International journal of hyperthermia*, 2006. 22(3): p. 197-203.

[31] **Horsman, M.**, et al., "Combretastatins novel vascular targeting drugs for improving anticancer therapy, in Angiogenesis", 2000, *Springer*. p. 311-323.

[32] **von Ardenne, M.**, "Selective multiphase cancer therapy: Conceptual aspects and experimental basis", *Advances in Pharmacology*, 1972. 10: p. 339-380.

[33] **Keech ML**, **Wills ED**, "The effect of hyperthermia on activation of lysosomal enzymes in HeLa cells", *European Journal of Cancer* (1965). 1979 Aug 1;15(8):1025-31.

[34] **Hinnen P.**, **Eskens FA.** Vascular disrupting agents in clinical development. British journal of cancer. 2007 Apr;96(8):1159-65.

[35] **Hokland, S.L.**, et al., "Imaging tumour physiology and vasculature to predict and assess response to heat", *International Journal of Hyperthermia*, 2010. 26(3): p. 264-272.

[36] **Gilkes, D.M., Semenza, G.L.**, and **Wirtz D.**, "Hypoxia and the extracellular matrix: drivers of tumour metastasis", *Nature Reviews Cancer*, 2014. 14(6): p. 430-439.

[37] **Overgaard, J.**, "Hypoxic radiosensitization: adored and ignored", *Journal of Clinical Oncology*, 2007. 25(26): p. 4066-4074.

[38] **Wong, R.S.**, "Apoptosis in cancer: from pathogenesis to treatment", *Journal of Experimental & Clinical Cancer Research*, 2011. 30(1): p. 1-14.

[39] **Plati, J., Bucur, O.**, and **Khosravi-Far R.**, "Apoptotic cell signaling in cancer progression and therapy", *Integrative biology*, 2011. 3(4): p. 279-296.

[40] **Lepock, J.R.**, "Cellular effects of hyperthermia: relevance to the minimum dose for thermal damage", *International journal of hyperthermia*, 2003. 19(3): p. 252-266.

[41] **Nguyen, H.T.**, et al., "Combined hyperthermia and chemotherapy as a synergistic anticancer treatment", *Journal of Pharmaceutical Investigation*, 2019. 49(5): p. 519-526.

[42] **Zhang, Y.** and **Calderwood S.K.**, "Autophagy, protein aggregation and hyperthermia: a mini-review", *International Journal of Hyperthermia*, 2011. 27(5): p. 409-414.

[43] **Dieing, A.**, et al., "The effect of induced hyperthermia on the immune system", *Progress in brain research*, 2007. 162: p. 137-152.

[44] **Schildkopf, P.**, et al., "Radiation combined with hyperthermia induces HSP70-dependent maturation of dendritic cells and release of pro-inflammatory cytokines by dendritic cells and macrophages", *Radiotherapy and Oncology*, 2011. 101(1): p. 109-115.

[45] **Chen, T.**, et al., “Heat shock protein 70, released from heat-stressed tumor cells, initiates antitumor immunity by inducing tumor cell chemokine production and activating dendritic cells via TLR4 pathway”, *The journal of immunology*, 2009. 182(3): p. 1449-1459.

[46] **Li, Z.**, et al., “Hyperthermia targeting the tumor microenvironment facilitates immune checkpoint inhibitors”, *Frontiers in Immunology*, 2020. 11.

[47] **Noessner, E.**, et al., “Tumor-derived heat shock protein 70 peptide complexes are cross-presented by human dendritic cells”, *The Journal of Immunology*, 2002. 169(10): p. 5424-5432.

[48] **Bethke, K.**, et al., “Different efficiency of heat shock proteins (HSP) to activate human monocytes and dendritic cells: superiority of HSP60”, *The journal of immunology*, 2002. 169(11): p. 6141-6148.

[49] **Breloer, M.**, et al., “Heat shock proteins as “danger signals”: eukaryotic Hsp60 enhances and accelerates antigen-specific IFN-γ production in T cells”, *European journal of immunology*, 2001. 31(7): p. 2051-2059.

[50] **Botzler, C.**, et al., “Definition of extracellular localized epitopes of Hsp70 involved in an NK immune response”, *Cell stress & chaperones*, 1998. 3(1): p. 6.

[51] **Toraya-Brown, S.** and **Fiering, S.**, “Local tumour hyperthermia as immunotherapy for metastatic cancer”, *International journal of hyperthermia*, 2014. 30(8): p. 531-539.

[52] **Lee, S.**,et al. “Immunogenic effect of hyperthermia on enhancing radiotherapeutic efficacy.”, *International journal of molecular sciences*, 2018, 19(9): p.2795.

[53] **Barros, F.M.**, et al., "Exosomes and immune response in cancer: friends or foes?", *Frontiers in immunology*, 2018. 9: p. 730.

[54] **Sharabi A.B.**, **Lim M.**, **DeWeese T.L.**, **Drake C.G.**, "Radiation and checkpoint blockade immunotherapy: Radiosensitisation and potential mechanisms of synergy." *Lancet Oncol.* 2015, 16: p. 498–e509.

[55] **Ianzini, M.M., F**, "Enhancement of radiation-induced mitotic catastrophe by moderate hyperthermia", *International journal of radiation biology*, 2000. 76(2): p. 273-280.

[56] **Hildebrandt, B.**, et al., "The cellular and molecular basis of hyperthermia", *Critical reviews in oncology/hematology*, 2002. 43(1): p. 33-56.

[57] **Wang, Y.**, et al., "Regulation of dna replication after heat shock by replication protein a-nucleolin interactions", *Journal of Biological Chemistry*, 2001. 276(23): p. 20579-20588.

[58] **Iliakis, G.**, et al., "Evidence for an S-phase checkpoint regulating DNA replication after heat shock: a review", *International journal of hyperthermia*, 2004. 20(2): p. 240-249.

[59] **Behrouzkia, Z.**, et al., "Hyperthermia: how can it be used?", *Oman medical journal*, 2016. 31(2): p. 89.

[60] **Wust, P.**, et al., "Hyperthermia in combined treatment of cancer", *The lancet oncology*, 2002. 3(8): p. 487-497.

[61] **Stauffer, P.R.**, "Thermal therapy techniques for skin and superficial tissue disease. in Matching the energy source to the clinical need: a critical review", 2000. *International Society for Optics and Photonics.*

[62] **Habash, R.W.**, et al., "Thermal therapy, part 2: hyperthermia techniques", *Critical Reviews in Biomedical Engineering*, 2006. 34(6).

[63] **Issels, R.**, et al., "Neoadjuvant chemotherapy combined with regional hyperthermia (RHT) for locally advanced primary or recurrent high-risk adult soft-tissue sarcomas (STS) of adults: long-term results of a phase II study", *European journal of cancer*, 2001. 37(13): p. 1599-1608.

[64] **Wiedemann, G.J.**, et al., "Ifosfamide and carboplatin combined with 41.8 °C whole-body hyperthermia in patients with refractory sarcoma and malignant teratoma", *Cancer research*, 1994. 54(20): p. 5346-5350.

[65] **Sethi, M.** and **Chakarvarti, S.**, "Hyperthermia techniques for cancer treatment: A review", *International Journal of PharmTech Research*, 2015. 8(6): p. 292-299.

[66] **Zhu, L.**, et al., "Ultrasound hyperthermia technology for radiosensitization", *Ultrasound in medicine & biology*, 2019. 45(5): p. 1025-1043.

[67] **Hijnen, N.M.**, et al., "Tumour hyperthermia and ablation in rats using a clinical MR-HIFU system equipped with a dedicated small animal set-up", *International journal of hyperthermia*, 2012. 28(2): p. 141-155.

[68] **Salgaonkar, V.A.**, et al., "Model-based feasibility assessment and evaluation of prostate hyperthermia with a commercial MR-guided endorectal HIFU ablation array", *Medical physics*, 2014. 41(3): p. 033301.

[69] **Phenix, C.P.**, et al., "High intensity focused ultrasound technology, its scope and applications in therapy and drug delivery", *Journal of Pharmacy & Pharmaceutical Sciences*, 2014. 17(1): p. 136-153.

[70] **Stuchly, M.A.**, "Interaction of radiofrequency and microwave radiation with living systems", *Radiation and environmental biophysics*, 1979. 16(1): p. 1-14.

[71] **Schwan, H.** and **Foster, K.**, "Microwave dielectric properties of tissue. Some comments on the rotational mobility of tissue water", *Biophysical journal*, 1977. 17(2): p. 193-197.

[72] **Ryan, T.P.** and **Brace, C.L.**, "Interstitial microwave treatment for cancer: historical basis and current techniques in antenna design and performance", *International Journal of Hyperthermia*, 2017. 33(1): p. 3-14.

[73] **Kim, K.S.** and **Lee, S.Y.**, "Nanoparticle-mediated radiofrequency capacitive hyperthermia: a phantom study with magnetic resonance thermometry", *International Journal of Hyperthermia*, 2015. 31(8): p. 831-839.

[74] **Kim, K.S.**, **Hernandez, D.**, and **Lee, S.Y.**, "Time-multiplexed two-channel capacitive radiofrequency hyperthermia with nanoparticle mediation", *Biomedical engineering online*, 2015. 14(1): p. 1-15.

[75] **Kim, J.H., Hahn, E.W.**, and **Antich, P.P.**, "Radiofrequency hyperthermia for clinical cancer therapy", *Natl Cancer Inst Monogr*, 1982. 61: p. 339-342.

[76] **Kuroda, S.**, et al., "Thermal distribution of radio-frequency inductive hyperthermia using an inductive aperture-type applicator: evaluation of the effect of tumour size and depth", *Medical & biological engineering & computing*, 1999. 37(3): p. 285-290.

[77] **Dutz, S.**, et al., "Hysteresis losses of magnetic nanoparticle powders in the single domain size range", *Journal of Magnetism and Magnetic Materials*, 2007. 308(2): p. 305-312.

[78] **Chang, D.**, et al., "Biologically targeted magnetic hyperthermia: potential and limitations", *Frontiers in pharmacology*, 2018. 9: p. 831.

[79] **De la Presa, P.**, et al., "Study of heating efficiency as a function of concentration, size, and applied field in γ-Fe2O3 nanoparticles", *The Journal of Physical Chemistry C*, 2012. 116(48): p. 25602-25610.

[80] **Deatsch, A.E.** and **Evans, B.A.**, "Heating efficiency in magnetic nanoparticle hyperthermia", *Journal of Magnetism and Magnetic Materials*, 2014. 354: p. 163-172.

[81] **Andrä, W.** and **Nowak, H.**, "Magnetism in medicine: a handbook", 2007: *John Wiley & Sons.*

[82] **Burton, C.**, **Hill, M.**, and **Walker, A.E.**, "The RF thermoseed-A thermally self-regulating implant for the production of brain lesions", *IEEE Transactions on Biomedical Engineering*, 1971(2): p. 104-109.

[83] **Brezovich, I.A.** and **Meredith, R.F.**, "Practical aspects of ferromagnetic thermoseed hyperthermia", *Radiologic Clinics of North America*, 1989. 27(3): p. 589-602.

[84] **Shimizu, T.** and **Matsui, M.**, "New magnetic implant material for interstitial hyperthermia", *Science and technology of advanced materials*, 2003. 4(5): p. 469.

[85] **Brezovich, I.A.**, **Atkinson, W.J**, and **Chakraborty, D.P.**, "Temperature distributions in tumor models heated by self-regulating nickel–copper alloy thermoseeds", *Medical Physics*, 1984. 11(2): p. 145-152.

[86] **Kaur, P.**, et al., "Hyperthermia using nanoparticles–promises and pitfalls", *International Journal of Hyperthermia*, 2016. 32(1): p. 76-88.

[87] **Sebastian Cabeza, V.**, et al., "Size-controlled flow synthesis of gold nanoparticles using a segmented flow microfluidic platform", *Langmuir*, 2012. 28(17): p. 7007-7013.

[88] **Pedrosa, P.**, et al., "Gold nanotheranostics: proof-of-concept or clinical tool?", *Nanomaterials*, 2015. 5(4): p. 1853-1879.

[89] **Palanisamy, S.** and **Wang, Y.M**, "Superparamagnetic iron oxide nanoparticulate system: synthesis, targeting, drug delivery and therapy in cancer", *Dalton transactions*, 2019. 48(26): p. 9490-9515.

[90] **Pollert, E.**, et al., "Search of new core materials for magnetic fluid hyperthermia: preliminary chemical and physical issues", *Progress in Solid State Chemistry*, 2009. 37(1): p. 1-14.

[91] **Sapareto, S.A.** and **Dewey, W.C.**, "Thermal dose determination in cancer therapy", *International Journal of Radiation Oncology Biology Physics*, 1984. 10(6): p. 787-800.

[92] **Kroesen, M.**, et al., "Confirmation of thermal dose as a predictor of local control in cervical carcinoma patients treated with state-of-the-art radiation therapy and hyperthermia", *Radiotherapy and oncology*, 2019. 140: p. 150-158.

[93] **Streffer, C.**, "Biological basis of thermotherapy (with special reference to oncology), in Biological basis of oncologic thermotherapy", 1990, *Springer*. p. 1-71.

[94] **Dewey, W.C.**, **Thrall, D.E.**, and **Gillette, E.L.**, "Hyperthermia and radiation—a selective thermal effect on chronically hypoxic tumor cells in vivo", *International Journal of Radiation Oncology Biology Physics*, 1977. 2(1-2): p. 99-103.

[95] **Gabriel, C.**, **Peyman, A.**, and **Grant, E.H**, "Electrical conductivity of tissue at frequencies below 1 MHz", *Physics in medicine & biology*, 2009. 54(16): p. 4863.

[96] **Liu, X.**, et al., "Conductivity and frequency dependent specific absorption rate", *Journal of Applied Physics*, 2013. 113(7): p. 074902.

[97] **Gabriel, S.**, **Lau, R.**, and **Gabriel, C.**, "The dielectric properties of biological tissues: II. Measurements in the frequency range 10 Hz to 20 GHz", *Physics in medicine & biology*, 1996. 41(11): p. 2251.

[98] **U.S. Food and Drug Administration**, "Criteria for Significant Risk Investigations of Magnetic Resonance Diagnostic Devices - Guidance for Industry and Food and Drug Administration Staff" FDA, Uun. 2014, Docket Number: FDA-2020-D-0957.

[99] **Atkinson, W.J.**, **Brezovich, I.A.**, and **Chakraborty, D.P.**, "Usable frequencies in hyperthermia with thermal seeds", *IEEE Transactions on Biomedical Engineering*, 1984(1): p. 70-75.

[100] **Sovilj, S.**, et al., "Simplified 2D bidomain model of whole heart electrical activity and ECG generation", *Measurement Science Review*, 2014. 14(3): p. 136.

[101] **Mcintosh, R.L.** and **Anderson, V.**, "A comprehensive tissue properties database provided for the thermal assessment of a human at rest", *Biophysical Reviews and Letters*, 2010. 5(03): p. 129-151.

[102] **Hua, Y.**, et al., "Intracavity hyperthermia in nasopharyngeal cancer: a phase III clinical study", *International Journal of Hyperthermia*, 2011. 27(2): p. 180-186.

[103] **Huilgol, N.G.**, **Gupta, S.**, and **Sridhar, C.**, "Hyperthermia with radiation in the treatment of locally advanced head and neck cancer: a report of randomized trial", *Journal of cancer research and therapeutics*, 2010. 6(4): p. 492.

[104] **Franckena, M.**, et al., "Long-term improvement in treatment outcome after radiotherapy and hyperthermia in locoregionally advanced cervix cancer: an update of the Dutch Deep Hyperthermia Trial", **International Journal of Radiation Oncology Biology Physics**, 2008. 70(4): p. 1176-1182.

[105] **Hong-Wei, C.**, "A randomized trial of hyperthermia-radiochemotherapy for uterine cervix cancer", *Clin J Clin Oncol*, 1997. 24: p. 249-251.

[106] **Zolciak-Siwinska, A.**, et al., "HDR brachytherapy combined with interstitial hyperthermia in locally advanced cervical cancer patients initially treated with concomitant radiochemotherapy–a phase III study", *Radiotherapy and Oncology*, 2013. 109(2): p. 194-199.

[107] **Algan, Ö.**, et al., "External beam radiotherapy and hyperthermia in the treatment of patients with locally advanced prostate carcinoma: Results of long term follow-up", *Cancer: Interdisciplinary International Journal of the American Cancer Society*, 2000. 89(2): p. 399-403.

[108] **van der Zee, J.**, et al., "Comparison of radiotherapy alone with radiotherapy plus hyperthermia in locally advanced pelvic tumours: a prospective, randomised, multicentre trial", *The Lancet*, 2000. 355(9210): p. 1119-1125.

[109] **Amichetti, M.**, et al., "Cisplatin, hyperthermia, and radiation (trimodal therapy) in patients with locally advanced head and neck tumors: A phase I–II study", *International Journal of Radiation Oncology Biology Physics*, 1993. 26(5): p. 801-807.

[110] **Issels, R.D.**, et al., "Effect of neoadjuvant chemotherapy plus regional hyperthermia on long-term outcomes among patients with localized high-risk soft tissue sarcoma: the EORTC 62961-ESHO 95 randomized clinical trial", *JAMA oncology*, 2018. 4(4): p. 483-492.

[111] **Oldenborg, S.**, et al., "Reirradiation + hyperthermia for recurrent breast cancer en cuirasse", *Strahlentherapie und Onkologie*, 2018. 194(3): p. 206-214.

[112] **Notter, M.**, **Piazena, H.**, and **Vaupel, P.**, "Hypofractionated re-irradiation of large-sized recurrent breast cancer with thermography-controlled, contact-free water-filtered infra-red-A hyperthermia: a retrospective study of 73 patients", *International Journal of Hyperthermia*, 2017. 33(2): p. 227-236.

[113] **De-Colle, C.**, et al., "Hyperthermic chest wall re-irradiation in recurrent breast cancer: a prospective observational study", *Strahlentherapie und Onkologie*, 2019. 195(4): p. 318-326.

[114] **Datta, N.R.**, et al., "Hyperthermia and radiotherapy in the management of head and neck cancers: A systematic review and meta-analysis", *International Journal of Hyperthermia*, 2016. 32(1): p. 31-40.

[115] **Kok, H.**, et al., "Feasibility of on-line temperature-based hyperthermia treatment planning to improve tumour temperatures during locoregional hyperthermia", *International Journal of Hyperthermia*, 2018. 34(7): p. 1082-1091.

[116] **Mulder, H.T.**, et al., "Systematic quality assurance of the BSD2000-3D MR-compatible hyperthermia applicator performance using MR temperature imaging", *International Journal of Hyperthermia*, 2018. 35(1): p. 305-313.

[117] **Datta, N.**, et al., "Local hyperthermia combined with radiotherapy and-/or

chemotherapy: Recent advances and promises for the future", *Cancer treatment reviews*, 2015. 41(9): p. 742-753.

[118] **Qin, W.**, et al., "Modulated electro-hyperthermia enhances dendritic cell therapy through an abscopal effect in mice", *Oncology Reports*, 2014. 32(6): p. 2373-2379.

[119] **Elming, P.B.**, et al., "Hyperthermia: the optimal treatment to overcome radiation resistant hypoxia", *Cancers*, 2019. 11(1): p. 60.

[120] **Overgaard, J.**, "Influence of sequence and interval on the biological response to combined hyperthermia and radiation", *Natl Cancer Inst Monogr*, 1982. 61: p. 325-332.

[121] **Van Leeuwen, C.**, et al., "3D radiobiological evaluation of combined radiotherapy and hyperthermia treatments", *International Journal of Hyperthermia*, 2017. 33(2): p. 160-169.

[122] **Kok, H.P.**, et al., "Quantifying the combined effect of radiation therapy and hyperthermia in terms of equivalent dose distributions", *International Journal of Radiation Oncology Biology Physics*, 2014. 88(3): p. 739-745.

[123] **Biau J**, **Chautard E**, **Verrelle P**, **Dutreix M**, "Altering DNA repair to improve radiation therapy: specific and multiple pathway targeting", *Frontiers in oncology*, 2019;9:1009.

[124] **Dietlein, F.**, **Thelen, L.**, and **Reinhardt, H.C.**, "Cancer-specific defects in DNA repair pathways as targets for personalized therapeutic approaches", *Trends in genetics*, 2014. 30(8): p. 326-339.

[125] **Krajewska, M.**, et al., "Regulators of homologous recombination repair as novel targets for cancer treatment", *Frontiers in genetics*, 2015. 6: p. 96.

[126] **Iliakis, G.**, **Murmann, T.**, and **Soni, A.**, "Alternative end-joining repair pathways are the ultimate backup for abrogated classical non-homologous end-joining and homologous recombination repair: Implications for the formation of chromosome translocations", *Mutation Research/Genetic Toxicology and Environmental Mutagenesis*, 2015. 793: p. 166-175.

[127] **Krawczyk, P.M.**, et al., "Mild hyperthermia inhibits homologous recombination, induces BRCA2 degradation, and sensitizes cancer cells to poly (ADP-ribose) polymerase-1 inhibition", *Proceedings of the National Academy of Sciences*, 2011. 108(24): p. 9851-9856.

[128] **van Rhoon, G.C.**, "Is CEM43 still a relevant thermal dose parameter for hyperthermia treatment monitoring?", *International Journal of Hyperthermia*, 2016. 32(1): p. 50-62.

[129] **Peeken J.C.**, **Vaupel P.**, **Combs S.E.**, "Integrating Hyperthermia into Modern Radiation Oncology: What Evidence Is Necessary?" *Front Oncol.* 2017 Jun 30;7:132. doi: 10.3389/fonc.2017.00132.

[130] **Cihoric, N.**, et al., "Hyperthermia-related clinical trials on cancer treatment within the ClinicalTrials. gov registry", *International journal of hyperthermia*, 2015. 31(6): p. 609-614.

[131] **Thiesen, B.** and **Jordan, A.**, "Clinical applications of magnetic nanoparticles for hyperthermia", *International journal of hyperthermia*, 2008. 24(6): p. 467-474.

[132] **Pinto, A.**, **Eveno, C.**, and **Pocard, M.**, "Update on clinical trials in colorectal cancer peritoneal metastasis", *International Journal of Hyperthermia*, 2017. 33(5): p. 543-547.

[133] **Bostwick, D.G.**, et al., "Prostate specific membrane antigen expression in prostatic intraepithelial neoplasia and adenocarcinoma: a study of 184 cases", *Cancer: Interdisciplinary International Journal of the American Cancer Society*, 1998. 82(11): p. 2256-2261.

[134] **Hofman, M.S.**, et al., "Prostate-specific membrane antigen PET: clinical utility in prostate cancer, normal patterns, pearls, and pitfalls", *Radiographics*, 2018. 38(1): p. 200-217.

[135] **Fendler, W.P.**, et al., "Assessment of 68Ga-PSMA-11 PET accuracy in localizing recurrent prostate cancer: a prospective single-arm clinical trial", *JAMA oncology*, 2019. 5(6): p. 856-863.

[136] **Eiber, M.**, et al., "Simultaneous 68Ga-PSMA HBED-CC PET/MRI improves the localization of primary prostate cancer", *European urology*, 2016. 70(5): p. 829-836.

[137] **Woo, S.**, et al., "Prostate-specific membrane antigen positron emission tomography (PSMA-PET) for local staging of prostate cancer: a systematic review and meta-analysis", *European Journal of Hybrid Imaging*, 2020. 4(1): p. 1-15.

[138] **Perera, M.**, et al., Gallium-68 prostate-specific membrane antigen positron emission tomography in advanced prostate cancer—updated diagnostic utility, sensitivity, specificity, and distribution of prostate-specific membrane antigen-avid lesions: a systematic review and meta-analysis", *European urology*, 2020. 77(4): p. 403-417.

[139] **Thakur, P.**, et al., "A review on MnZn ferrites: Synthesis, characterization and applications", *Ceramics international*, 2020. 46(10): p. 15740-15763.

[140] **Knight, D. W.**, "Practical continuous functions for the internal impedance of solid cylindrical conductors", *G3YNH info* (2013).

[141] **Medhurst, R. G.**, "HF resistance and self-capacitance of single-layer solenoids", *Wireless Engineer* 24 (1947).

[142] **Rosa, E.B.**, "Calculation of the self-inductance of single-layer coils", *No. 31. US Government Printing Office*, 1906.

[143] **Nagaoka, H.**, "The inductance coefficients of solenoids", *The journal of the College of Science*, Imperial University of Tokyo, Japan 27 (1909): 1-33.

[144] **Snelling, E.**, "Soft Ferrites-Properties and Applications", 1969: CRC Press, Cleveland, OH

[145] **Cochran, J.F.** and **Heinrich, B.**, 2020, "Applications of maxwell's equations".

[146] **Chen, D.X.**, **Pardo, E.** and **Sanchez, A.**, 2006. "Fluxmetric and magnetometric demagnetizing factors for cylinders", *Journal of Magnetism and Magnetic Materials*, 306(1), p.135-146.

[147] **Chen, D.X.**, **Brug, J.A.** and **Goldfarb, R.B.**, 1991 "Demagnetizing factors for cylinders", *IEEE Transactions on magnetics*, 27(4), p.3601-3619.

[148] **Davies, J.**, **Simpson, P.**, "Induction Heating Handbook", *London: McGraw-Hill*, 1979. Print.

[149] **Paulus, J.A.**, et al., "Evaluation of Inductively Heated Ferromagnetic Alloy Implants for Therapeutic Interstitial Hyperthermia", 1996 *IEEE Trans. Biomed. Eng.* 43, p. 406-413.

[150] **Cetas, T.C.**, **Gross, E.J.** and **Contractor, Y.**, 1998. A ferrite core/metallic sheath thermoseed for interstitial thermal therapies. IEEE transactions on biomedical engineering, 45(1), p.68-77.

[151] **McAdams, W.H.**, 11Heat Transmission", New York: McGraw-Hill, 1954. Print.

[152] **Pennes H.H.** "Analysis of Tissue and Arterial Blood Temperatures in the Resting Human Forearm," J. Appl. Physiol. 1, 93-122 (1948).

[153] **Crook JM**, **Haie-Meder C**, **Demanes DJ**, **Mazeron JJ**, **Martinez AA**, and **Rivard MJ** American brachytherapy society–groupe Européen de Curiethérapie–European society of therapeutic radiation Oncology (ABS-GEC-ESTRO) consensus statement for penile brachytherapy. *Brachytherapy* 2013; 12(3):191-8. doi: 10.1016/j.brachy.2013.01.167.

[154] **Griffiths DJ**, "Introduction to Electrodynamics", Boston: Pearson, 1999.

[155] **Yadav S.**, "Determination of thermal conductivity of tissue mimicking gel", Doctoral dissertation.

[156] **Warrell G.R.**, "Computational and experimental evaluations of a novel thermo-brachytherapy seed for treatment of solid tumors", Doctoral dissertation, University of Toledo.

[157] **Vaupel, P.** and **Kelleher, D.K.**, "Blood flow and oxygenation status of prostate cancers", *Oxygen Transport to Tissue XXXIV*, 2013: 299-305.

[158] **Franiel, T.**, et al., "Prostate MR imaging: tissue characterization with pharmacokinetic volume and blood flow parameters and correlation with histologic parameters", *Radiology*, 2009 252(1): 101-108.

[159] **Ward MR**, "Electrical Engineering Science",. McGraw-Hill 1971: 36–40.

[160] **Gabriel S**, **Lau RW**, **Gabriel C.** "The dielectric properties of biological tissues: III. Parametric models for the dielectric spectrum of tissues", *Phys. Med. Biol.* 1996; 41:2271. doi: 10.1088/0031-9155/41/11/003.

[161] **Froes, FH**, ed. "Titanium: physical metallurgy, processing, and applications", ASM international, 2015.

[162] **Macintosh, R.L.**, and **Anderson, V.** " A comprehensive tissue properties database provided for the thermal assessment of a human at rest", *Biophysical Reviews and Letters*, 2010, 5(3): 129-151.

[163] **Duck A.** , "Physical Properties of Tissue: A Comprehensive Reference Book", (IPEM, York, 1990).

[164] **Hasgall, A.**, et al. , "IT'IS Database for thermal and electromagnetic parameters of biological tissues", *IT'IS Foundation*, 1 September 2015.

[165] **Giering K.** , et al., "Determination of the specific heat capacity of healthy and tumorous human tissue", *Thermochim. Acta* 251, 199–205 (1995).

[166] **Boyer, R.**, **Welsch, G.**, and **Collings E. W.**, "Materials Properties Handbook", (ASM International, Materials Park, OH, 1994).

[167] **Serway, R.A.**, **Jewett, J.W.**, "Principles of physics", 1998, 1 Saunders College Pub. Fort Worth, TX.

[168] **Gong L.**, et al., "Application of Radiosensitizers in Cancer Radiotherapy", *Int Journal of Nanomedicine* 2021 16: 1083.

[169] **Gautam, B.**, **Parsai, E.I.**, **Shvydka, D.**, **Feldmeier, J.**, **Subramanian, M.**, "Dosimetric and thermal properties of a newly developed thermobrachytherapy seed with ferromagnetic core for treatment of solid tumors", *Medical Physics* 2012 39(14): 1980-1990.

[170] **Taghizadeh S**, **Shvydka D**, **Shan A**, **Mian OY**, and **Parsai EI**, "Optimization and experimental characterization of the innovative thermo-brachytherapy seed for prostate cancer treatment", *Medical Physics*, 2024 Feb; 51(2): 839-53.

Appendix A

Algorithms Used for Data Acquisition and Processing

Code for connection to the oscilloscope is provided below

```
import numpy as np
from struct import unpack
import pyvisa as visa # For connection to instrument

class Oscilloscope():
    def __init__(self, frequency: int, plot: bool = False):
        self.frequency = frequency
        self.plot_flag = plot
        self.scope = self._connect()

    def _connect(self):
        """
        Finding the oscilloscope and connecting to it.
        """
        # Open session to instrument
        rm = visa.ResourceManager('@py')
        SERIAL = "C050688"
        resource=[r for r in rm.list_resources() if SERIAL in r][0]
```

```
        lib = rm.visalib
        return rm.open_resource(resource)

    def _setup_channel_one(self, scope):
        """
        Setting channel one parameters
        """
        scope.write('DATA:SOU CH1')
        scope.write('DATA:WIDTH 1')
        scope.write('DATA:ENC RPB')

    def _setup_channel_two(self, scope):
        """
        Setting channel two parameters
        """
        scope.write('DATA:SOU CH2')
        scope.write('DATA:WIDTH 1')
        scope.write('DATA:ENC RPB')

    def _get_parameters(self, scope):
        """
        Obtaining the scales on the oscilloscope.
        """
        # obtaining the multiple
        self.ymult = float(scope.query('WFMPRE:YMULT?'))
        # obtaining the shift (yellow arrow)
        self.yzero = float(scope.query('WFMPRE:YZERO?'))
        # obtaining the y offset signal offset
        self.yoff = float(scope.query('WFMPRE:YOFF?'))
        # finding the x increment
        self.xincr = float(scope.query('WFMPRE:XINCR?'))
```

```
    def _read(self, scope):
        """
        Reading data stream from oscilloscope
        """
        scope.write('CURVE?')
        # reading the raw data
        data = scope.read_raw()
        # separating the header
        headerlen = 2+int(data[1])
        header = data[:headerlen]
        # data without the header
        ADC_wave = data[headerlen:-1]
        # decoding the data
        ADC_wave = np.array(unpack('%sB' %len(ADC_wave), ADC_wave))
        # getting the voltage data from channel one
        volts = (ADC_wave-self.yoff)*self.ymult+self.yzero
        time = np.arange(0, self.xincr*len(volts), self.xincr)
        return volts, time

    def _close(self, scope):
        """
        Closing the connection
        """
        scope.close()
        return

    def process(self):
        """
        Controling the process
        """
        scope = self.scope
        # set up channel one and extract vales
```

```
        self._setup_channel_one(scope)
        self._get_parameters(scope)
        volts_ch1, time_ch1 = self._read(scope)

        # set up channel two and extract values
        self._setup_channel_two(scope)
        self._get_parameters(scope)
        volts_ch2, time_ch2 = self._read(scope)

        return volts_ch1, time_ch1, volts_ch2, time_ch2
```

The following code is used to connect to the Omega thermocouple

```
import minimalmodbus

MODES = {
    'ascii' : minimalmodbus.MODE_ASCII,
    'rtu'   : minimalmodbus.MODE_RTU
}

PARITY = {
    'even'  : minimalmodbus.serial.PARITY_EVEN,
    'odd'   : minimalmodbus.serial.PARITY_ODD,
    'none'  : minimalmodbus.serial.PARITY_NONE
}

class TemperatureController():
    def __init__(self,
          port: str = '/dev/cu.usbserial-AB0OJ47K',
          mode: str = 'ascii', address: int = 1):
        self.port = port
        self.mode = MODES[mode]
        self.address = 1
```

```
def setup(self, baudrate: int = 9600,
     bytesize: int = 8, parity: str = 'even',
     stopbits: int = 1, timeout: int = 1):
    """
    Connecting to the thermocouple
    """
    self.instrument = minimalmodbus.Instrument(self.port, 1,
                                  self.mode) #debug = True
    self.instrument.serial.baudrate = baudrate
    self.instrument.serial.bytesize = bytesize
    self.instrument.serial.parity = PARITY[parity]
    self.instrument.serial.stopbits = stopbits
    self.instrument.serial.timeout = timeout
    # Good practice
    self.instrument.close_port_after_each_call = True
    self.instrument.clear_buffers_before_each_transaction = True

def read(self):
    """
    Reading from the thermocouple
    """
    return self.instrument.read_register(0x1000)/10

def set(self, temperature: float, decimals: int = 1):
    """
    Setting the desired temperature in case using thermocouple
    as temperature regulator
    """
    self.instrument.write_register(0x1001, temperature, decimals
                                  )
```

The following code is used for connecting to the Keithley sourcemeter which controls the voltage across the incandescent light bulb and changes the temperature

```
import pyvisa as visa

class SourceMeter():

    def __init__(self):
        self.current_voltage_a = 0.5
        self.current_voltage_b = 0.5

    def _connect(self, host:str = "192.168.0.55", port:str = "5025")
                                                :
        """
        connect to the keithly source meter through TCPIP
        """
        rm = visa.ResourceManager('@py')
        self.source_meter =  rm.open_resource(f'TCPIP::{host}::{port
                                                    }::SOCKET')

    def initialize(self, **kwargs):
        """
        Initializing the connection to the sourcemeter
        """
        self._connect(**kwargs)
        # setting the current limit
        self.source_meter.write("smua.source.limiti=1.5")
        self.source_meter.write("smub.source.limiti=1.5")
        # setting the voltage
        self.source_meter.write("smua.source.levelv=0.5")
        self.source_meter.write("smub.source.levelv=0.5")
        # turning the output on
        self.source_meter.write("smua.source.output=smua.OUTPUT_ON")
```

```
        self.source_meter.write("smub.source.output=smub.OUTPUT_ON")
        self.source_meter.write("beeper.enable=beeper.ON")
        self.source_meter.write("beeper.beep(1, 1200)")

    def increment(self, increment:float=0.5):
        """
        increamenting the output voltage of the sourcemeter
        """
        # if we have not reached channel a limit increment channel a
                                                 we increment voltage in
                                                channel a
        if self.current_voltage_a < 20:
            self.current_voltage_a += increment
            self.source_meter.write(f"smua.source.levelv={self.
                                                     current_voltage_a}")
        # if channel a limit is reached but channel b limit is not
                                                reached increment voltage
                                                in channel b
        elif self.current_voltage_b < 20:
            self.current_voltage_b += increment
            self.source_meter.write(f"smub.source.levelv={self.
                                                     current_voltage_b}")
        # if both limits are reached
        else:
            print('instrument limit reached!!!!')

    def disconnect(self):
        """Disconnecting from the sourcemeter"""
        self._close()

    def _close(self):
        """Closing the connection to the sourcemeter"""
```

```
        # turning the output on
        self.source_meter.write("smua.source.output=smua.OUTPUT_OFF"
                                            )
        self.source_meter.write("smub.source.output=smub.OUTPUT_OFF"
                                            )
        self.source_meter.close()
```

The process of data acquisition was orchestrated by the following

```
from lib.oscilloscope.oscilloscope import Oscilloscope
from lib.temperature_controller.temperature_controller import
                                  TemperatureController
from lib.sourcemeter.sourcemeter import SourceMeter
import argparse
from datetime import datetime as dt
import time
import os


def sleep_time(epsilon):
    '''
    for pause between two measurements
    epsilon : difference between tempetratures
    '''
    if epsilon > 0.1:
        return 120
    return 90


class Bucket():
    def __init__(self, path):
        self.path = path
        self.locations = {"input": ["voltage", "time"], "output": ["
                                            voltage", "time"]}
        self.file_name_suffix = None
```

```
    def initiate_files(self, v_initial, frequency, date):
        self.file_name_suffix = f'{v_initial}_{frequency}_{date}.csv
                                        '
        for key, value in self.locations.items():
            for kind in value:
                file_name = f'{kind}_{self.file_name_suffix}'
                with open(os.path.join(self.path, key, file_name), '
                                                  w') as file:
                    file.write(f'set_temperature,temperature,
                                                     resistance,
                                                     turns,
                                                     core_type,dt,{
                                                     kind}\n')

    def write(self, input_type, file_type, *values):
        first_columns = ','.join(str(value) for value in values[:-1]
                                        )
        last_column = '"[{}]"'.format(','.join(str(value) for value
                                        in values[-1]))
        all_columns = ','.join([first_columns,last_column])
        with open(os.path.join(self.path, input_type, f'{file_type}_
                                        {self.file_name_suffix}'),
                                         'a') as file:
            file.write(all_columns+'\n')
        return

parser = argparse.ArgumentParser(description = 'parsing input
                                 parameters')
parser.add_argument('-f', dest = 'frequency', type = int, help = '
                                 frequency of oscilloscope.')
parser.add_argument('-t', dest = 'turns', type = int, help = 'turns
```

```
                                   of solenoid')
parser.add_argument('-i', dest = 'increment', type = float, help = '
                                   the amount to increment the source
                                    meter voltage.')
parser.add_argument('-r', dest = 'resistance', type = float, help =
                                   'the resistance in the circuit')
parser.add_argument('-c', dest = 'core', type = int, help = 'the
                                   type of core inside')
parser.add_argument('--vac', dest='vacuum' )

args = parser.parse_args()
vacuum = args.vacuum
bucket = Bucket(path = './buckets/ferrite_archive/raw/' if not
                                   vacuum else './buckets/
                                   vacuum_archive/raw/')

oscilloscope = Oscilloscope( frequency = args.frequency or 100000 )
sourcemeter = SourceMeter()
sourcemeter.initialize()
controller = TemperatureController()
controller.setup()

slp = 90

# tolerance for changing temperature
current_temp = controller.read()

# timestamp to use in the name of the file
today = dt.strftime(dt.now(), "%Y-%m-%dT%H:%M:%S")

# initial values
input_voltage, input_time_axis, output_voltage, output_time_axis =
```

```
                                   oscilloscope.process()
input_peak2peak, phase = oscilloscope.fit(input_voltage,
                                   input_time_axis)
initial_peak2peak = f'{input_peak2peak:.2f}'

# setting up the headers in the file
bucket.initiate_files(initial_peak2peak, args.frequency, today)

# pause to get the correct values for inital temperature
time.sleep(slp)
counter = 0

while current_temp < 70:

    if counter == 15:
        sourcemeter.increment()
        time.sleep(30)
        counter = 0

    counter += 1
    current_temp = controller.read()
    bucket.write('input', 'voltage', *(current_temp, current_temp,
                                       args.resistance, args.turns,
                                       args.core, 2e-8, input_voltage
                                       ))
    bucket.write('output', 'voltage', *(current_temp, current_temp,
                                       args.resistance, args.turns,
                                       args.core, 2e-8,
                                       output_voltage))

    try:
        input_voltage, input_time_axis, output_voltage,
```

```
                                                     output_time_axis =
                                                     oscilloscope.process()
        dt1 = input_time_axis[1]-input_time_axis[0]
        dt2 = output_time_axis[1]-output_time_axis[0]
    except:
        oscilloscope = Oscilloscope( frequency = args.frequency or
                                                     100000 )
        input_voltage, input_time_axis, output_voltage,
                                                     output_time_axis =
                                                     oscilloscope.process()
        dt1 = input_time_axis[1]-input_time_axis[0]
        dt2 = output_time_axis[1]-output_time_axis[0]


    print(f'\rtemperature: {current_temp}, counting: {counter}', end
                                                 = '')
    time.sleep(10)
```

Processing the data and calculating different components of the circuit is calculated by using the following code and utility functions

```
def integrate(voltage: np.array, dt: float, diameter: float,
       turns: int, time: np.array=None, y=0):
    """
    This is the function that integrates over the voltage to
    find the magnetic flux
    B = 1/(NA) \int V dt
    """
    l = len(voltage)
    coef = (turns*np.pi*diameter**2/4)
    if time is not None:
        # if time vector is given
        magnetic_flux = [simpson(voltage[:i+1], time[:i+1])+y for i
```

```
                                                    in range(l)]
    else:
        # if the time spacing between the points are given
        magnetic_flux = [simpson(voltage[:i+1], None, dt)+y for i in
                                                    range(l)]
    return np.array(magnetic_flux)/coef



def field(current: np.array, turns: int, length: float):
    """
    This function calculatest the magnetic field using current
    """
    magnetic_field = turns/length*current
    return magnetic_field

def flux(voltage: np.array, dt: float, diameter: float,
    turns: int, time: np.array = None, y=0):
    """
    This function calculates the magnetic flux.
    """
    return integrate(voltage, dt, diameter, turns, time, y=0)

def sine_func(wt, a, phi, c):
    return a*np.sin(wt+phi)+c



def simple_circuit(x: list, v_real: float, v_im: float,
                   R: float, w: float) -> list:
    """
    This function is the circuit equations in the case when the
                                         oscilloscope capacitance and
                                         resistance are not taken into
```

```
                                                    account. or when Ro -> \infty
                                                    and co->0. Here they are
                                                    provided as input so we can
                                                    easily switch between
                                                    fucntions without changing the
                                                     codes
    """
    return [
        (x[0]*(R+x[0])+w**2*x[1]**2)/((R+x[0])**2+(w*x[1])**2)-
                                                           v_real,
        (R*w*x[1])/((R+x[0])**2+(w*x[1])**2)-v_im
    ]


def linear(x, a, b):
    """
    This is a linear funciton with x as argument, a as slope and b
                                                    as intercept
    """
    return a*x+b
```

```
class Wire():
    """
    This is a wire class that will capture all of the properties of
                                                    the wire that was used in the
                                                    circuit.
    """
    def __init__(self, diameter: float, length: float = 0, material:
                                                     str = "copper") -> None:
        self.diameter = diameter
        self.length = length
        self.area = np.pi*diameter**2/4
        self.material = material
```

```
    def get_resistance(self):
        self.resistance = MATERIALS.get(self.material).get("
                                                resistivity")*self.length/
                                                self.area
        return self.resistance

class Coil():
    """
    This is a coil class that will contain all the information about
                                                the coil
    """
    def __init__(self, turns: int = 16, winding: Wire = Wire(0.
                                                000254), lead: Wire = Wire(0.
                                                000254, length=0.16)):
        self.turns = turns
        self.diameter, self.length = [(coil["diameter"], coil["
                                                length"]) for coil in
                                                COIL_PROPERTIES if coil["
                                                turns"] == self.turns][0]
        self.winding = winding
        self.winding.length = np.sqrt(self.length**2+(np.pi*self.
                                                diameter*self.turns)**2)
        self.lead = lead
        self.resistance = self.lead.get_resistance() + self.winding.
                                                get_resistance()
        self.area = np.pi*self.diameter**2/4
```

```
class Circuit():
    def __init__(self, file: str, turns: int = None,
        parasitic:float = 0, diameter: float = None, length: float =
                                                None,
        lead: float = None, coil_loss: float = 0,
```

```
                                        equivalent_vacuum_file:
                                        str = "", vacuum: bool =
                                        False):
    """
    Initializing the Circuit object and do some initial data
                                        processing that will be
                                        used later.

    Args:
        measurement_df (DataFrame)  : The data frame containing
                                          the measurement data
        turns (int)                 : Number of coil turns
        parasitic (float)           : The parasitic inductance
                                          present in the circuit
        diameter                    : diameter of the coil
        length                      : length of the coil
        lead                        : the length of the lead
                                          wire
        coil_loss                   : the loss by the coil
                                          without core
    """
    self._prepare_data(file, vacuum=vacuum)
    self.mdf["normalized_temperature"] = round(self.mdf["
                                        temperature"]*2)/2
    self.parasitic = parasitic
    self.lead = lead if lead is not None else 0.16
    # creating the time axis
    if "dt" not in self.mdf.keys():
        self.mdf["dt"] = 2e-8
    self.mdf["time"] = self.mdf.apply(lambda x: np.arange(0, x["
                                        dt"]*len(x["voltage_input"
                                        ]), x["dt"] ), axis = 1)
```

```
self.mdf[["fitted_input_voltage_amplitude", "input_phase", "
                                    input_offset"]] = self.mdf
                                    .apply(lambda x: curve_fit
                                    (f=sine_func, xdata=2*np.
                                    pi*x["frequency"]*x["time"
                                    ], ydata=x["voltage_input"
                                    ], p0=[10, 10, 10])[0],
                                    axis=1, result_type="
                                    expand")
self.mdf[["fitted_output_voltage_amplitude", "output_phase",
                                     "output_offset"]] = self.
                                    mdf.apply(lambda x:
                                    curve_fit(f=sine_func,
                                    xdata=2*np.pi*x["frequency
                                    "]*x["time"], ydata=x["
                                    voltage_output"], p0=[0,
                                    10, 10])[0], axis=1,
                                    result_type="expand")
# the phase differenece between input and output voltages
self.mdf["phase_shift"] = self.mdf["output_phase"] - self.
                                    mdf["input_phase"]
if diameter is not None and length is not None:
    self.mdf["coil_length"] = length
    self.mdf["coil_diameter"] = diameter
else:
    # getting the coil information from the database
    length, diameter = self.get_coil_info(self.mdf["turns"].
                                        values[0])
    self.mdf[["coil_length", "coil_diameter"]] = [length,
                                        diameter]
self.get_vacuum_inductance()
```

```
self.get_permeability_from_circuit_inductance(turns=self.mdf
                                              ["turns"].values[0])
# fitting a sine function to the data to get the amplitude
                                              and phase of the input and
                                               output channels
self.mdf["parasitic_voltage"] = self.get_parasitic_voltage()
if equivalent_vacuum_file:
    self.vacuum_circuit = Circuit(file=
                                      equivalent_vacuum_file
                                      , turns=turns, vacuum=
                                      True)
    self.vacuum_circuit.get_circuit_inductance()
    self.vacuum_circuit.mdf["normalized_temperature"] =
                                      round(self.
                                      vacuum_circuit.mdf["
                                      temperature"]*2)/2

    vacuum_df = self.vacuum_circuit.mdf.groupby("
                                      normalized_temperature
                                      ").mean()[["
                                      circuit_resistance", "
                                      circuit_inductance"]].
                                      reset_index()
    rw_vs_temp_linear, cov = curve_fit(linear, xdata=
                                      vacuum_df["
                                      normalized_temperature
                                      "], ydata=vacuum_df["
                                      circuit_resistance"],
                                      p0=[1, 1])
    vacuum_df["vacuum_circuit_resistance"] = vacuum_df["
                                      circuit_resistance"]
    self.mdf["vacuum_circuit_resistance"] = linear(self.mdf[
```

```
                                                        "
                                                        normalized_temperature
                                                        "], *rw_vs_temp_linear
                                                        )
        else:
            self.vacuum_circuit=None
            self.mdf["vacuum_circuit_resistance"] = 99e-3

        # find the resistance due to the wire and calculate the
                                                    voltage diff due to it.
        self.mdf["wire_resistance_voltage"] = self.mdf.apply(lambda
                                                    row: row["
                                                    vacuum_circuit_resistance"
                                                    ]*row["current"], axis=1)

        self.coil_loss = coil_loss

    def get_vacuum_inductance(self):
        """
        Calculating the vacuum inductance with corrections
        """
        wire_diameter = self.coil.winding.diameter
        rho = 1.724e-8
        mu0 = 4*np.pi*1e-7
        self.mdf["effective_diameter"] = self.mdf.apply(lambda x:
                                                    effective_diameter(x["
                                                    coil_diameter"]-0.00027,
                                                    wire_diameter, x["
                                                    frequency"], rho, mu0, x["
                                                    turns"], x["coil_length"]-
                                                    wire_diameter), axis=1)
        self.mdf["km"] = self.mdf.apply(lambda x:
```

```
                                            mutual_inductance_correction
                                            (x["turns"], x["
                                            effective_diameter"], x["
                                            coil_length"]-
                                            wire_diameter), axis=1 )
        self.mdf["ks"] = self.mdf.apply(lambda x:
                                            self_inductance_correction
                                            (x["effective_diameter"],
                                            wire_diameter, x["
                                            coil_length"]-
                                            wire_diameter, x["turns"])
                                            , axis=1)
        self.mdf["kl"] = self.mdf.apply(lambda x: non_linearity(x["
                                            effective_diameter"], x["
                                            coil_length"]), axis=1)
        self.mdf["Li"] = self.mdf.apply(lambda x:
                                            inner_inductance_low_freq(
                                            rho, x["frequency"], mu0,
                                            x["turns"], x["coil_length
                                            "]-wire_diameter,
                                            wire_diameter, x["
                                            effective_diameter"]),
                                            axis=1)
        self.mdf["vacuum_inductance"] = mu0*np.pi*(self.mdf["
                                            effective_diameter"]*self.
                                            mdf["turns"]/2)**2*self.
                                            mdf["kl"]/self.mdf["
                                            coil_length"]
        return self.mdf["vacuum_inductance"]


    def get_coil_info(self, turns: int):
```

```
        """
        Get the coil information

        Args:
            turns (int): Number of coil turns
        """

        self.coil = Coil(turns)
        return self.coil.length, self.coil.diameter

    def get_flux(self):
        """
        Calculating the flux from the voltages
        B= 1/A x \int (dV_o - dV_p)dt
        """
        self.mdf["flux"] = self.mdf.apply(lambda x: flux(x["
                                                   voltage_output"]-x["
                                                   parasitic_voltage"]-x["
                                                   wire_resistance_voltage"],
                                                    x['dt'], x["
                                                   effective_diameter"], x["
                                                   turns"], 2*np.pi*x["
                                                   frequency"]*x["time"], ((x
                                                   ["flux"])[1]+x["flux"][0])
                                                   /2)*x["dt"]/(2*np.pi*x["
                                                   frequency"]), axis = 1)
        return self.mdf[["temperature", "time", "flux"]]

    def get_current(self):
        """
        Calculating the current from the voltages
        I = (dV_i - dV_o)/R
```

```
        """
        self.mdf["v_r"] = self.mdf["voltage_input"] - self.mdf["
                                            voltage_output"]
        # use the above formula to calculate the current
        self.mdf["current"] = self.mdf.apply(lambda x: (x["v_r"])/x[
                                            "resistance"], axis = 1)
        return self.mdf["current"]

    def get_field(self):
        """
        Calculating the field from the current
        H = N/l I
        """
        if "current" not in self.mdf.keys():
            self.get_current()
        # calculating the field according to the formula
        self.mdf["field"] = self.mdf.apply(lambda x: field(x["
                                            current"], x["turns"], x["
                                            coil_length"]), axis = 1)
        return self.mdf[["temperature", "time", "field"]]

    def get_circuit_inductance(self):
        """
        Calculating the inductance from the circuit equations.
        """

        # calculating the real and imaginary parts of the impedance
        self.mdf["v_real"] = self.mdf.apply(lambda x: (x["
                                            fitted_output_voltage_amplitude
                                            "])/x["
                                            fitted_input_voltage_amplitude
                                            "]*np.cos(x["phase_shift"]
```

```
                                        ), axis=1)
    self.mdf["v_im"] = self.mdf.apply(lambda x: (x["
                                        fitted_output_voltage_amplitude
                                        "])/x["
                                        fitted_input_voltage_amplitude
                                        "]*np.sin(x["phase_shift"]
                                        ), axis=1)
    # numerically solve the circuit equations
    rs = [fsolve(simple_circuit, [10, 0.000008], args=(row["
                                        v_real"], row["v_im"], row
                                        ["resistance"], 2*np.pi*
                                        row["frequency"])) for i,
                                        row in self.mdf.iterrows()
                                        ]
    self.mdf[["circuit_resistance", "circuit_inductance"]] = rs
    return self.mdf["circuit_inductance"]

def get_permeability_from_circuit_inductance(self, turns: int):
    """
    Calculating the permeability from circuit_inductance


    Args:
        turns (int): Number of coil turns
    """
    if "cicuit_inductance" not in self.mdf.keys():
        self.get_circuit_inductance()
    if not turns:
        turns = self.mdf["turns"].values
    L0 = self.mdf["vacuum_inductance"]
    self.mdf["circuit_permeability"] = (self.mdf["
                                        circuit_inductance"]-self.
                                        parasitic)/L0
```

```
        return self.mdf["circuit_permeability"]

    def get_amplitude_permeability(self):
        """
        Calculate the B_max/mu0*H0
        """
        if "flux" not in self.mdf.keys():
            self.get_flux()
        if "field" not in self.mdf.keys():
            self.get_field()
        mu0 = 4*np.pi*1e-7
        self.mdf["amplitude_permeability"] = self.mdf.apply(lambda
                                                 row: max(row["flux"])/(mu0
                                                 *max(row["field"])), axis=
                                                 1)


    def get_parasitic_voltage(self):
        """
        Calculate the voltage resulting from the parasitic
                                                 inductance.
        V_p = L dI/dt
        """
        if "current" not in self.mdf.keys():
            self.get_current()

        self.mdf[["current_amplitude", "current_phase", "
                                                 current_offset"]] = self.
                                                 mdf.apply(lambda row:
                                                 curve_fit(sine_func, xdata
                                                 =2*np.pi*row["frequency"]*
                                                 row["time"], ydata=row["
```

```
                                            current"], p0=[1, 10, 1])[
                                            0], axis=1, result_type="
                                            expand")
        self.mdf["current_derivative"] = self.mdf.apply(lambda row:
                                            row["current_amplitude"]*2
                                            *np.pi*row["frequency"]*np
                                            .cos(2*np.pi*row["
                                            frequency"]*row["time"]+
                                            row["current_phase"]),
                                            axis=1)

        parasitic_voltage = self.parasitic*self.mdf["
                                            current_derivative"]

        return parasitic_voltage.values

    def get_hysteresis_area(self):
        """
        Calculating the hysteresis area
        """

        self.mdf["hysteresis_area"] = self.mdf.apply(lambda x:
                                            Polygon(zip(x["flux"], x["
                                            field"])).area/(x["
                                            frequency"]*x["time"][-1])
                                            -self.coil_loss, axis = 1)
        return self.mdf["hysteresis_area"]

    def get_imaginary_permeability(self, turns: int):
        """
        Calculating the imaginary component of the permeability
```

```
        Args:
            turns (int): Number of coil turns
        """
        self.get_hysteresis_area()
        mu0 = 4*np.pi*1e-7
        self.mdf["hysteresis_resistance"] = self.mdf.apply(lambda x:
                                                  x["hysteresis_area"]*2*(
                                                 np.pi*(x["
                                                 effective_diameter"])**2/4
                                                 )*x["coil_length"]*x["
                                                 frequency"]/x["current"].
                                                 max()**2, axis = 1)
        self.mdf["mu_imag"] = self.mdf.apply(lambda x: (x["
                                                 hysteresis_resistance"])*x
                                                 ["coil_length"]*4/(mu0*2*
                                                 np.pi*x["frequency"]*turns
                                                 **2*np.pi*x["
                                                 effective_diameter"]**2),
                                                 axis = 1)

    def _prepare_data(self, file, vacuum: bool = False):
        base = f'./buckets/{"vacuum_archive" if vacuum else "
                                                 ferrite_archive"}/raw/'
        input_file = os.path.join(base, "input", file)
        output_file = os.path.join(base, "output", file)
        input_df = pd.read_csv(input_file)
        input_df["voltage"] = input_df["voltage"].apply(lambda x: np
                                                 .array(eval(x)))
        output_df = pd.read_csv(output_file)
        output_df["voltage"] = output_df["voltage"].apply(lambda x:
                                                 np.array(eval(x)))
        self.mdf = pd.merge(input_df, output_df[["voltage"]],
```

```
                                                                    left_index=True,
                                                                    right_index=True, suffixes
                                                                    =["_input", "_output"])
        self.mdf["frequency"] = int(file.split("_")[2])
```